Laser excitation of positronium produced by various materials at a range of temperatures.

Ben Cooper - October 2017

A thesis submitted to the Department of Physics and Astronomy, University College London for the degree of Doctor of Philosophy.

Abstract

Methods and techniques in the production, manipulation, and accumulation of positrons in a 'Surko-type' buffer-gas trap are presented. The pulsed output of the trap is optimised for laser excitation of positronium (Ps). The techniques of positron time compression and single-shot positron annihilation lifetime spectroscopy (SSPALS) are discussed in detail and used throughout the study.

A small array or Ps converter materials have been characterised at various temperatures. Ps cooling as a function of positron implantation is presented and discussed. Direct laser irradiation of the samples, and the effect on the Ps yield has also been studied. In some cases, particularly at cryogenic temperatures, laser induced paramagnetic centres are formed and this has a detrimental effect on the Ps yield as they cause triplet Ps to convert to the shorter-lived singlet state. Whereas in single crystal semiconductors, the laser has an enhancing effect due to an exciton-like positron-electron surface state. Many of the Ps converter materials studied here are formed from porous structures. The long term confinement of Ps within isolated cavities has also been observed, where a lifetime measurement technique using an excitation laser is presented.

General methods of Ps-laser spectroscopy are also presented and the applications of which are discussed including laser-enhanced time-of-flight spectroscopy (LEPTOF), and the production, and electrostatic guiding of highly excited Rydberg Ps. Using these techniques a crossed beam scattering experiment involving Rydberg Ps, electrons, and Argon ions was carried out.

This work presents important considerations for experiments to create a laser-cooled Bose-Einstein condensate (BEC) of Ps in an engineered porous material at cryogenic temperatures.

Declaration

This work has not previously been accepted in substance for any degree and is not being concurrently submitted in candidature for any degree.

Signed ..... (candidate)

Date .....

Statement 1

This thesis is the result of my own investigations, except where otherwise stated. Where correction services have been used, the extent and nature of the correction is clearly marked in a footnote(s).

Other sources are acknowledged by footnotes giving explicit references. A bibliography is appended.

Signed ..... (candidate)

Date .....

Statement 2

I hereby give consent for my thesis, if accepted, to be available for photocopying and for inter-library loan, and for the title and summary to be made available to outside organisations.

Signed ..... (candidate)

Date .....

Contents

Acknowledgements

I wish to thank my supervisor, Dr David Cassidy, for his unwavering determination for the project to succeed, for his wealth of experience and insight, and for affording me the freedom and self direction I've enjoyed throughout my time at UCL. I also thank Professor Peter Barker, Dr Stephen Hogan, and Professor Gaetana Laricchia for their invaluable comments and suggestions. I also wish to thank Dr Adam Deller and Dr Thomas Wall, who expertly introduced me to the field and made my experience working in it so valuable, varied, and enjoyable.

It would have been exceptionally difficult to have made any progress without the assistance of our technical and administrative staff. I therefore wish to thank: John Dumper, Rafid Jawad, James Percival, Tony Hoare, Nadia Waller, James Gane, Khadija Bouzgan, and Derek Thomas.

I am also fortunate to have met so many fascinating people during my degree, through collaboration, at conferences, and just in and around the college. I acknowledge the many friends I have made along the way: Vincenzo Monachello, Søren Lindholt Andersen, Lia Han, Lokesh Gurung, Rina Kadokura, Alberto Alonso and many others.

The completion of this thesis was made possible by the support of my family and friends. I'm especially grateful to Guleraana, who has encouraged me to fulfill my potential every step of the way.

List of Figures

Chapter 1

Introduction

1.1 Antimatter

In 1928, Paul Dirac derived a relativistic wave equation, marrying the then recent developments of quantum mechanics and Einstein's special theory of relativity [Dirac, 1928a,b]. The quadratic form of the energy, $E^2 = m^2c^4 + p^2c^2$, within Einstein's theory [Einstein, 1905, 1907] lead to an uncomfortable prediction by the Dirac equation. Seemingly non-physical, negative energy solutions could not be avoided. Dirac [1930] proposed his "hole theory" , which predicts the existence of a twin particle to the electron of opposite charge. The theory suggested that in the vacuum, there exists a "sea" of negative energy electron states which combine to give a total energy, momentum and spin of zero, the infinite charge is uniformly distributed across all of space, and thus leads to fields that are not experimentally measurable. When a hole is created in this negative energy continuum, a particle with opposite charge to the electron makes a transition into the positive energy continuum. Dirac initially thought that these particles were protons but this idea was soon dismissed due to the difference in mass [Oppenheimer, 1930]. The notion

of an exotic and unobserved form of matter then followed. A particle of the same mass as the electron that would mutually annihilate upon contact with one was postulated. Dirac [1931] had predicted the existence of antiparticles. This idea was not taken seriously in 1933:

> Dirac has tried to identify holes with anti-electrons...We do not believe that this explanation can be seriously considered.
>
> *Handbuch der Physik* , **24**, 246 (1933)

However, the previous year, experimentalist Carl Anderson had imaged the paths of positively charged particles as they passed through a lead plate whilst he studied cosmic rays. He concluded that these particles could not be protons as the curvatures within his cloud chamber suggested a mass much smaller than would be expected. An observation that had occurred previously but was dismissed and not followed up [Merhra and Rechenberg, 2000]. The curvatures suggested a mass comparable to that of the electron. The discovery was later confirmed by Blackett and Occhialini [1933]. Dirac's anti-electron had been discovered. These particles were named positrons, and the discovery earnt Anderson a share of the 1936 Nobel prize. Dirac's 'hole theory' was later replaced by 'local relativistic quantum field theory' or quantum electrodynamics (QED) [Feynman, 1949a,b; Tomonaga and Oppenheimer, 1948]. The study of antimatter allows the testing of fundamental theories like QED, and CPT symmetry. The asymmetry of matter and antimatter in the observable universe remains one of the most challenging questions in modern physics. Studying simple systems involving antiparticles is an essential endeavour in the quest for a complete model of nature.

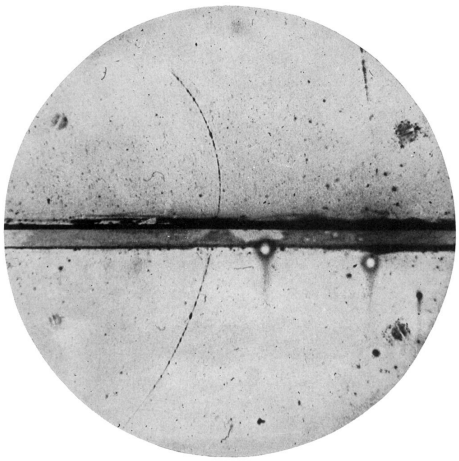

Figure 1.1: A 63 million volt positron, passing through a 6mm lead plate, and emerging as a 23 million volt positron. Carl Anderson concluded that the length of the latter path is at least ten times longer than what one would expect for a proton of the same curvature. [Anderson, 1933].

1.1.1 Positrons

The positron is the electron antiparticle. It possesses the same mass-energy, spin and charge magnitude as the familiar electron. The sign of the charge is however opposite. The production mechanisms for positrons are β^+ radioactive decay and pair production from high energy photons. Both electrons and positrons are stable in vacuum but, due to the opposite values of their additive quantum numbers, the two particles can decay into photons when they interact. The entire system's mass-energy is converted into energetic gamma rays in an annihilation event, in accordance with $E = mc^2$. In general, the lifetime against annihilation of a positron in an environment containing matter is inversely proportional to the local electron density. In condensed matter such as metals this is typically 250 ps [Cotterill *et al.*, 1972], whilst in gasses this may be considered as the minimum lifetime against annihilation.

1.2 Positronium

A positron can also exist in a neutral bound state with an electron. This is a positronium atom (Ps) and the first observations of Ps formation were performed by Deutsch [1951] at MIT. He later went on to measure the Ps Zeeman and hyperfine splitting [Deutsch and Brown, 1952]. Ferrell [1951] contributed to the theory of the fine structure between the 1^3S_1 and 1^1S_0 ground states of Ps.

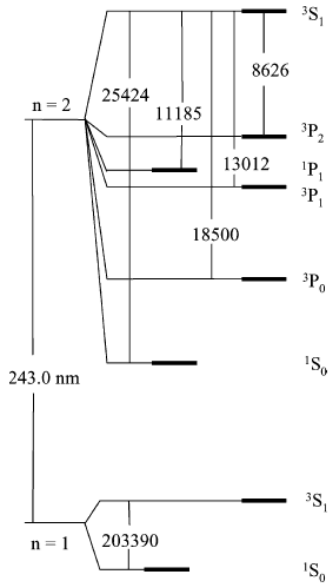

Figure 1.2: Schematic diagram of the lowest energy levels of Ps. The numbers separating the sub levels are given in MHz. The Lyman-α wavelength indicating the distance between $n = 1$ and 2 is also shown. Drawn from Ley [2002].

Positronium is more elementary in structure than the well understood hydrogen atom, and one can solve for the energy eigenvalues of Ps by using the non-relativistic Schrödinger equation, in the same way as hydrogen. The energy level structure for the ground and first excited states is shown in figure 1.2, where the levels are grouped into a singlet spin state, $S = 0$ and and triplet, $S = 1$ as the system is comprised of two fermions.

Each state is designated by $n^{2S+1}L_J$, where L and J are the orbital, and total angular momentum.

Due to the reduced mass of the system,

$$\mu = \frac{m_+ m_-}{m_+ + m_-} = (m_-/2) \tag{1.1}$$

if $m_+ = m_-$, where m_+ and m_- are the positron and electron mass respectively, the gross values of the energy levels are half of that of hydrogen [Ley, 2002]. For example the binding energy E_{Ps} = - 6.8 eV. The fine and hyperfine levels are more complicated than in hydrogen. This is due to the large magnetic moment of the positron in comparison with the proton, QED, and annihilation effects [Rich, 1981].

The requirement of the invariance of charge conjugation during an annihilation event, led Yang [1950] and Wolfenstein and Ravenhall [1952] to the following selection rule. It states that a positronium atom with total spin S, and orbital angular momentum L can annihilate, releasing n_γ photons. The selection rule is given by,

$$(-1)^{n_\gamma} = (-1)^{L+S}. \tag{1.2}$$

This rule states that singlet Ps in the ground state ($S = L = 0$) can only annihilate with an even number of gamma photons, whilst the triplet state ($S = 1$, $L = 0$) can only annihilate with an odd number of photons. For the singlet state, known as para-positronium (p-Ps), the dominant annihilation decay mode is through the release of 2γ-ray photons. Whereas the triplet state, ortho-positronium (o-Ps), predominantly decays with 3γ-rays [Ore and Powell, 1949]. The triplet state can annihilate with a single photon. However the probability of this decay mode is suppressed by the requirement of a third body to absorb the excess momentum. All states of Ps have a finite lifetime. In the ground state the the annihilation rates for the singlet and triplet sub states are $\approx$ 8 GHz for (p-Ps) and $\approx$ 7 MHz for (o-Ps) [Ore and Powell, 1949]. The inverse of these annihilation rates are the mean

lifetimes against annihilation, these are 0.125 ns [Al-Ramadhan and Gidley, 1994] and 142 ns [Vallery *et al.*, 2003] respectively. For n $>$ 1 the decay rates also have a contribution from spontaneous emission. Both the annihilation and spontaneous emission rates depend strongly on the principle quantum number n.

1.2.1 Rydberg positronium

The lifetime against annihilation for low angular momentum (L) Ps states increases with n^3, this is because the annihilation rate depends on the probability density, and hence the excited state wave function squared, evaluated at the origin of a spherical polar coordinate system. The annihilation rate therefore scales with n^{-3} [Berko *et al.*, 1980]. The spontaneous emission rate also scales with n^{-3} in the absence of an external field. This leads to an n^3 dependence on the fluorescence lifetimes (τ_{fluor}). For Ps in the $2p$ state in the absence of an external field, $\tau_{fluor} = 3.19 \times 10^{-9}$s [Hogan, 2013]. Ps is unlikely to annihilate in the $2p$ state as τ_{fluor} dominates the decay rate [Gallagher, 1994]. Extended lifetimes against annihilation are essential for many experiments involving Ps, and the lifetimes can be extended with excitation to Rydberg states. An atom is in a Rydberg state if the principle quantum number n is high, and the atom displays exaggerated properties [Gallagher, 1994]. Electric dipole transitions of Ps to longer lived Rydberg states can be initiated optically (see chapter 4).

The lifetime of Rydberg states are in general, strongly effected by external fields. Ps is unusual in that the linear Zeeman effect is suppressed due to cancellation effects of the positron and electron magnetic moments. For Ps prepared in large magnetic fields ($\geqslant$ 1 T), the induced electric field from the motional Stark effect becomes significant. However, for the experiments explained in later chapters, the applied magnetic fields are too small to observe these effects. For atoms prepared in $2p$ states, the combination of magnetic, and electric fields can cause mixing of singlet and triplet states [Curry, 1973]. This can result in a reduced lifetime against annihilation which can be controlled with the applied fields, and the polarisation of the excitation laser pulses [Alonso *et al.*, 2015]. Rydberg Ps does however interact

strongly with applied electric fields and this is due to the linear Stark shift and the large dipole moments which scale with n^2. The Ps electric dipole moment for a given n is approximately twice that of the corresponding Hydrogen atom due to equation 1.1 and its effect on the Bohr radius. The maximum induced Ps electric dipole moment associated with a particular Rydberg state is given by,

$$\vec{\mu} \simeq \frac{3}{2} n^2 e a_{0Ps}, \tag{1.3}$$

where e is the electron charge, and $a_{Ps} = 2a_0$ is the Ps Bohr radius, equal to 1.058 $\times$ 10^{-10} m. The Stark energy shifts and the forces that can be applied to Rydberg Ps via electric field gradients are therefore significantly larger than observed in Hydrogen. Hogan [2013] presents a calculation of the Stark energy shifts observed in Ps Rydberg states, obtained via the application of perturbation theory to the zero field solutions of the Schrödinger equation expressed in parabolic coordinates. To the second order the Stark energy shift is given by,

$$E_{Stark} = \frac{3}{2} nkea_{0Ps}|\vec{F}| - \frac{1}{16} n^4 (17n^2 - 3k^2 - 9m^2 + 19) \frac{e^2 a_{0Ps}^2}{E_{hPs}} |\vec{F}|^2, \tag{1.4}$$

where $E_{hPs} = 2hcRy_{Ps}$ is the Hartree energy for Ps, and k is the difference between two parabolic quantum numbers [Gallagher, 1994] and represents the level of dipole alignment with the external field. Hogan [2013] gives E_{Stark} to the fourth order from D. Kleppner and Zimmerman [1983]. The curvature of each state shown in figure 1.3 toward lower energy with increasing electric field strength is a consequence of the quadratic term in equation 1.4.

The figure shows that at reasonably modest electric fields, individual Rydberg-Stark states can be separated. $|m| = 2$ Rydberg states were calculated as the angular component of the spectral intensity of a $2p$ - nd transition depends on the azimuthal quantum number m of the $2p$ state, and the value Δm, and it is transitions where $m = 1$ $(2p)$ and $m = 2$ (nd) that are strongest [Hogan, 2013].

The split states are each denoted with the index value k. As the atoms move

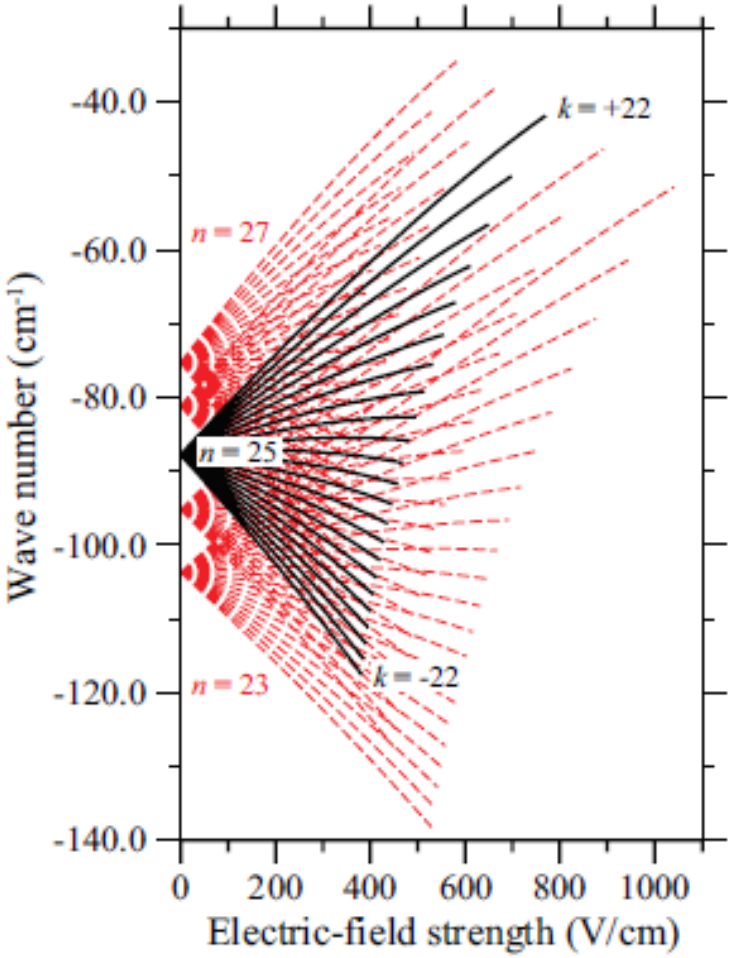

Figure 1.3: Stark map depicting the energies of the $|m| = 2$ Rydberg states of Ps with values of n between 23 and 27 in the presence of an external electric field [Hogan, 2013].

between regions of differing electric field strength, the internal energy is shifted according to the electric dipole moment and this will change the atom's kinetic energy as a result of the conservation of the total energy. Increasing the field strength will either speed the atom up, or slow it down depending on whether the Stark shift is positive, or negative. Rydberg-Stark states can therefore be grouped into low-field-seeking (lfs) states with positive shifts ($k > 0$), and high-field-seeking (hfs) states with negative shifts ($k < 0$). Rydberg Ps is however susceptible to ionisation by an electric field and the field required to ionise Rydberg Ps scales with n^{-4} in general but there is also a dependence on the index k (see chapter 4).

1.3 Motivations

We have built a pulsed beam of slow positrons for the purpose of positronium production and experimentation. The system is optimised for pulsed laser spectroscopy of Ps. We study positronium because it has applications, and offers insight into many areas of fundamental and applied physics and chemistry. In particular, Ps has some interestingly unique properties when compared to other atoms. For example, it is its own antiparticle and it can be described well using QED [Karshenboim, 2004], offering a system to test the theory. It is purely leptonic system without the presence of hadrons and the strong nuclear interaction, which could enable a precision spectroscopic measurements associated with an accurate determination of the Rydberg constant. This may have implications which shed some light on the proton size discrepancy [Antognini *et al.*, 2013]. Gravitational measurements on highly excited, long lived Rydberg-Stark states of positronium could lead to insights into the behaviour of antimatter in the gravitational field of the earth [Mills and Leventhal, 2002]. It is envisioned that a gravitational measurement would exploit the large electric dipole moments possessed by Rydberg Ps allowing the use of atom optics techniques previously demonstrated for other atoms and molecules, including mirrors [Vliegen and Merkt, 2006] and lenses [Vliegen *et al.*, 2006]. Long lived Rydberg-Stark states of Ps can also be transported with

field gradients for the purpose of antihydrogen production via charge exchange interactions [Deutch *et al.*, 1993; Hessels *et al.*, 1998]. Production of an efficient source of many antihydrogen atoms is an exciting prospect as it may provide a method of answering the questions of matter-antimatter asymmetry in the observable universe. Directly measuring if there are any differences between matter and the antimatter partners may aid understanding of why our universe is made almost entirely of matter, despite the prediction of the current standard model that matter and antimatter should have been produced in equal quantities during the big bang.

Another exciting prospect that the study of Ps offers is an observation of a Bose-Einstein condensate (BEC) of Ps, a system which could also provide a gravity measurement which utilises atomic interferometry [Cassidy and Mills, 2007b; Kasevich and Chu, 1992]. A Ps BEC could also facilitate the study of stimulated annihilation radiation, and perhaps the production of a γ-ray laser [Avetissian *et al.*, 2014; Bertolotti and Sibilia, 1979]. Developments of such a laser could produce a short wavelength beam suitable for probing nuclei, or a very powerful device used in orbit to protect the earth from large asteroids. These experimental endeavors may be enabled through the mastery and development of the techniques explained throughout this thesis.

Chapter 2

Positron Beams

β^+ decay from a radioisotope such as ^{22}Na is the most convenient source of positrons for experimentation in a small laboratory. Some facilities do utilise linear accelerators to produce positrons via pair production [Cowan *et al.*, 1993; Michishio *et al.*, 2011; Nagashima, 2014] but such sources are large in size. For a smaller laboratory, a radioactive isotope is a convenient alternative. ^{22}Na is selected as it has a large branching ratio for (β^+) emission (90.2%), a half-life of 2.6 years and it is commercially available with activities as high as 2 GBq. The decay scheme of ^{22}Na also has a rather striking feature in the production of an excited state of ^{22}Ne that rapidly decays via the emission of a 1.274 MeV photon. This photon can be used as a start signal in a positron lifetime measurement. This chapter gives an overview of the positron beam and trap which we assembled at the beginning of this study.

2.1 Positron moderation

To study systems containing many Ps atoms one needs a steady supply of positrons in the form of a beam. Positrons emitted from a β^+ source have broad energy distributions. For ^{22}Na the β^+ energy spectrum is peaked at 178 keV and its endpoint energy is 545 keV. To reduce this large spread of energies, moderating materials are placed near the positron source. The efficiency of an energy moderating material ϵ, is defined as the number of slow positrons that emerge from the material per β^+ particle emitted from the source. Metals do emit positrons with a narrow spread of energy [Mills, 1989] but they often have low efficiency.

By depositing Neon gas onto the source and allowing it to solidify at low temperature Mills and Gullikson [1986] were able to effectively double the efficiency previously achieved with single crystal tungsten. They measured $\epsilon = 0.70 \pm 0.02\%$ using a cylindrical geometry. Further improvements of ϵ were found by R. Khatri *et al.* [1990] who investigated the benefits of altering the geometry of the gas deposition to a conical arrangement. They achieved an efficiency, $\epsilon = 1.4 \pm 0.2\%$. The increased efficiency in solid rare gasses is due to the positrons being emitted before they have lost all of their initial kinetic energy. Large diffusion lengths allow positrons to travel to the surface and escape into vacuum having undergone some cooling within the deposit. ϵ is higher as a result, but the energy spread of positrons emitted from solid Ne is larger than a metallic moderator.

2.1.1 The positron source

A ^{22}Na sample is mounted behind a conical aperture. The unit is thermally coupled to, but electrically isolated from, a closed cycle helium cryostat. The cone is held between 5 and 8 K during positron beam operation. At the time of purchase (March 2013) the activity of the source was ≈ 2 GBq. We therefore estimate that at the time of writing, the activity of the source is ≈ 0.6 GBq.

The source chamber is evacuated to a base pressure of $\approx 2 \times 10^{-9}$ mbar. Two water cooled coils separated by their radius surround the source chamber which is encased in a large tank filled with lead grains. Figure 2.1 shows the DC positron section of the beam-line.

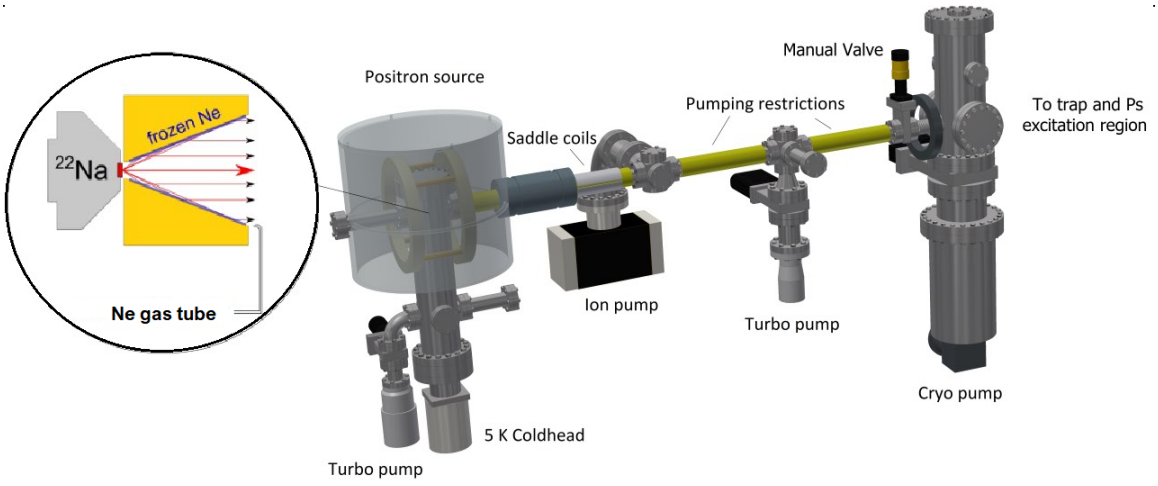

Figure 2.1: Schematic layout of the DC positron beam. Differential pumping is employed to protect the moderator from contaminants emanating from the positron trap. This is aided further by using two 8 mm diameter tubes located inside the second and third yellow solenoids which make up part of the magnetic guidance system. A pair of saddle coils is used to guide slow positrons over a velocity selection barrier. This beam is discussed in detail in Cooper *et al.* [2015]

It is important that a solid rare gas moderator is protected from contamination from gasses in the trap (See section 2.2) and elsewhere within the vacuum system. Limitation of contaminants diffusing to the source chamber is achieved with differential pumping along the DC section of the positron beam, and is aided further with conductance limiting inserts.

2.1.2 Moderator growth

When replacing an old, decayed moderator, the cold head expander is switched off, allowing the system's temperature to rise to around 20 K. Any remnants of an old moderator are thermally desorbed. With the cold head expander back on, the system is allowed to return to base pressure and temperature. The source is then heated to between 7-9 K (base temperature ~ 5 K), which is maintained by a resistive heater. The slight increase in temperature yields more positrons and this may be due to annealing of the Ne deposit as it is being formed. At a slightly elevated temperature, the surface layers are also less likely to absorb contaminants. Neon gas is then admitted to the cone via a small tube (figure 2.1).

We have found that there are great benefits to be had by growing the moderator at a fast rate with a higher Ne pressure. This is presumably due to less opportunity for contamination within the Ne deposit. This also improves the longevity of the moderator, increasing the period of use from several days to a number of weeks. However, moderator longevity is also heavily dependent on the vacuum quality that is achieved before, and after the growth sequence is initiated. A typical moderator growth curve following a fast growth ($\sim 8mins$) is shown in figure 2.2 (a), which yielded around 5.9 million positrons per second. The Ne pressure, as measured by a local ionisation gauge is $\sim 1 \times 10^{-3}$ mbar. Previously much slower growth cycles were used, typically with a Ne pressure $\sim 3 \times 10^{-4}$ mbar, for around 25-40 mins. This method would yield on average, a final count rate of around 4-5 million positrons per second, with a much faster decay. In recent months the best achievable beam strengths are around 3.5 million positrons per second and this is due to the age of the ^{22}Na source.

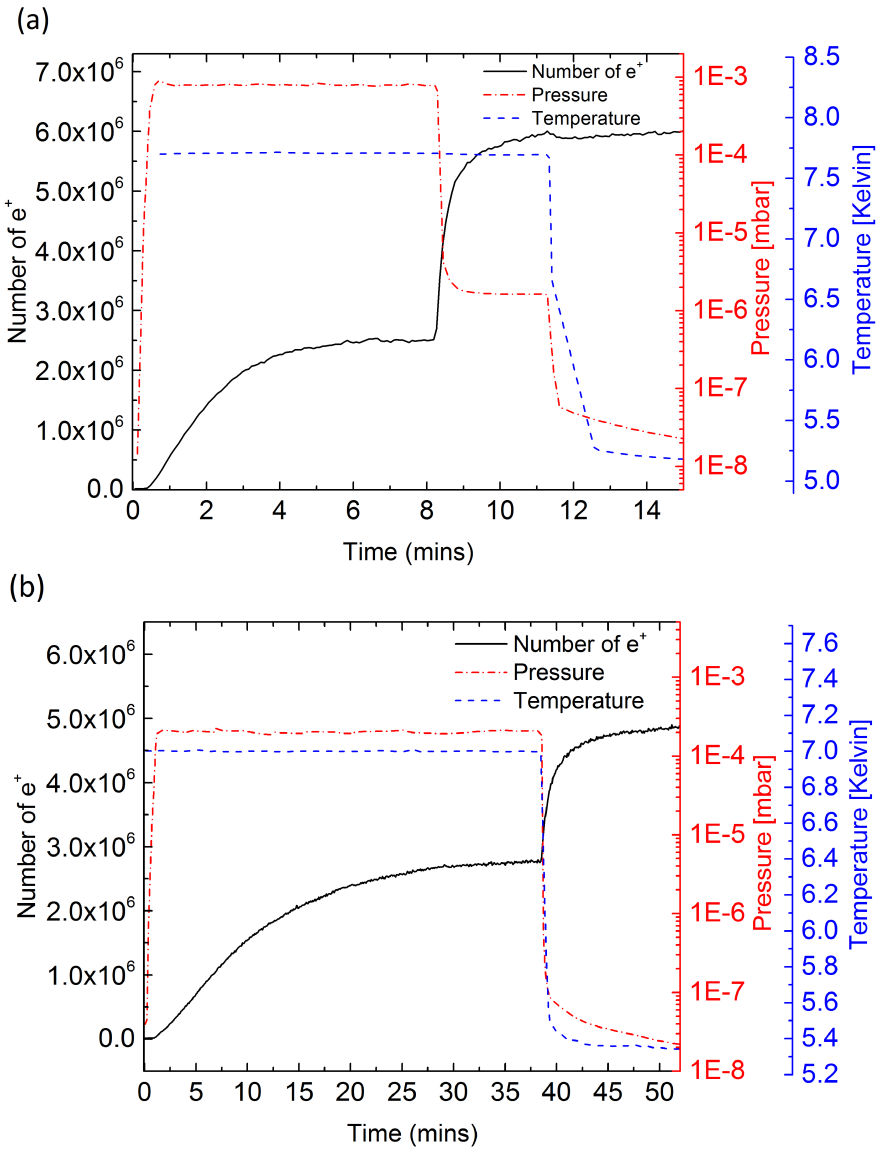

Figure 2.2: (a) Moderator 29 (5th Jan 2015). There is a steady increase in count rate (solid line) as the Neon gas pressure is increased (dotted line) over the growth period of around 9 minutes. As the count rate reaches a plateau, the Neon inlet is closed, causing a rapid increase in count rate, due to a reduction in gas attenuation of positrons. The temperature (dashed line) was set to 7.7 K during growth. The final count rate is ~ 5.9 million positrons per second. (b) Moderator 20 (12th Nov 2014). The lower temperature, pressure and growth time produces a weaker beam of ~ 4.9 million positrons per second.

2.1.3 Magnetic transport

An axial magnetic field is used to guide positrons along the beam line, from the source to the target chamber. Solenoid magnets are used as they provide the most uniform fields. However, they form only part of the beam as they prevent access to the vacuum system. In the gaps between solenoids we use a series of coils which are separated by a distance approximately equal to their radius. The positrons which form the slow beam and those which are trapped and ejected towards the Ps experimentation section are slow enough such that they follow the magnetic field lines. The field strength along the beam line is however non uniform. For a positron traveling between two points within the extent of the magnetic field, the position in the perpendicular (radial) direction can be found with the initial position (r_0, x_0) and the difference in field strength at the two points,

$$r = r_0 \sqrt{\frac{B_x}{B_{x_0}}}. \tag{2.1}$$

Qualitatively, this means that a positron beam is compressed in regions of high magnetic field, but in regions of lower field, the beam is larger. The magnetic field in the trap is $\approx$ five times larger than that of the Ps experimental region therefore leading to a beam size increase by a factor of around 2.2.

It is often the annihilation radiation which is to be detected at the opposite end of the beam line. In this case the detection apparatus must be properly shielded from the source so that one can separate the annihilation events caused by fast positrons with those from the slow positron beam or trap output. A pair of saddle shaped coils are used to guide the low energy beam over a solid barrier. The positron beam is also imaged using a micro channel plate (MCP) and phosphor screen assembly.

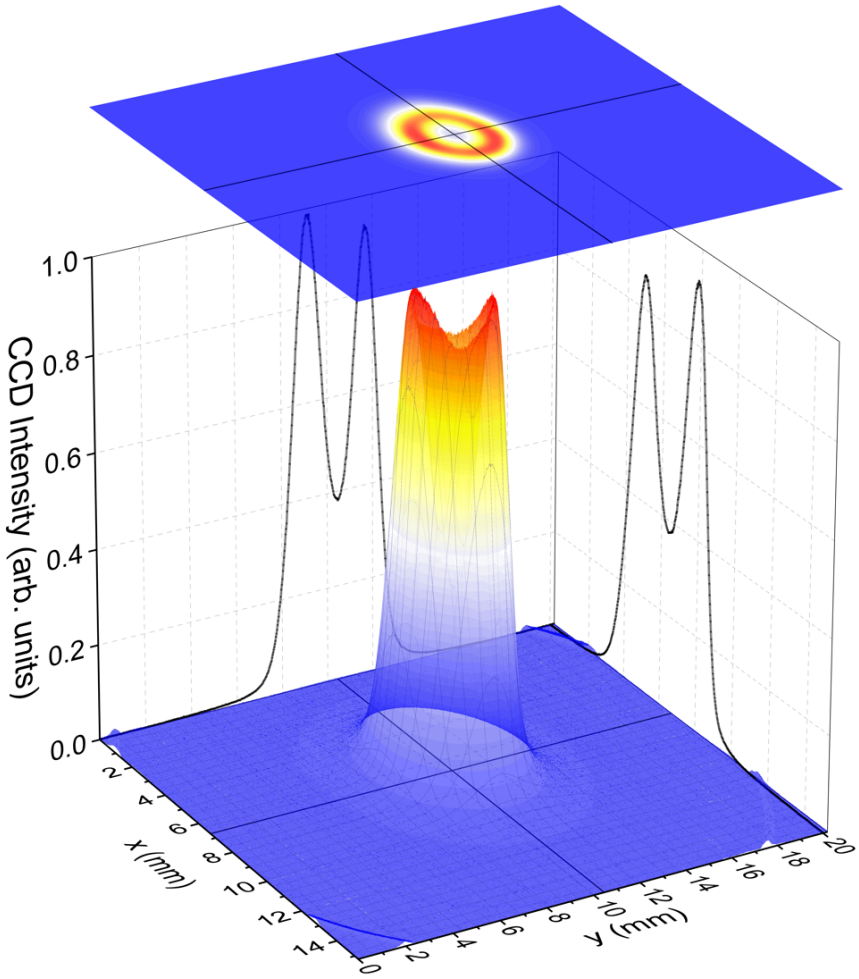

Figure 2.3: Slow positron beam imaged on MCP phosphor screen assembly with a 3D representation and 2D slices projected onto the axes. [Cooper *et al.*, 2015]

Figure 2.3 shows the ring shaped beam as imaged on the MCP phosphor screen. The hole in middle is due to the conical geometry shown in figure 2.1. The magnetic fields at the source and the MCP are approximately the same (≈ 13 mT). Figure 2.3 is thus a good representation of the beam size at the origin.

2.2 Positron trapping

The trapping and storage of positrons at low energies allows many scientific avenues to be realised. Studies involving the binding of matter with antimatter is of great interest, positronium being the prime example. Achieving a source of cold and trapped positrons is very useful in the production of antihydrogen [Gabrielse *et al.*, 2002; Madsen *et al.*, 2014], which in turn allows tests of fundamental symmetries such as the CPT theorem. Other applications of tailored positron sources include medicine, for example, positron emission tomography (PET) [Fischer *et al.*, 2001] and materials science [Gidley *et al.*, 2006]. The device of choice is often a variation of the Penning trap [Malmberg and deGrassie, 1975; Malmberg and Driscoll, 1980], which is a trap that confines particles in the radial direction by utilising a uniform magnetic field, whilst restriction in the axial direction is achieved by an electrostatic potential.

A Surko trap is a buffer gas (BG) trap which comprises of multiple stages of varying pressures of a neutral gas. The selection of the type of gas must consider the cross sections for direct annihilation, inelastic scattering, and Ps formation. With N_2 the inelastic scattering cross section for electron excitation is fairly large, allowing the positrons to quickly lose energy through inelastic collisions. The cross section for Ps formation is also large and this is the main loss mechanism when using N_2 as a buffer gas [Marler and Surko, 2005a]. Positrons in the eV range will excite an electronic transition within the gas molecule it is colliding with. Between 0.05 to several eV, vibrational transitions dominate and below 0.05 eV it is rotational excitations which achieve further cooling [Surko, 2010]. The cross sections for vibrational and rotational excitations with N_2 are small. To achieve

further cooling via these transitions, a small amount of CF_4 [Natisin *et al.*, 2014] is added to interact with positrons in the final stage of the trap.

The gas pressure in the first stage of the trap is tuned such that a positron will collide on average one time per transit. This enables a suitable loss of energy, leading confinement within the later stages which form a potential well. Positrons are prevented from reflecting backwards, leaving the trap, and eventually being lost to annihilation somewhere near the source. Further energy loss is achieved through additional electronic excitations in later stages of the trap, which are at lower pressures. The lower energy, vibrational and rotational cooling is achieved in the final stage via interactions with the secondary gas. The final stage can be located in a separate, differentially pumped section of the vacuum system for increased positron lifetimes [Cassidy *et al.*, 2006a]. The main benefit of this approach is the reduction of the pressure in the location of positron storage, as it is separated from the BG, lengthening the lifetime against annihilation. A long storage lifetime allows one to accumulate many more positrons. Cassidy *et al.* [2006a] successfully generated intense pulses containing $\sim 6 \times 10^7$ positrons, following ejection from an accumulator. This accumulator was loaded by opening the trap at a frequency of 4 Hz. With additional time compression a 1 ns pulse width was achieved. The high density pulse corresponded to an instantaneous positronic current of 10 mA. However, for the experiments explained here higher density pulses achieved with an accumulator are not required.

The trapping and cooling of positrons enables us to manipulate them into short, intense pulses. This in turn allows us to produce large numbers of Ps atoms in pulses, and perform Ps spectroscopy experiments. By storing positrons from a weak DC beam (with a large energy spread) one may produce either a high quality, pulsed positron beam ($\Delta E \sim 25$ meV), for use in scattering experiments for example [Marler and Surko, 2005b], or an intense pulsed beam [Cassidy *et al.*, 2006a; Greaves and Moxom, 2003], for use in experiments involving many positrons. Several facilities that employ this type of positron production and trapping method are now in operation, where many different experimental areas have been, and continue to be

explored [Andresen *et al.*, 2010; Cassidy *et al.*, 2006a; Clarke *et al.*, 2006; Sullivan *et al.*, 2010].

The device which this thesis is based upon is explained further in Cooper *et al.* [2015]. The positron trap is that of a Surko type with two stages. The electrostatic potential in each region varies, forming a potential well structure during the loading phase of the trap. A cutaway schematic of the trap is shown in figure 2.4 (a).

A comparison of the cross sections for the positron interaction processes is shown in figure 2.4(b). It is through inelastic collisions with the N_2 BG that enable positrons to slow down to the potential well energy shown in 2.4(c).

Compression of the ensemble of positrons in the radial direction is achieved with a "rotating wall" (RW) electrode, operating in a broad frequency range [Greaves and Moxom, 2008]. A similar type of compression method is used in experiments involving plasmas [Danielson and Surko, 2005; Greaves and Surko, 2000; Huang *et al.*, 1997]. The technique involves the application of a series of sinusoidal voltages to a segmented cylindrical electrode with an appropriate phase shift applied to each segment. The voltage applied is of the form

$$V_{RW}(t) = V_{RW} sin(\omega_{RW} t + \phi), \tag{2.2}$$

where V_{RW} and ω_{RW} are the amplitude and frequency of the sinusoidal function generated by an arbitrary waveform generator, and ϕ takes on increasing quantities of $\frac{\pi}{2}$ and is applied to adjoining segments. The electrode used in this study is segmented into four quarters. Figure 2.5 shows the affect of varying the applied frequency and amplitude of the sinusoidal function on the output of the trap.

In the reference frame of the positrons at the bottom of the potential well shown in figure 2.4 (c), the electric field will appear to rotate which in turn applies a torque. For the trap described here, the accumulated positrons are not dense enough to enter the plasma regime. The ensemble of positrons is non interacting which prevents the propagation of plasma modes. Compression is however still observed

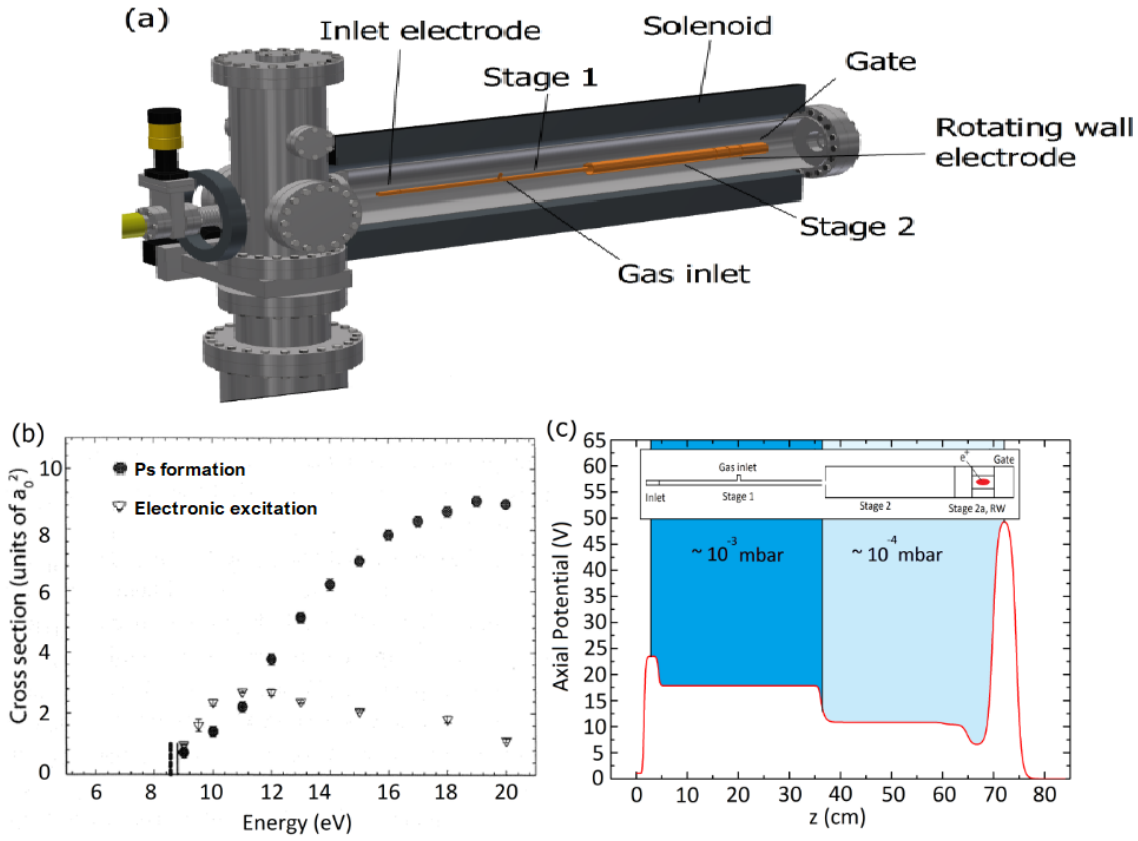

Figure 2.4: (a): Extension of figure 2.1 covering the two-stage Surko type positron trap. (b): Cross sections in atomic units for positron-impact, electronic excitation in N_2 and positronium formation. The dashed and vertical bars indicate the thresholds for electronic excitation and positronium formation, respectively. Drawn from Marler and Surko [2005a]. (c) Top: Scaled drawing of the trap electrode structure, including the segmented rotating wall electrode. Bottom: Axial potential during the trapping phase, calculated with SIMION. [Cooper *et al.*, 2015]

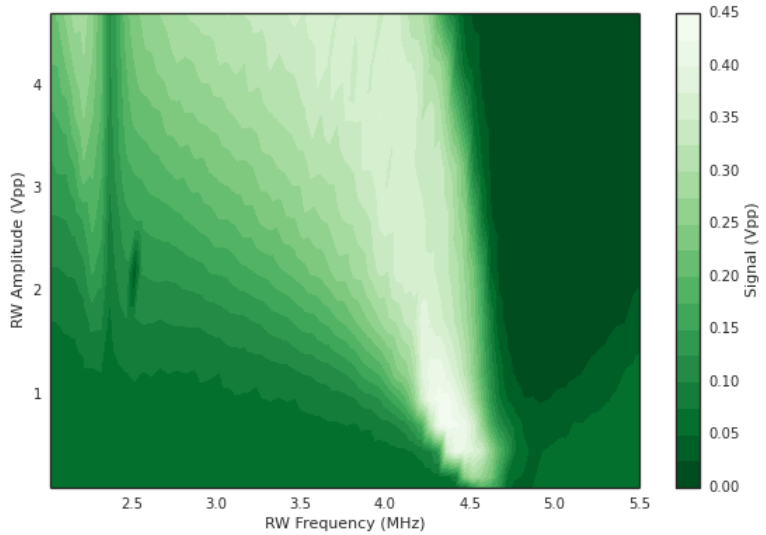

Figure 2.5: Variation of the amplitude and frequency of the applied rf signal and the effect on the trapping efficiency. The maximum output (white) corresponds to a trapping efficiency of ≈ 5 %

in what is known as the 'single particle regime' which works on the basis of the rf drive frequency being close to the axial bounce frequency of the trapped particles [Greaves and Moxom, 2008].

The process of compression causes heating of the positrons through resonant interactions with the particle motion. Cyclotron cooling is adequate provided that the magnetic field is strong enough to cause sufficient cooling within the positron lifetime in the trap. However, with a modest magnetic field of ≈ 50 mT the CF_4 molecular gas ($\approx \frac{P_{N_2}}{5}$) facilitates vibrational and rotational cooling [Natisin *et al.*, 2014].

In order to measure the lifetime of positrons in the trap, the length of the trap loading time was varied. Figure 2.6 shows trap accumulation data from the positron annihilation signal following the output of the trap. The ideal loading duration is when the amount of positrons lost per cycle is minimised with maximum output, i.e near the highest point of the linear region in the data shown in figure 2.6.

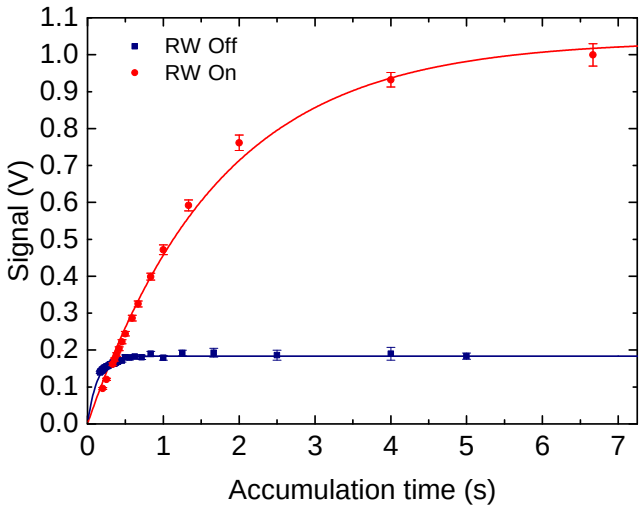

Figure 2.6: Accumulation curve yielding an estimation of the positron lifetime within the trap. τ was extracted by fitting equation 2.3, and has a value of 1.80 $\pm$0.08 s. The accumulation rate is found as 0.60 $\pm$ 0.03 Hz. The trap output is considerably lower without rotating wall compression. [Cooper *et al.*, 2015]

The trap output was recorded via annihilation radiation following positron collision with a solid barrier. The pk-pk voltage of this annihilation signal, which is directly proportional to the amount of positrons released, was recorded and plotted against the inverse of the trigger frequency.

The gate electrode was lowered to 0V from 52V at a variable rate controlled by a pulse delay generator. The data is fitted to

$$N_e(t) = C(1 - e^{-t/\tau}), \tag{2.3}$$

where τ is the positron lifetime in the second stage of the trap and C = Rτ, where R is the accumulation rate.

With the RW on, the measured lifetime is almost entirely due to interactions with the gas molecules in the trap. Without the RW there is an increased annihilation rate due to positron diffusion towards the trap electrodes [Deller *et al.*, 2014]. The operational range of the trap is 0.5 - 10 Hz. For most applications the trap is operated at 1 Hz as this offers a high number of positrons and is easily synchronised with our pulsed lasers that typically operate at 10 Hz (see chapter 4).

2.2.1 Trap output pulse

When running the trap at 1 Hz with an average moderator the trap releases around 10^5 e^+s^{-1}. Single positron annihilation events were used to calibrate a detector comprised of a scintillation material and PMT. This was done when the slow positron beam passed through the system with the trap switched off. The pk-pk voltage recorded for the single events which were on average received at a rate of ≈ 1 μs^{-1} was then scaled for the case of maximum trap output and solid angle leading to a measurement of the number of trapped positrons.

The output pulse can also be imaged at the MCP (figure 2.7). Spatially, the trap outputs a pulse of positrons which have a Gaussian distribution. With rotating wall compression active, the spatial width of the pulse is 2.57 ± 0.01 mm FWHM. The beam is approximately three times wider and three times less intense without the RW (see figure 2.6). The distance scale in the recorded image was calibrated by allowing the positron pulse through a 2 mm aperture in the target region. This was done as there is a different magnetic field strength at the target compared with the MCP, which is indicated in figure 2.7.

We aim to make many Ps atoms which can be excited by pulsed (ns) lasers. In order to overlap the Ps atoms with the laser pulses in time we must temporally compress the output of the trap. Liouville's theorem [Liouville, 1838] is the ultimate constraint on bunching in the presence of non-conservative forces. As the full volume occupied in phase space by the particle ensemble is conserved, one can distort the phase space in one dimension i.e velocity at the cost of distorting another in an opposing fashion. For example, if the velocity of a particle group can be compressed i.e 'time bunched' then the energy spread is increased.

Two bunching methods have been used during the course of the study. Firstly, we applied a pulse directly to the trap electrodes which caused the positrons to leave the trap in a time-bunched packet. This was achieved with a fast ramp voltage of ~180 V, applied to all of the trapping electrodes. This produces pulses of around 10^5 positrons, which are of a Gaussian distribution spatially, as shown in figure 2.7.

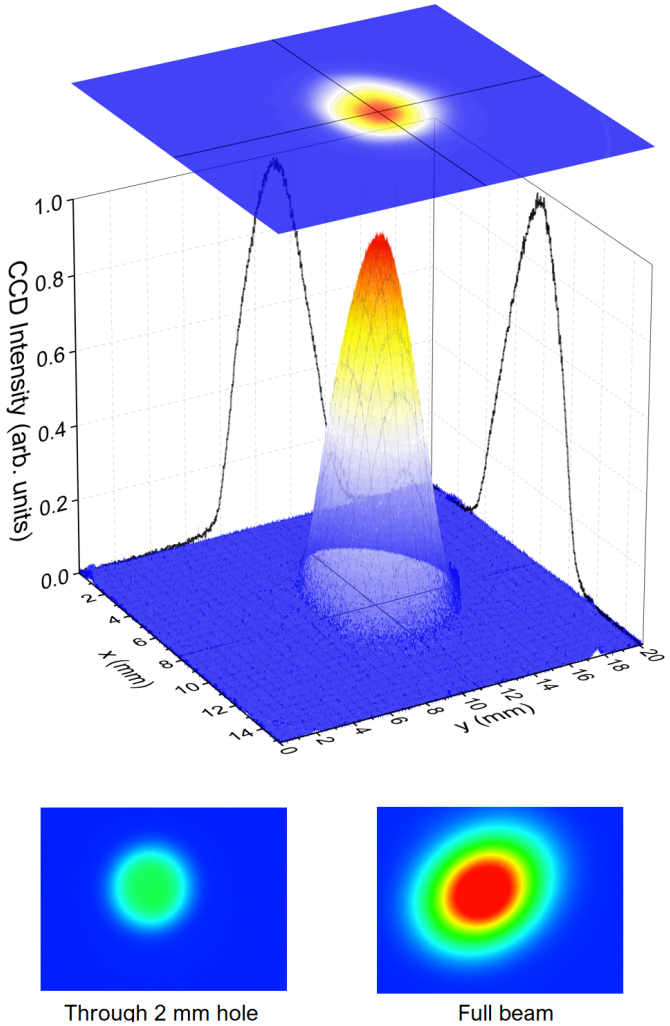

Figure 2.7: Top: Trap output pulse imaged, using the same detectors as in figure 2.3 the spatial width is 2.57 $\pm$ 0.01 mm FWHM [Cooper *et al.*, 2015]. Bottom left: Image of beam passing through 2 mm alignment hole. Bottom right: Full beam imaged after lifting the alignment hole out of the beam path.

This buncher is similar to other versions [Mills, 1980] except that each buncher section or ring has its own individually tuned avalanche pulser voltage which is applied on top of and independently of the DC bias voltage (figure 2.4 (c)) and the rf rotating wall voltages which are applied to the segmented electrode near the end of the trap. This bunching method is appropriate for a short flight path from the trap to the target, such as the setup shown in figure 2.8. This arrangement is explained in detail in Cooper *et al.* [2015], and has facilitated a range of experiments including Ps production, time-of-flight studies [Deller *et al.*, 2015b], and the production of Rydberg-Stark states of Ps [Wall *et al.*, 2015].

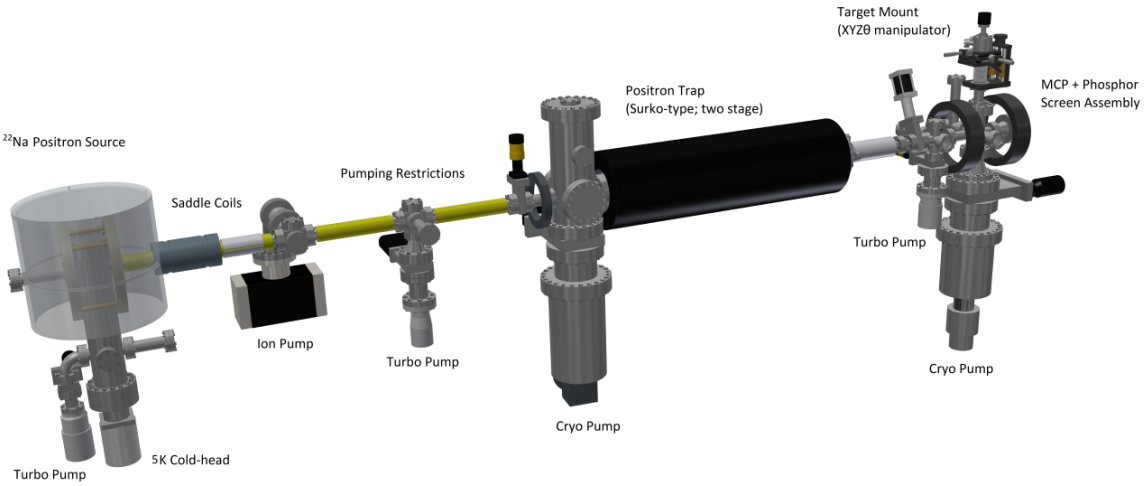

Figure 2.8: The DC positron beam and trap coupled to a Ps formation and excitation chamber. The distance from the trap to the target is ~ 0.5 m. The magnetic fields at the source, in the trap center and at the MCP detector are approximately 13, 50, and 13 mT respectively. [Cooper *et al.*, 2015].

For some experiments an extended beam line is required and the bunching method must be adapted. Pulsing directly from the trap is limited as the output starts to diverge in time as the trap-target distance increases. This limitation is overcome by using a simple 'pull-down-gate' switch which allows positrons out of the trap without bunching. Then, following magnetic transport along the beamline, time-bunching is performed closer to the target. A potential is applied along a series of rings which are aligned to the beam axis, this buncher is shown in figure

6.2. The applied potential varies quadratically with distance due to the resistance between each ring. The pulse is applied via a fast solid state switch. The positrons within the ring structure see an approximately harmonic potential. The switch pulse time is delayed relative to the trap opening to allow for transit from the trap to the buncher rings. A typical bunched positron pulse is shown in figure 2.9.

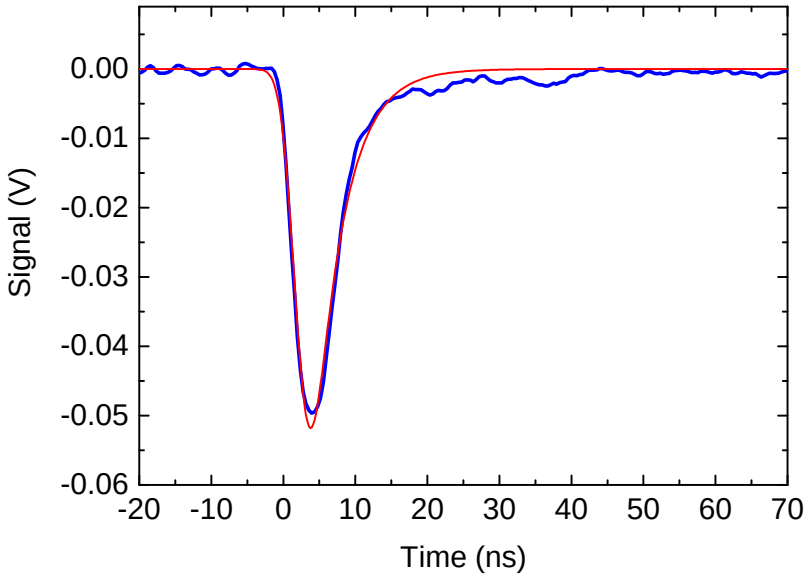

Figure 2.9: Annihilation signal of bunched positrons on a metal surface. The measurement was performed at the position of Ps production using a Cerenkov radiator and PMT. The fit to the data is convolution of the detector response with the Gaussian shape of the the positron beam and is explained further in Cooper *et al.* [2015].

Both bunching methods produce positron pulses of $\Delta t \sim 4$ ns as measured at the Ps converter target, which is suitable for temporal overlap with lasers of $\Delta t \sim 6$ ns. However, the measured time-width is dependent on the distance between the buncher and target, and the size and timing of the applied voltage pulse.

Chapter 3

Detection and measurement of Positronium

When a beam of slow positrons is incident on a target material, formation of the Ps atom is possible. The amount of Ps produced varies depending on the material but can be large for porous insulators. Detection of Ps can be achieved using annihilation γ-rays, and the timing associated with their detection. The detectors must be fast enough to differentiate between photons emanating from direct positron-electron annihilation, and photons that have a delay associated with the decay of *o*-Ps. *p*-Ps is too short lived (picoseconds) for detection using the methods explained here. The longer lifetime of *o*-Ps (nanoseconds) is detected using scintillation materials and photo multiplier tubes (PMT). Long lived Rydberg-Ps can also be detected via impact with a micro-channel plate (MCP).

3.1 Single shot positron annihilation lifetime spectroscopy

To study processes involving many positrons and positronium atoms, a packet of positrons ($\approx 10^5\ s^{-1}$) is ejected from the trap. The pulse ($\Delta t \sim 4ns$) is then implanted into a Ps converter material. Data is analysed with single-shot positron annihilation spectroscopy SSPALS [Cassidy *et al.*, 2006b], which is a method of detection and analysis of annihilation radiation. The basic methodology is as follows: The positrons are implanted into a material in a short pulse and this produces a continuous burst of annihilation γ-rays. A fast scintillating material undergoes luminescence when exposed to the ionising radiation. Scintillation light is converted into an electrical pulse with a PMT which is divided between two channels of a 1 GHz, 12 bit digital oscilloscope with a 50 Ω tee. The waveform from each channel are then spliced together and a constant fraction discriminator (CFD) algorithm is used to determine the trigger time (t = 0), configured for the leading-edge of the prompt peak. Division of the PMT output is done as it is necessary to observe the detector response over two separated channels, allowing us to avoid saturation of the signal in the early part of the spectrum whilst recording delayed events at a high gain. The timing characteristics of the SSPALS technique depend on the intrinsic response of the detector. SSPALS is ultilised here with two independent detectors which comprise of two types of scintillation materials: lead tungstate ($PbWO_4$) [Cassidy *et al.*, 2006b], and cerium doped lutetium yttrium oxyorthosilicate (LYSO) [Alonso *et al.*, 2016; Cooke *et al.*, 2000]. The SSPALS technique can also be used with alternative materials such as PbF_2 [Cassidy and Mills, 2007a]. An example spectrum is shown in figure 3.1.

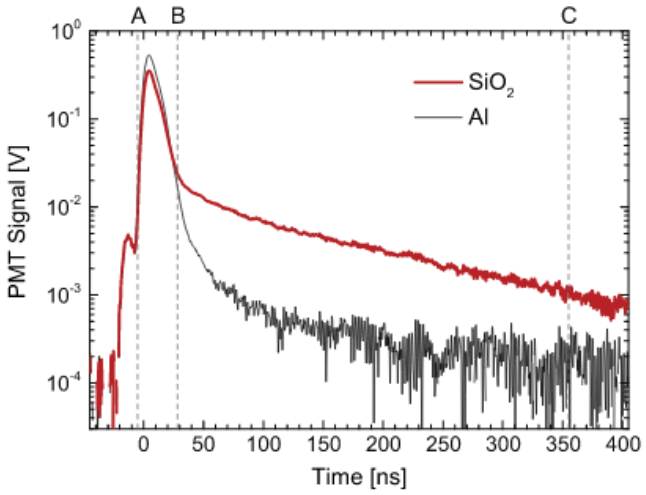

Figure 3.1: Lifetime spectra for 1 keV positrons implanted into an aluminium (black) or porous silica (red) target. The untreated Al surface is not expected to produce a significant amount of Ps, whereas the delayed signal evident from the silica target indicates a positron to *o*-Ps conversion efficiency of $\approx$ 25%. The step at around t = 10 ns is due to positrons annihilating on a pumping restriction aperture downstream from the target region [Deller *et al.*, 2015b].

One can extract from the data, the fraction of annihilation events that are delayed (f_d). This value is found as the ratio of the integrated areas *B*-*C* and *A*-*C*,

$$f_d = \int_B^C V(t)dt / \int_A^C V(t)dt, \tag{3.1}$$

where $V(t)$ is the PMT anode signal. These integration time windows (A, B, and C) are indicated in figure 3.1, and their selection depends on the process to be studied [Cooper *et al.*, 2015]. It is usually adequate to compare the counts in the prompt peak with those at later times. This is true for experiments involving photo-ionisation of Ps or any type of induced quenching of Ps in the ground state [Cooper *et al.*, 2016], or n = 2 [Alonso *et al.*, 2015]. For these processes the range *A*-*B* is fixed to contain only the prompt annihilation events and is typically -10 to 30 ns for $PbWO_4$, which is due to the decay time of the material.

The short lived Ps component will also contribute to the prompt peak. It will include *p*-Ps annihilation along with *o*-Ps that suffers spin exchange (see chapter 6) or other quenching processes, such as those due to the presence of magnetic, and or electric fields [Curry, 1973].

The data in figure 3.1 is displayed on the log scale for clarity and is the average of 60 single-shots. The two spectra highlight the difference between two materials in their suitability for producing *o*-Ps. Porous silica is often used as it produces large fractions of *o*-Ps which is cooled via collisions within the material (see chapter 5).

For experiments involving the prompt destruction of Ps in excited states as a means of detection, the later part of the spectrum will mostly contain the annihilation, or reduction thereof, of *o*-Ps. The region *B*-*C* is typically set as 30-600 ns for these experiments when using the $PbWO_4$ detector (50-1000 ns for LYSO). A comparison between measurements of the excitation of $n = 2$ Ps followed by prompt photoionisation is shown in figure 3.2(a) and (b). The excitation lasers (see chapter 4) cause an increased signal during the time of the prompt peak (*A*-*B*). This will therefore reduce the amount of delayed annihilation events at times outside the window. Here the *B* parameter is selected as the approximate cross over point between positive and negative signals in the background subtracted trace. The selection of *B* is the most critical as it allows direct access to information regarding the effect of the lasers. For experiments involving Ps with extended lifetimes against annihilation, the *B* parameter is set to later times which enables us to capture delayed annihilation events related long lived Rydberg states of Ps. The presence of long lived atoms that are traveling through the chamber can be determined from later annihilation caused by collisions, or a lack of signal related to atoms which outlive the window *B* - *C* or move out of view of the detector. The value of *C* is less critical and is normally selected at the limit of a measurable signal.

A (50 x 38 x 25)mm lead tungstate ($PbWO_4$) scintillator, coupled via a 150 mm long light guide to a PMT makes up the primary detector.

The light guide is a 50 mm wide acrylic rod which provides a suitable distance between the PMT electronics and the magnetic field that surrounds the target region. A second detector comprised of a 10 x 10 array of 4 x 4 x 20 mm LYSO crystals is also used for SSPALS. This detector gives a higher signal to noise ratio than the $PbWO_4$, especially for experiments involving long lived Rydberg states which is due to a higher light output. However, the $PbWO_4$ detector has a far superior time resolution, due to a shorter decay time (~ 10 ns, compared with ~ 40 ns for LYSO). This provides a clearer picture of processes occurring on short time scales such as *o*-Ps formation and annihilation following positron impact with the target. This decay time is still not short enough to resolve the very short lifetimes of positrons in dense solids, or to distinguish between the instantaneous annihilation events and those of *p*-Ps decay. However, this detector is selected for live monitoring of the experiment as any effect on Ps formation due to, for example, an issue with the bunching, or RW compression will have a more obvious effect on the lifetime spectrum. These effects can be hidden in the LYSO spectrum due to the reduced time resolution. Example spectra for typical laser excitation schemes (see chapter 4) for both detectors are shown in figure 3.2.

Figure 3.2(a) and (b) compare data for direct ionisation of Ps following excitation to $n = 2$. The increased temporal resolution of the $PbWO_4$ is apparent as the distinction between the prompt peak and the events at later times is clear. Also the reduction in annihilation γ-rays at all times after the prompt peak is more prominent than that of the LYSO, where the difference is not visible in the top panel until around 200 ns. It is therefore somewhat surprising that the LYSO still has an increased signal to noise ratio for this process. (c) and (d) compare data for the excitation of Ps to the n = 14 Rydberg state. Here the annihilation signal comes much later, when the atoms crash into the chamber walls, and this is made possible by the increased lifetimes. These processes that occur on increased timescales are easier to see in the LYSO background subtracted spectra.

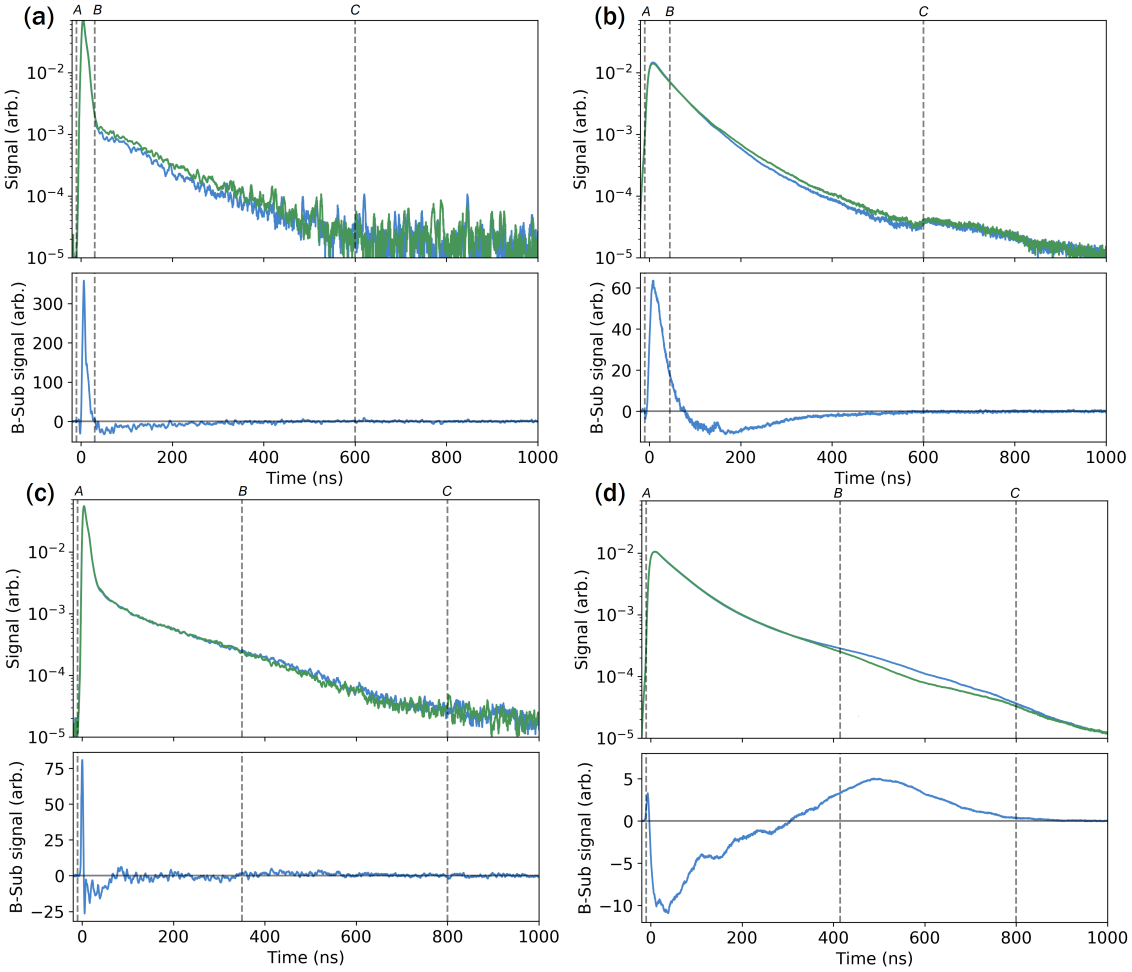

Figure 3.2: (a):Lifetime spectrum and subsequent background subtracted trace following photoionisation of $n = 2$ Ps obtained via the $PbWO_4$ detector.(b): Data obtained at the same time as in (a) with the LYSO detector.(c):Lifetime spectrum and subsequent background subtracted trace following excitation from n = 2 to n = 14.(d): Data obtained at the same time as in (c) with the LYSO detector, the clear bump at around 500 ns shows the LYSO to perform better for long term processes. All plots indicate the integration windows with vertical dotted lines.

Changes in the lifetime spectrum due to the effect of a probing tool such as a laser is quantified with the 'S_γ parameter'. This quantity is given by,

$$S_\gamma = \frac{f_{bk} - f_{sig}}{f_{bk}}, \tag{3.2}$$

where f_{sig} and f_{bk} refer to the delayed fraction (f_d, equation 3.1) when there is a signal, and there is a no signal during a background measurement respectively. Figure 3.2(a) ($PbWO_4$) gives $S_\gamma = 20 \pm 0.86$ %, with a signal to noise ratio (SNR) of 14. Whereas with the LYSO S_γ is lower (3 ± 0.45%) but more importantly there is an enhanced SNR = 20. The LYSO excels when comparing 3.2(c) and (d), where the S_γ and (SNR) are -12 $\pm$0.6 % (5.5) and -30 $\pm$0.4 % (33) for $PbWO_4$ and LYSO respectively. The increased signal to noise ratio of the LYSO detector enables faster acquisition times due to higher quality data with increased statistics.

3.2 Single event counting and the use of micro channel plates

For some experiments where a few atoms are registered in a location away from the excitation region, we employ a single event counting scheme. Rydberg Ps has an extended lifetime and this enables manipulation of the motion of these atoms via interactions with the exaggerated electric dipole moments (equation 1.3). Atoms that are guided with electric fields are recorded using a threshold triggering system. Guided atoms can be detected with a scintillator and PMT, where a registered event will exceed set threshold conditions related to the recorded voltage and time width of the recorded signals. The recording window is associated with the flight time of the atoms. An MCP is also used for registering events associated with guided atoms.

An MCP consists of several million hollow microchannels [Wiza, 1979]. These channels are typically made of leaded glass and are packed together in an array.

Each channel opening is typically ~ 10 μm in diameter. If a particle strikes the interior surface of one of the channels with enough kinetic energy a number of secondary electrons will be liberated from the material. These electrons will experience subsequent impact within the channel and likewise produce more secondary electrons inducing an avalanche effect. A large current amplification can take place if a suitable electric field is applied between the front and back of the plate. This is normally achieved with metal rings that hold the plate (or plates for higher gain) in compression. The channels are coated with a conducting material, so that the electric field may be applied along the channels. The MCP is stacked onto a suitable anode, which may be a metal plate, a phosphor coated screen for position sensitive imaging, or an array of electrically isolated wires also for position sensitive detection.

Two types of MCP were used in this study and their differences consist of the level of maximum gain and the choice of anode material. For imaging the positron beam (see chapter 2) a single plate MCP and phosphor screen assembly was used. Charged particle detection using an MCP like this is straightforward as the front plate can be biased to accelerate the particles toward the detector. The amplified electron current is then accelerated toward the screen. Upon impact, electron-hole pairs are excited and they de-excite through emission of photons. The phosphorescent material in this detector is P43 (GdO_2S:Tb). Visible light peaked at a wavelength of 545 nm is emitted from the screen and is imaged using a digital CCD camera programmed to expose during the decay time of the phosphor glow which is ~ 650 µs.

A double plate MCP was used to detect individual Ps atoms following their excitation into Rydberg-Stark states and electrostatic guiding away from the excitation region (see chapter 4). This detector is shown in figure 3.3.

The two plates were arranged as a chevron to enable secondary electron transport through the detector. With the two plates the minimum gain of this detector is increased to $\sim 10^8$, from $\sim 10^4$. Which is essential for the detection of neutral atoms of a relatively low internal energy. The anode in this case is a solid metal

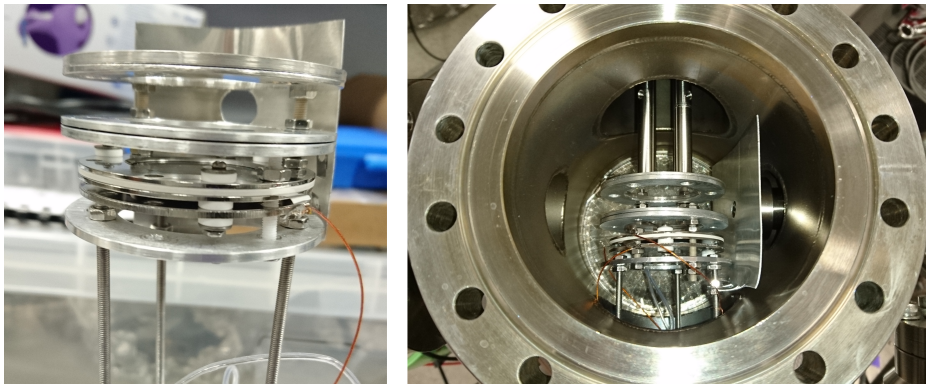

Figure 3.3: Left: Photograph of the two-plate high gain MCP with additional electrodes for the purpose of electric field control. Right: The detector in place for receiving guided Ps atoms.

plate, the detector is therefore used for time-of-flight measurements as avalanche currents induced by atoms striking the detector are monitored by an oscilloscope. MCPs in general have fast response times of less than 1 ns.

Similar timing measurements can also be performed using the phosphor screen anode. In both cases the anode signal is sent to the oscilloscope via a high pass filter. Example time-of-flight data for guided atoms is shown in figure 3.4.

3.3 Hardware control

We have utilised some of the vast capabilities of LabVIEW to create a programmable and automated system which has the ability to run experiments over large parameter spaces whilst monitoring, and reacting to environmental changes. The 'Oskar' (Orchestrate Sequences Keep Attribute Record) is a collection of LabVIEW virtual instruments (vi) designed to systematically control hardware and acquire and organise data which was written by Dr Adam Deller. It was developed, tested and implemented during the course of this study and is available for download via Github (https://github.com/PositroniumSpectroscopy). Sequences of data col-

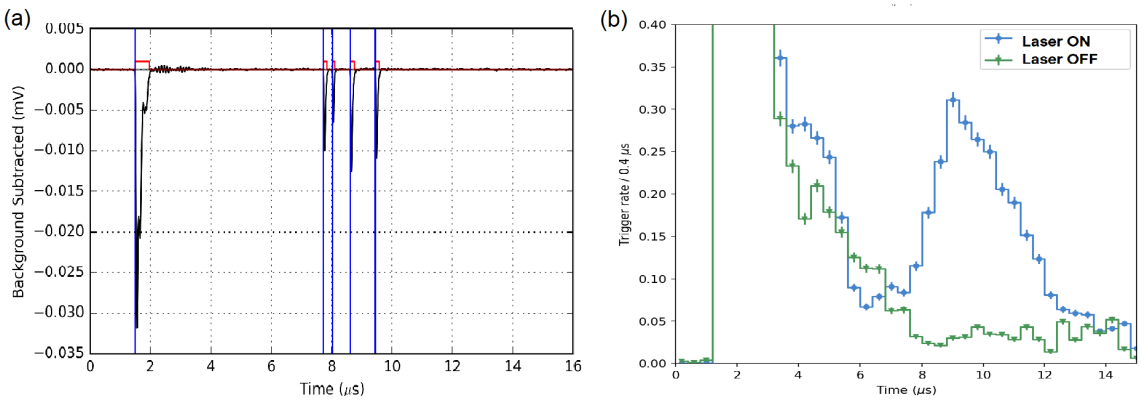

Figure 3.4: (a):A smoothed single oscilloscope trace following positronium impact with an MCP. Here four events are detected following excitation to low field seeking sub states of n = 14 and electrostatic guiding to the detector with a quadrupole. The vertical blue lines indicate the position of a registered event. The large feature at the start is due to rf pickup from HV solid state switches and is ignored. (b) The average rate of triggers received at the MCP as a function of time compared to a background taken with the Rydberg Ps excitation laser off resonance.

lection over varied parameter spaces are conducted by one master program. The sequencer vi is designed to read a file which is essentially an experiment script. The file contains lines of experimental variables such as laser wavelength, the applied voltage to an electrode, or the time of a trigger pulse. This vi does not control hardware, it merely sends the required setting to a variable vi (VAR) which has control of a specific device. For example, the purpose of the script may be to vary the frequency and amplitude of the sinusoidal waveform for the purpose of rotating wall optimisation. The sequencer does not know what these parameters are and the naming of them is arbitrary. The sequencer sends out a message to all running VAR programs saying 'The variables related to the rotating wall are to be set in this way'. The sequencer will then wait for the relevant VAR program to respond with a message that the values have been set. In the rotating wall example, the VAR vi will be the program controlling the arbitrary waveform generator. Some VAR programs are required to run on a loop which reads the value back from the hardware after it has been set and only gives the OK signal to the sequencer once

a condition has been met. This is to account for slow processes such as voltage ramping times. Once all the VAR programs have completed their tasks for a given line the sequencer will then wait in acquisition mode for a defined period before moving on to the next line. Each line has a sequence ID which is time stamped. If there are other programs running which are monitoring equipment such as oscilloscopes, cameras or other sensors, the data from these programs will be compiled into a single array which contains all of the relevant information from a sequence such as the line number, the parameters which were set, and the number of repeats.

The data files are then processed separately offline where averaging over repeats, SSPALS analysis, counting, or image processing and plotting can be performed. In the case of the above example concerning the rotating wall, one might wish to average oscilloscope waveforms and plot the mean pk-pk voltage of annihilation γ-ray signals against the varying sinusoidal values as this gives an insight into the efficiency of the trap under the changing conditions. An example of this is shown in figure 2.5. This particular sequence was run continuously for 12 hours, it contained 1021 lines which covered the broad, two dimensional parameter space.

Chapter 4

Laser Spectroscopy of Positronium

Progress in the field of laser spectroscopy of Ps has been limited in the past and this is mainly due to the availability of suitable positron sources, and hence Ps atoms. Some experiments were done using magnetic bottle traps [Chu *et al.*, 1984] or intrinsically pulsed linac based beams [Howell *et al.*, 1985; Ziock *et al.*, 1990a]. The development of the Surko buffer gas trap [Danielson *et al.*, 2015; Surko *et al.*, 1989] (See chapter 2) solved the problem of limited positrons but the field still remains under-explored. Laser excitation of Ps holds many benefits and it allows us to measure the Ps kinetic energy via Doppler spectroscopy. Excitation with laser pulses also allows us to extend the Ps lifetimes against annihilation, which provides time to perform advanced experiments.

4.1 Laser system

The laser system is comprised of one solid state laser, an Nd:YAG with a fundamental wavelength of 1064 nm, and two dye lasers which are used to produce tunable frequency pulses for Ps laser spectroscopy experiments. One dye laser is pumped with the third harmonic of the Nd:YAG (λ = 355 nm up to 160 mJ/pulse). This laser is operated with courmarin 102 dye which can produce light between $\approx$ 455 and 495 nm in wavelength with the peak efficiency at $\approx$ 475 nm. Three SF10 glass prisms make up the dispersive element inside the resonator. The laser is tuned to produce pulses near λ = 486 nm which are frequency doubled using a Barium Borate (BBO) crystal. The output of this laser comprises of ~ 6 ns (FWHM) pulses of UV light with λ ~ 240 - 245 nm and a $\Delta\nu \approx$ 85 GHz frequency bandwidth. This intentionally wide bandwidth provides some spectral overlap with Doppler broadened Ps. The doubling efficiency is controlled by varying the phase-matching angle of the BBO crystal. This enables regulation of the output energy as the laser wavelength is varied over the $1s$–$2p$ transition in Ps. This laser outputs fluences up to $\approx$ 2 mJ cm^{-2}.

Residual radiation from the Nd:YAG second harmonic (λ = 532 nm) can be used to photoionise $2p$ Ps via resonance enhanced multi-photon ionisation (REMPI) [Demtröder, 2003], or in the case of semiconductor targets, enhance the production of ground state Ps (see chapter 5). 532 nm pulses can also be used to pump a second pulsed dye laser operated with styryl-8 dye. The fundamental output of this laser gives up to 15 mJ cm^{-2} of IR light in the range 730-750 nm and it is used to drive $2p$-nd transitions in Ps.

The UV radiation and the secondary pulses (532 nm or IR) cross paths in front of, or enter a Ps converter target, for studies of vacuum Ps or confined Ps respectively. A schematic of the pulsed laser system is shown in figure 4.1

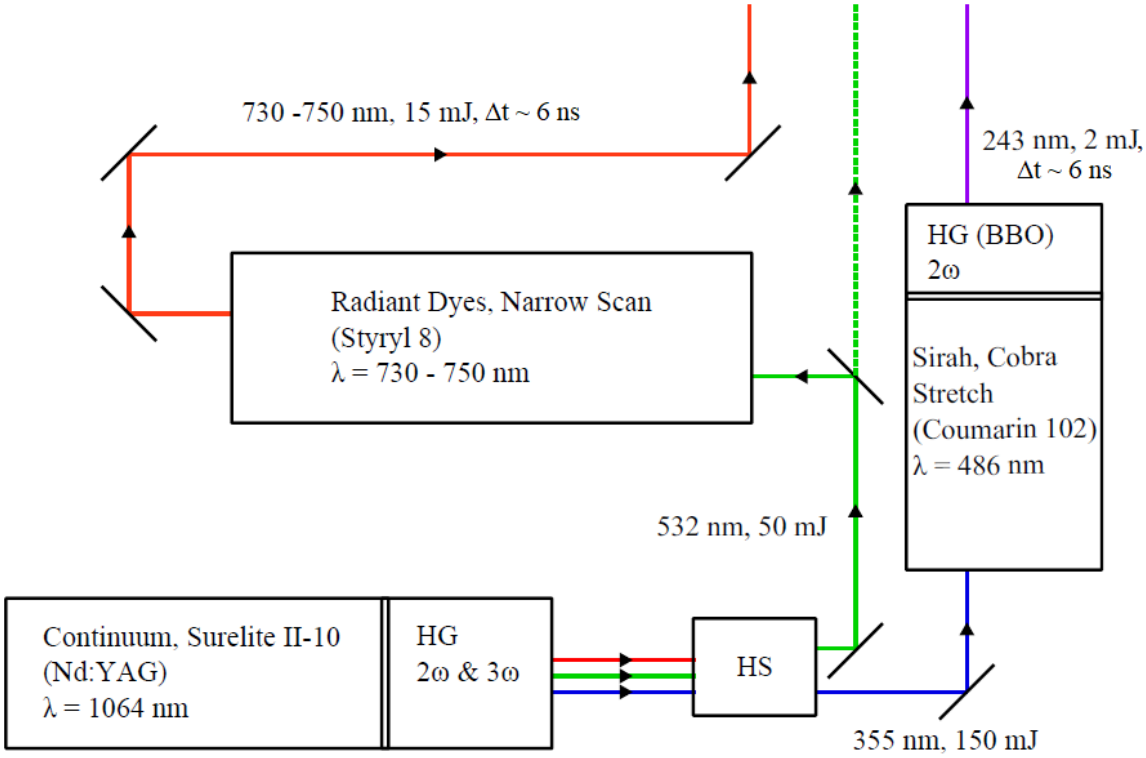

Figure 4.1: Laser system schematic with harmonic generation (HG) and harmonic separation (HS) units. Either 730-750 nm or residual 532 nm laser pulses can be sent the the vacuum chamber for interaction with UV excited Ps. The UV and IR pulses are temporally overlapped at the chamber. When using 532 nm pulses, the path length is extended to match the UV with an optical delay line.

4.1.1 Laser timing

A system which is suitable for laser spectroscopy of Ps has been developed. We have achieved this goal by sending suitably timed laser pulses to the vacuum chamber, where *o*-Ps is confined within a sample or emitted into vacuum. The orientation of the target with respect to the positron beam and laser pulses for a typical experiment is shown in figure 4.2.

There is a suitable delay between the firing of the Nd:YAG Q-switch and the trap opening. This is done to allow a transit time for positrons from the trap to the target via the buncher. The laser arrival time is tuned to achieve the largest laser interaction signal, as measured with SSPALS (see chapter 3) an example is shown for a 1*s*-2*p*-ionisation scheme in figure 4.3.

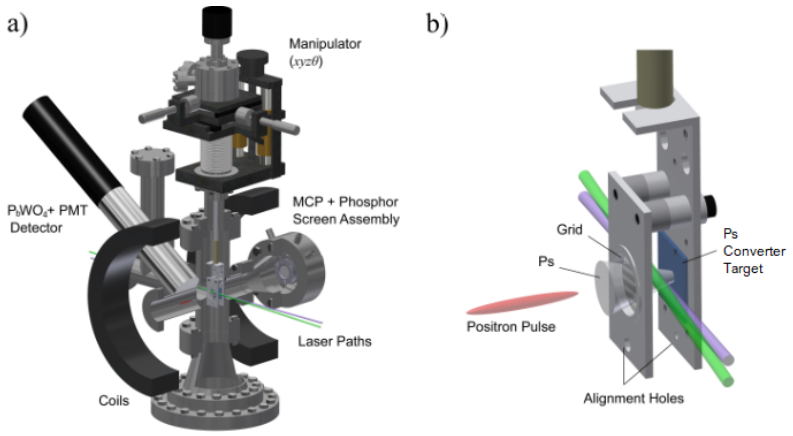

Figure 4.2: (a) Positronium-laser interaction chamber. Two coils surround the chamber producing a magnetic field at the target of ~ 13 mT. The target is raised out of view of the positron beam whilst performing trap diagnostics using the MCP. (b) Zoomed target mount. The target is sometimes placed behind a tungsten grid which is 97% transmissive. Ps atoms can be produced and reflected back into vacuum where they can interact with the laser pulses. The incoming positron pulse has a time width comparable to that of the lasers, which ensures good temporal overlap between the lasers and the emitted Ps. The 2 mm wide alignment holes at the bottom of the mount allow measurement of the positron pulse size whilst imaging the positrons arriving at the MCP see chapter 2 [Cooper *et al.*, 2015].

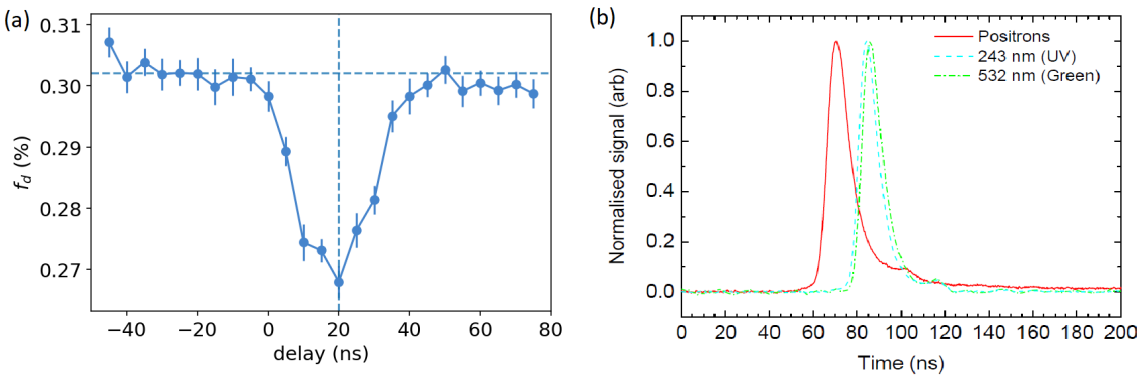

Figure 4.3: (a):Variation of the laser trigger time relative to positron release and the effect on the delayed fraction (f_d). The time axis has been scaled for clarity. (b): Plastic scintillator response showing an approximately 20 ns delay between the positron and laser arrival at the target. This was a suitable delay for the photo-ionisation of positronium as shown by the lowest value of f_d in (a) but this time will vary depending on the type of target and the laser position [Cooper *et al.*, 2015].

In figure 4.3, the laser initially arrives at the target chamber before the positrons and is therefore too early and this provides a background measurement. There is a constant delay between the flashlamp and Q-switch and the trigger times for both of these are moved together to change the arrival time of the lasers at the chamber. The annihilation γ-ray and laser pulse timing is monitored with a plastic scintillation detector or Si photo diode detector. If using a plastic scintillator, it is positioned such that it is in view of the annihilation radiation from the target in addition to diffuse reflected light from the laser pulses, which enter the scintillator through a small pinhole. The anode signal of the PMT coupled to the plastic scintillator is recorded with a digital storage oscilloscope. Figure 4.3(b) shows a delay of $\approx$ 20 ns between the positron and laser arrival time. This delay was optimum for photo-ionisation of Ps emitted into vacuum as it yielded the biggest interaction signal, S_γ, and signal-to-noise ratio. The optimal trigger time will vary depending on the type of target (see chapter 5), and the laser position with respect to the target. There is also a dependence on the implantation energy of the positrons which is related to the speed of the emitted positronium and its emission time.

4.1.2 Doppler broadened $1s$-$2p$ transition

Due to the very low mass of Ps, there is large Doppler broadening of atomic transitions at the typical Ps kinetic energies produced in the lab. This can affect the precision of a spectroscopic measurement. Doppler broadening of atomic transitions in Ps make laser spectroscopy challenging. This is due to laser bandwidths being typically much narrower than the transition that one is attempting to excite. There is a compromise between signal strength and resolution. For example, the 243 nm Lyman-α transition in Ps has a natural linewidth of 50 MHz is drastically increased to $\sim$ 460 GHz via Doppler broadening at room temperature. Excitation of the the Lyman-α transition in Ps with a narrowband laser at room temperature would be very difficult due to minimal overlap in frequency.

Elimination of some issues associated with Doppler broadening can be achieved following the two-photon, Doppler-free technique which was the first observation of Ps laser excitation by Chu *et al.* [1984]. The 1^3s_1-2^3s_1 interval was measured using two photons which reduced Doppler effects to the second order. Another approach is to increase the frequency overlap of a broadened transition. It is possible to obtain solid-state UV lasers with large ($\sim$ 200 GHz) bandwidths [Deller *et al.*, 2015a]. Alternatively, prisms can be used [Cooper *et al.*, 2015; Ziock *et al.*, 1990b] or high-order gratings [Cassidy *et al.*, 2010a] as dispersive media which produce light from dye lasers with bandwidths up to 100 GHz.

A single-photon, Doppler broadened Lyman-α $1s$-$2p$ transition was first achieved by Ziock *et al.* [1990b], who by using a frequency doubled, pulsed dye laser were able to saturate the 1^3s–2^3p transition in Ps with a laser linewidth $\approx$ 350 GHz.

We have also saturated the 243 nm, 1^3s–2^3p transition in Ps with the frequency doubled, wide bandwidth ($\Delta\nu \approx 85$ GHz) UV laser with pulse fluences above 500 μJ cm^{-2}. The saturation curve for the transition at resonance is shown in figure 4.4(b). Detection of the $2p$ states excited by the laser is achieved by their immediate ionisation with the residual 532 nm pulses at $\sim$ 25 mJ cm^{-2}.

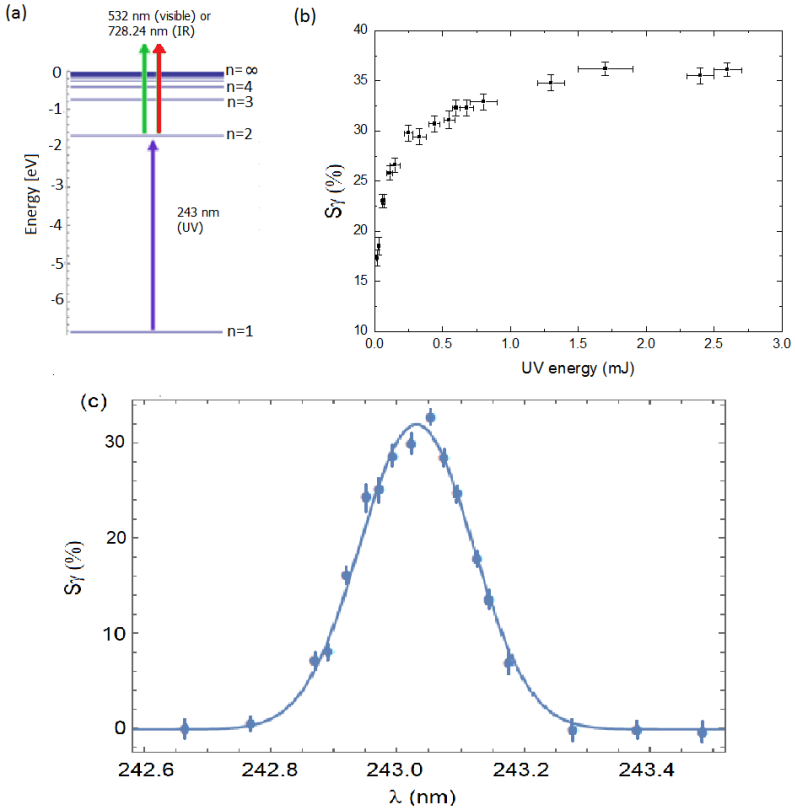

Figure 4.4: (a) $1s$-$2p$-ionisation via a two-step Doppler broadened scheme. 243 nm light drives Ps from the ground state to n = 2, then 532 nm light drives the Ps to the ionisation band where it is detected via changes in the SSPALS lifetime spectrum. IR pulses shorter than $\sim$ 730 nm can also drive $2p$ states to the ionisation band. (b) Measured intensity of the $1s$-$2p$ transition in positronium, showing saturation above $\sim$ 500 μJ cm $^{-2}$ of UV power. (c) $1s$-$2p$ line shape for Ps emitted into vacuum following the implantation of 5 keV positrons into porous silica.

Without the ionisation laser and in the absence of magnetic quenching, the $2p$ states would decay back to the ground state ($\tau \sim 3.2$ ns) and this process would go unnoticed in the lifetime spectrum.

Changes in the lifetime spectrum are quantified using equation 3.2, as explained in chapter 3. Figure 4.4 (c) shows S_γ as a function of the UV wavelength with $\sim 700\ \mu$ J cm^{-2} pulses. This enables a measurement of the spread in Ps velocities along the direction of propagation of the lasers. A Gaussian function has been fitted to the data which is of the form $A\ exp[-(\lambda-\lambda_0)^2/(2\sigma^2)]$. The rms speed in the direction parallel to the laser can be estimated with the assumption that the profile is dominated by non-relativistic Doppler broadening where

$$v_{RMS\parallel} = \frac{c\sigma}{\lambda_0}. \tag{4.1}$$

The line shape in figure 4.4(c) was measured following the implantation of 5 keV positrons into porous silica. $v_{RMS\parallel}$ is dependent on the type of Ps converter used and the energy of the incoming positron beam (see chapter 5). With the target and laser orientation as shown in figure 4.2, the line is centered at 243.03 ± 0.02 nm and has $\sigma = 0.089 \pm 0.002$ nm corresponding to a $v_{RMS\parallel}$ of ~ 110 km s^{-1} in the direction of the laser, which is representative of the slowest Ps produced during the course of this study.

4.2 Rydberg positronium

Many experiments can be done with Ps atoms in both the $1s$ and $2p$ states as shown in the following chapters. However, there is a great desire to increase the lifetime of Ps as this enables experimentation over longer timescales. For example, an ensemble of long lived Rydberg states of Ps would be useful for testing gravitational interactions with antiparticles [Cassidy and Hogan, 2014; Mills and Leventhal, 2002]. Antimatter is assumed to fall downwards, towards earth [Jentschura, 2013], however this has not yet been verified experimentally and any discrepancy between

the motion of matter and antimatter particles in a gravitational field would spark intense interest as it would challenge many accepted notions in modern physics.

Rydberg Positronium was first observed by Ziock *et al.* [1990a] who achieved $n = 14$ and $n = 15$ by first exciting Ps to $n = 2$ then optically pumping these states to higher n with an infrared (IR) laser. The signal to noise ratio of this method was later improved by Cassidy *et al.* [2012b]. The efficient production of long lived Ps atoms has benefits for many experiments including higher resolution time-of-flight [Jones *et al.*, 2015], separation of atoms from the point of creation and excitation, and Doppler correction methods [Jones *et al.*, 2014].

We have adopted the same technique, in that we initiate the $1s$-$2p$ transition with the pulsed UV laser ($\lambda = 243$ nm), and follow this with an excitation to Rydberg states with a pulsed IR laser ($\lambda = 730$ - 750 nm). The Ps energy eigenvalues can be calculated with precision by using the Bethe-Salpeter equation [Salpeter and Bethe, 1951]. However, an adequate approximation can be made using the Hydrogenic expression

$$E_n = -\frac{\mu q_e^4}{8h^2\epsilon_0^2}\frac{1}{n^2}, \tag{4.2}$$

where μ is the reduced mass given by equation 1.1 and this enables the equation above to be reduced to

$$E_{Ps} = -\frac{6.8eV}{n^2}, \tag{4.3}$$

which is approximately half of the value for Hydrogen [Ley, 2002]. The required energy to complete the transition from $n = 2$ to a higher n state can therefore be estimated via the energy interval between the two states. For example, the interval between $n = 2$ and $n = 12$ is approximately 1.65 eV. This translates to an IR wavelength of around 750 nm as shown in figure 4.5.

This two-step process has led us to the population of high n states in Ps from $n = 9$ - 30. We cannot resolve states above $n = 30$ due to Doppler broadening and

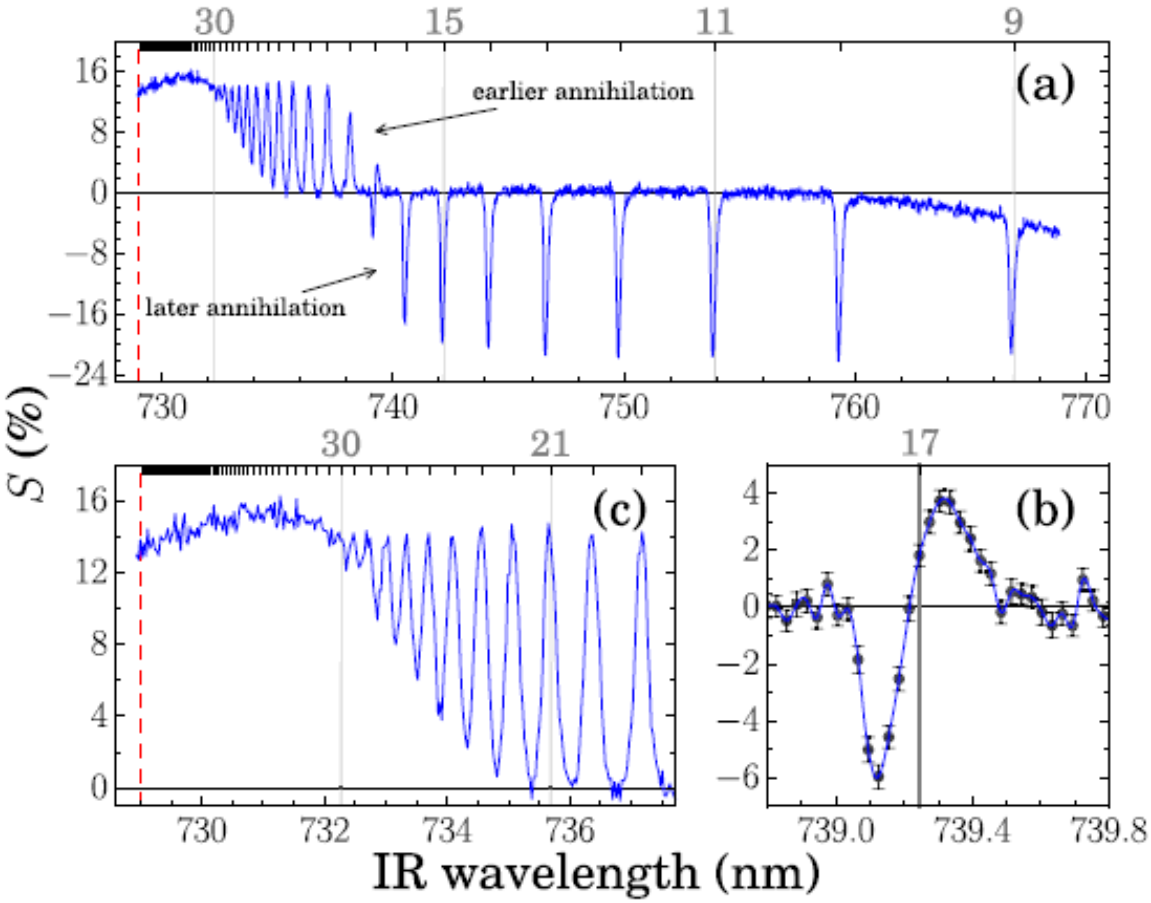

Figure 4.5: (a) Population of the states n = 9 - 30 following a two step laser excitation process. The data for n = 17 are expanded in (b) and $n \geqslant 19$ is shown in (c) The negative S values indicate long lived Rydberg positronium, where the positive values indicate field ionisation following exit from the grid. The error bars, not shown in (a) or (c), are of the same size as those shown in (b). Values of n are shown in the top axes. [Wall *et al.*, 2015].

the large laser bandwidth. These Rydberg atoms were prepared in a near zero applied electric field which is achieved using the grid shown in figure 4.2. Here the background is defined when the UV laser is on resonance with the $1s$-$2p$ transition (243 nm), but the IR laser is tuned off resonance, at all points between $n = 10$ and $n = 11$ (755 - 758.5 nm). The S_γ value is therefore a measure of the second step in the process, i.e the $2p$ states which are elevated to higher n levels.

There is some production of Rydberg states from broadband light, emitted from amplified spontaneous emission (ASE) this is the reason for the change in the background value between $n = 9$ and 10. At these wavelengths, we approach the limit of the Styryl-8 dye gain curve which is peaked at ~ 740 nm and drops to approximately half of the maximum efficiency at 720 and 765 nm. In this region the optical cavity is off resonance with the requested frequency, and a spontaneously emitted photon that is on resonance with the cavity receives the most gain from the active medium, causing an amplification of a broad frequency range of photons. The negative S_γ parameter for the $n = 9$ - 16 states represent a reduction in signal at earlier times. These states are not annihilating within the lifetime spectrum time windows A-B as explained in chapter 3. The effect of the laser is the production of Ps states which have extended lifetimes where some are detected at later times, and some move out of view of the detectors entirely. For the states higher than $n = 17$, the S_γ parameter is positive. These states are annihilating at earlier times due to ionisation from the electric field produced after the grid (see figure 4.2). The applied field that is required to ionise Rydberg states scales with n^{-4} [Gallagher, 1994]. The $n = 17$ line is both positive and negative, and is serendipitously split approximately in the middle. This is due to polarisation of the Ps atoms by the electric field, resulting in a partial splitting of states with both positive and negative Stark shifts [Wall *et al.*, 2015]. Basic control of this effect is shown in figure 4.6. This was achieved by altering the magnitude of the field seen by atoms which are transmitted through the grid. The small electric field in the excitation region remained by keeping the potential difference between the two constant. A small, constant potential difference between the target and the grid was applied, creating a field of 63 V cm^{-1}. This field, along with motional Stark effects cause polarisation

of the Rydberg atoms leading to weak Stark splitting [Gallagher, 1994].

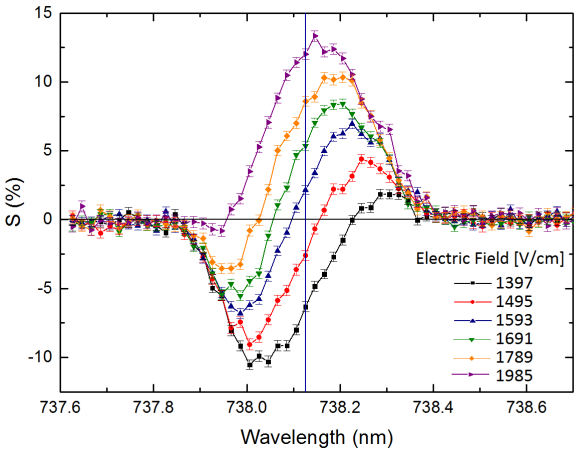

Figure 4.6: $n = 18$ peak measured with a constant 63 V/cm electric field in the excitation region, and a varying field outside the the grid. The vertical line indicates the predicted position of the $n = 18$ peak. Negative S_γ values indicate atoms which are passing though the grid, whilst positive S_γ values indicate atoms in Stark states which are field ionised [Wall *et al.*, 2015].

The longer wavelength components have negative Stark shifts, causing ionisation in weaker fields [Damburg and Kolosov, 1979]. Figure 4.6 shows that the suppression in transmission through the grid occurs first for the longer wavelength, negatively shifted states. For the outermost states, the ionisation field is approximately equal to the classical ionisation field [Gallagher, 1994],

$$F_{ion} = \frac{2R_{Ps}hc}{ea_{Ps}9n^4}, \tag{4.4}$$

where R_{Ps} is the Rydberg constant for Ps and is equal to $0.5R_\infty$, and a_{Ps} is the Bohr radius of Ps and is equal to $2a_0$. Equation 4.4 suggests that for Ps states transmitted through the grid which have negative Stark shifts at $n = 18$, the ionisation field is 1360 V/cm. The data in figure 4.6 shows that only the outermost, longer wavelength states are ionised by the field (positive S_γ).

For the outermost states with positive shifts, ionisation occurs at approximately $2F_{ion}$, which suggests a field of 2721 V cm^{-2} should completely inhibit transmission

of all stark states within $n = 18$, we see that practically all states within $n = 18$ are ionised by the field (positive S_γ) at a value of 1985 V/cm. This is lower than $2F_{ion}$ and this may be attributed to n-mixing of states with higher principle quantum number in the combined magnetic and inhomogeneous electric fields near the grid [Wall *et al.*, 2015].

We have also been able to resolve individual Stark states in the excitation region by increasing the electric fields in the excitation region up to 2 kV cm^{-1}, figure 4.7 shows examples of individual Stark-state resolution within the $n = 11$ manifold. This work, in addition to the data presented in figure 4.6, represent the first steps towards the development of atom optics for Ps for which Ps Stark-state selection is a useful prerequisite.

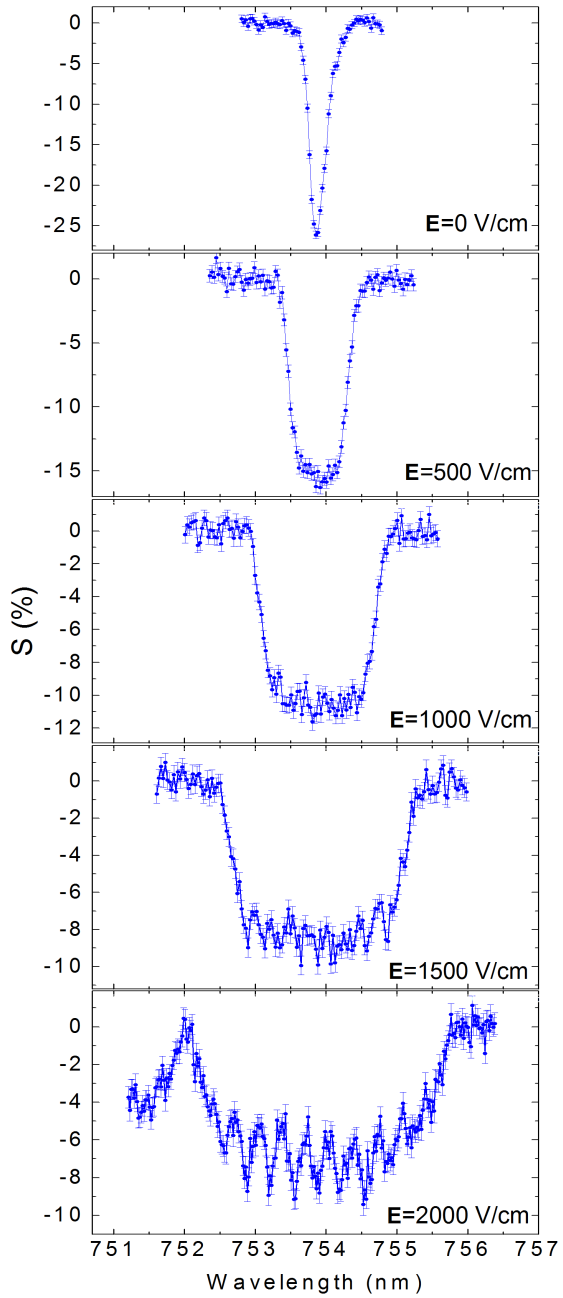

Figure 4.7: Resolution of individual Stark states of the positronium $n = 11$ manifold. This data was recorded in various electric fields ranging from 0 to 2.0 kV/cm. Drawn from Cooper *et al.* [2015]

Rydberg-Stark states with $k \neq 0$ have large electric dipole moments and with the application of inhomogeneous electric fields, large forces can be applied to these atoms [Gallagher, 1994; Hogan *et al.*, 2012]. By tuning the electric field in the excitation region, long lived Rydberg-Stark states of Ps can be produced which can in turn be spatially manipulated using guiding fields.

$n > 2$ Ps states with non zero angular momentum quantum numbers ($l \neq 0$) [Alekseev, 1958] have suppressed annihilation rates. Rydberg Ps is therefore primarily described by its fluorescence lifetimes. The fluorescence lifetimes for $n > 10$ is typically of the order of μs [Deller *et al.*, 2016b]. This is ideal for the transport of atoms, which typically have speeds less than 100 km s^{-1} over a few meters.

4.2.1 Guiding of low field seeking states

Following the production of Rydberg-Stark states of Ps and the separation of low, and high-field seeking states, we have demonstrated guiding of the low-field seeking states using a quadrupole guide which is shown in figure 4.8. These techniques and similar have been used on regular atoms for some time [Wieman *et al.*, 1999]. Employing these techniques for use on systems involving antiparticles has naturally been limited due to the difficulties associated with the production of such atoms. However, the recent advances in positron moderation, trapping, cooling, and manipulation are enabling progress.

Rydberg-Stark states of Ps were prepared following the two-colour two-photon excitation scheme outlined in the previous section. Initial experiments employed a 670 V cm^{-1} field in order to separate the n = 10 Rydberg-Stark states (see figure 4.7 for a demonstration of the similar separation observed for n = 11). Whilst this field is not strong enough to individually resolve Stark-states, it is however suitable for the optical selection of either high-field-seeking (hfs) or low-field-seeking (lfs) states. Selection of lfs or hfs is then achieved by simply de-tuning the IR laser to a shorter or longer wavelength component of the Stark-broadened line.

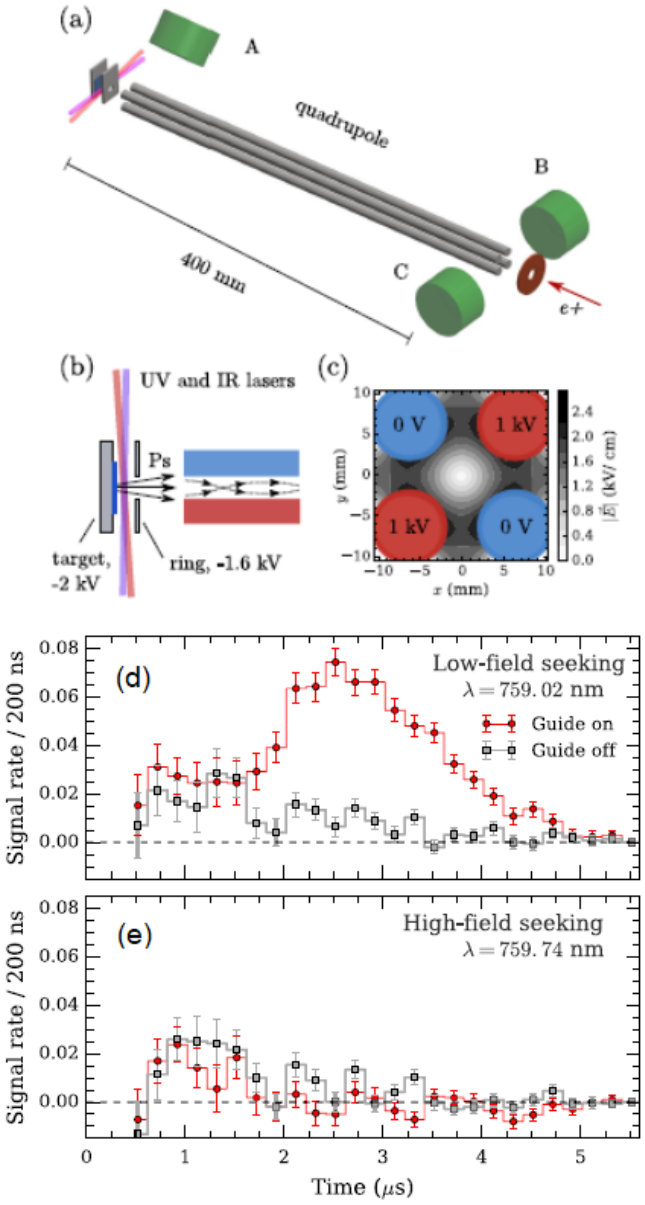

Figure 4.8: (a) Schematic layout of the quadrupole guide arrangement, indicating the Ps excitation region, and the gamma-ray detectors A, B, and C. (b) Expanded view of the excitation region, and (c) a contour plot of the electric field strength inside the quadrupole with 1 kV applied. (d) and (e) show background subtracted TOF data recorded by detectors B and C with 1 kV applied to the guide electrodes, for IR laser wavelengths corresponding to (d) outer lfs (k $\sim$ 6) and (b) outer hfs (k ~ -6) states of $n = 10$. [Deller *et al.*, 2016a]

Initial experiments were done using a 0.4 m quadrupole electrode positioned to accept Ps atoms made in a reflection geometry following their exit of the excitation region. As a result of the geometry shown in figure 4.8, the bias to the quadrupole rods was applied $\sim$ 150 ns after the positron beam had passed through it using a solid-state high-voltage switch. This was found as a suitable time to allow the positrons to pass through without deflection, for Ps to then be made in the sample and be emitted into vacuum, and finally be prepared into a Rydberg-Stark state and travel back towards the guide. The optimum time for pulsing the guiding field on was found in a similar way to the laser delay scan shown in figure 4.3. In this case the effects of pulsing the rods on whilst the positrons are still in the vicinity of the rods can be monitored via SSPALS at the target.

This guide enabled us to show that low-field-seeking Rydberg-stark-states of the $n = 10$ manifold can be guided by creating an inhomogeneous electric field along the flight path of the atoms [Deller *et al.*, 2016a]. By pulsing on potentials at the opposite poles of the guide, we are able to create a potential minimum at the centre. The electric field therefore increases near the rods which applies a force via the large electric dipole moment of the Ps. The excited states are produced predominantly with azimuthal quantum number $m_l = 1$, and even values of k, which is due to the polarisation of the excitation lasers [Wall *et al.*, 2015]. The lfs states are thus confined along the potential minima which runs along the centre of the guide manipulating the direction of travel to the forward direction. For the shifted IR wavelength of 759.02 nm it is expected that states with $k \sim$ -6 (610 Debye) are being produced [Hogan, 2013].

Detection of guided atoms was done via a single event triggering method using LYSO scintillators and PMTs. The technique is explained in chapter 3. This guide opens up the opportunity to perform further experimentation on atoms that have been transported away from the excitation region. This is advantageous if such experiments require different electric fields to the excitation region, or to be performed away from the potential interference from laser pulses. However, the atoms are transported in reflection along the positron beam axis which presents

some limitations on further experiments. These limitations were initially overcome by bending the positron beam off axis for Rydberg Ps lifetime studies [Deller *et al.*, 2016b]. Adding a 45^o bend to the guide also provided a method of transporting Rydberg-Stark states of Ps to an area away from both the Ps excitation region, and the positron beam axis [Alonso *et al.*, 2017]. The layout of this guide is shown in figure 4.9.

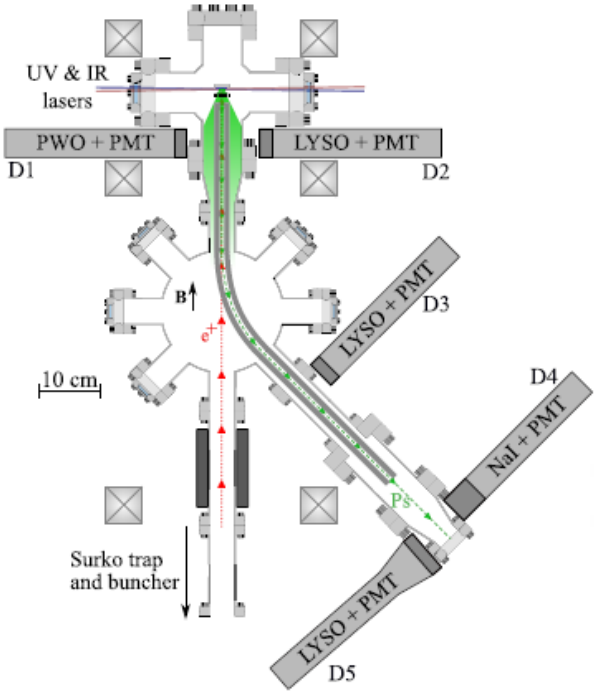

Figure 4.9: (a) Schematic representation of the experimental apparatus containing the curved guide. The positions of the five γ-ray detectors are indicated where D1 and D2 are used to monitor Ps atoms in or near the excitation region via lifetime spectroscopy, and D3, D4, and D5 are used to generate single-event TOF spectra. [Alonso *et al.*, 2017].

The bend adds a velocity selective component where atoms of a mean speed (kinetic energy) of ≈ 180 km s$^-$1 (~ 185 meV) enter the guide following implantation of positrons into a porous insulator (see chapter 5). The atoms selected at the bend have a longitudinal velocity of ~ 90 km s$^-$1 (~ 45 meV). These features

can be used to perform experiments in which guided Ps atoms interact with other species as explained in the next section.

A demonstration of the excitation and guiding of n = 14 lfs of Ps is shown in 4.10. An MCP was added to the end of the curved guide to aid detection following the methodology outlined in chapter 3

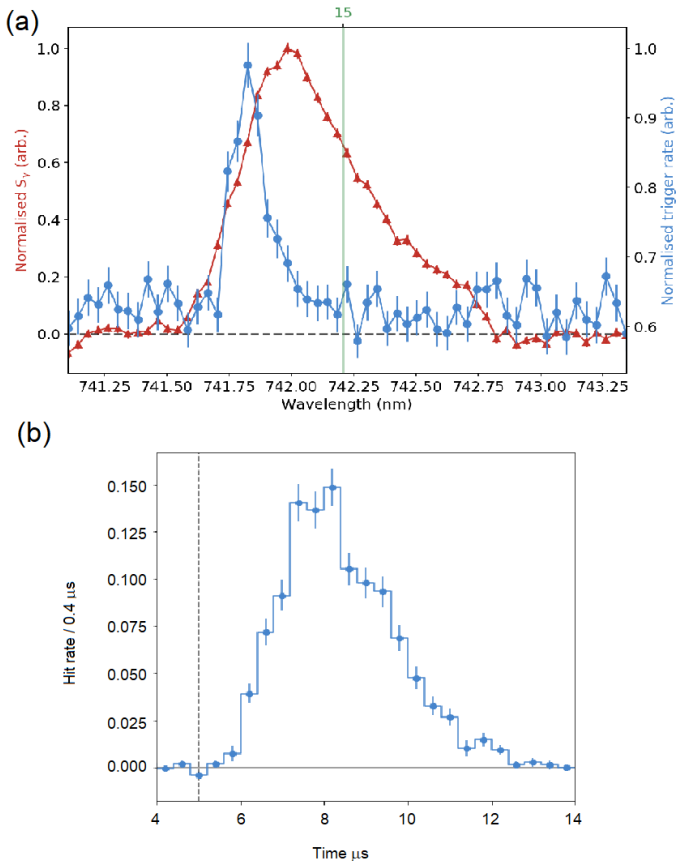

Figure 4.10: (a) Line scan of n = 15 excited in an electric field of $\sim$ 330 V cm $^{-1}$. The corresponding trigger rate as measured on the MCP at the end of the guide is also shown. The excess trigger rate is seen when $\lambda \sim 741.8$ nm showing the optimum excitation wavelength for low field seeking state production and guiding. (b) corresponding TOF spectrum for atoms that were successfully guided around the 45^o bend. The background subtracted count rate is 1.12 $\pm$ 0.02 Hz.

Here the applied electric field is $\sim$ 330 V cm $^{-1}$ which is suitable to optically select a subset of lfs states. The resulting trigger rate at the MCP is also shown which indicates the optimum detuned wavelength for producing lfs states that are accepted by the guide.

4.2.2 Crossed-beam charge-exchange scattering

Using the techniques for the electrostatic guiding of lfs Rydberg-Stark states of Ps outlined in the previous section, a charge exchange scattering interaction experiment was attempted. Collisions between Rydberg atoms and neutral species have been studied for decades, for example Hotop and Niehaus [1968]. The curved quadrupole guide was extended to accommodate an additional chamber which housed the MCP and facilitated the crossing of the Ps beam with an ion source. Argon ions were produced with a miniature ion sputtering gun, which produces a uniform, low density, inert gas ion beam with a diameter of 10mm. The ion beam was accelerated and focused with electrostatic lenses. The lens region was differentially pumped to reduce the Argon gas pressure in the scattering region.

The objective of this experiment was to observe the following reaction between Rydberg Ps, (Ps*) and a positive ion namely,

$$Ps^* + Ar^* \rightarrow Ar + e^+, \tag{4.5}$$

or the equivalent for He^+ as two gasses were available for ion production. In this reaction, the ion is neutralised by the Ps* electron leaving a free positron. The e^+ should be distinguishable from the Ps* as it can be accelerated into the front of the MCP producing a larger secondary electron current than the Ps*. Charge exchange processes involving Ps*, in particular the charge conjugate of the reaction producing Hydrogen [Merrison *et al.*, 1997],

$$Ps^* + p \rightarrow H + e^+ \tag{4.6}$$

have long been seen as a direct route towards efficient antihydrogen production [Darewych, 1987; Deutch *et al.*, 1988; Ermolaev *et al.*, 1987; Hessels *et al.*, 1998; Storry *et al.*, 2004].

For n = 14 positronium with a velocity of $\sim$ 90 km s^{-1} the cross section for the reaction above involving a stationary proton is expected to be of the order of $10^{-10}cm^2$ [Charlton, 1990; Krasnický *et al.*, 2016]. However, for a crossed beam experiment involving a diffuse ion beam, this will be an overestimate but it is expected that the adjusted cross section will still be very large. This assumption is made on the basis that the attenuation of the Ps* exciting the guide can be observed in the presence of diffuse background electrons which originate at the ion source as shown in figure 4.11.

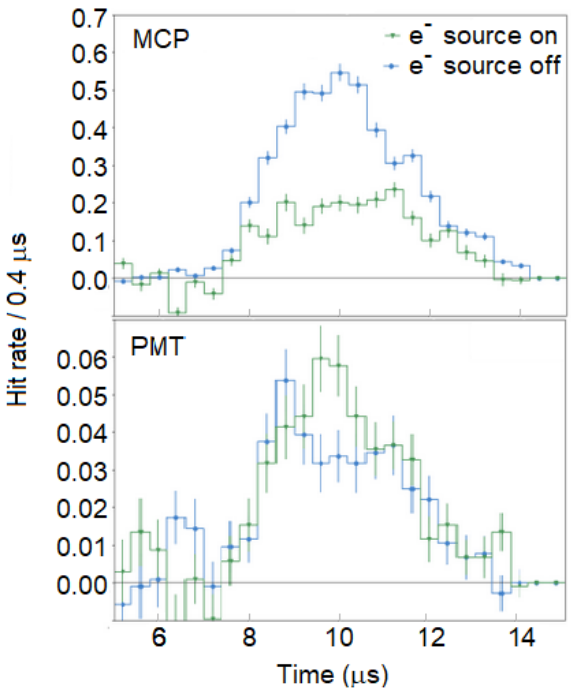

Figure 4.11: Attenuation of Rydberg Ps by an electron gas as seen on an MCP. The PMT detectors are indifferent to the interaction which can be suppressed with a permanent magnet. This confirms that Ps guiding is still active in the presence of the electron gas.

For a maximised ion current, the ion gun filament emission current is around 20 mA. However, this produces a large amount of background electrons which fully attenuated the guided Ps*. The data in figure 4.11 was recorded with a low emission current of 1 mA which produces a weak ion beam as measured with a Faraday cup. Here the Argon gas inlet is closed which suppresses ion production and allows only the background electrons to enter the scattering region. Figure 3.3 shows the end of the guide, field suppression plates, and double plate MCP. The interaction region is 2.5 cm across. A simplified schematic is shown in figure 4.12.

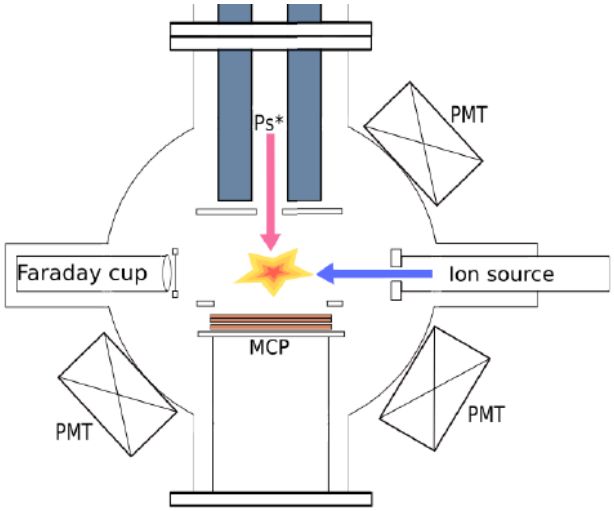

Figure 4.12: Scattering region following the guide exit. Ions and electrons are produced on the right hand side of the MCP. The inhomogeneous electric field generated by the rods is terminated by a grounded aperture. A second aperture that sits in front of the MCP allows control of the field at the location of the interaction. Three scintillation detectors with PMTs are situated outside of the chamber, the counts of which are summed.

With the background electrons present an attenuation of Ps* is observed at the MCP. The summed PMT counts remain constant with and without the filament on. This suggests that the Ps* is being guided successfully regardless of the presence of charges and that annihilation is occurring in a similar location to the MCP. Interactions involving Ps* and electrons can take several forms including ionisation or breakup, ground state Ps production via electron exchange, or production of the

Ps negative ion, Ps^-. The relevant cross sections for interactions with electrons for ground state Ps are given in reference [Ward *et al.*, 1987]. However, it is not trivial to determine which processes are taking place. Detection of reaction products can give insight into the scattering mechanism, for example, positron detection could indicate Ps ionisation is taking place. However, there are difficulties associated with this detection scheme as an applied electric field designed to direct positron reaction products to the detector may affect the electron trajectories which could in turn prevent the reaction from taking place. Background electron suppression would be essential in an experiment in which heavy ions are used as a scattering target. This may be achieved with electric and/or magnetic fields. The reaction could also be facilitated within an ion trap [Willitsch *et al.*, 2008].

Chapter 5

Positronium production and cooling

For some experiments it is advantageous to produce a large amount of cold Ps atoms, such as those concerned with the production of antihydrogen. Many different materials have been shown to produce Ps. From the early work of Canter and Mills who produced Ps on the surfaces of various solid targets [Canter *et al.*, 1974; Mills, 1978], to the more recent, observation of formation in SiO_2 [Nagashima *et al.*, 1998], silica aerogel [Nagashima *et al.*, 1995], mesoporous thin films [Liszkay *et al.*, 2008b], and positively doped silicon [Cassidy *et al.*, 2011b]. Porous materials are often selected as the target material for achieving a large Ps production fraction. Schultz and Lynn [1988], explain the theory of positron interactions with solids prior to positronium production. Upon impact between the beam and the target, several possibilities for interactions arise, including implantation into the material or back scattering away from it. If a positron is implanted into an insulator, it can diffuse through the material, losing energy through inelastic collisions. A diffusing positron will continue to lose energy until it annihilates, reaches the surface, forms Ps, or gets trapped in a lattice defect site where it will eventually annihilate. For metals and semiconductors, Ps production is not possible in the bulk due to the high electron density which screens the positron charge [Schultz and Lynn, 1988]. However, if a positron diffuses to the surface, the formation of Ps can occur via a number of processes.

5.1 Positronium formation in insulators

An insulator will allow Ps formation within the bulk of the material which can subsequently diffuse to the surface and be released into the vacuum. In any case the positron energy E_+ must exceed the ionisation energy of the medium E_i, minus the Ps binding energy

$$E_+ \geqslant E_i - E_{Ps} \tag{5.1}$$

to form Ps. Ps atoms can be produced in solid insulators following positron implantation into various materials [Canter *et al.*, 1974; Mills, 1979; Mills *et al.*, 1991; Paulin and Ambrosino, 1968; Rich, 1981; Sferlazzo *et al.*, 1988]. In many of these materials Ps is formed by interactions with the electrons produced by positron implantation [Tao, 1974]. The lifetime for Ps atoms formed in the bulk of many such materials is sub-nanosecond [Gidley *et al.*, 1999]. However, if such materials have open spaces in the form of pores, Ps atoms that are formed in their vicinity can diffuse into them enabling extended Ps lifetimes.

5.1.1 SiO_2

Ps atoms can be produced efficiently when positrons interact with fine powders of various oxides [Paulin and Ambrosino, 1968]. The Ps atoms diffuse to the grain surfaces [Brandt and Paulin, 1968] where they are emitted into vacuum with a kinetic energy related to the Ps binding energy, the band-gap energy, and the work functions of the electron and positron [Nagashima *et al.*, 1998]. In general, SiO_2 emits Ps into vacuum with approximately 1 eV of energy. Higher emission energies can be observed when surface-based formation processes are present [Sferlazzo *et al.*, 1987] as the initial Ps energy is reduced following collisions and this is absent in a surface based formation. Ps undergoes many hundreds of thousand collisions due to the typical Ps speed and the sample geometry [Ford *et al.*, 1976]. However, complete thermalisation within powdered materials requires very deep

implantation [Mills *et al.*, 1989; Nagashima *et al.*, 1995; Tianbao *et al.*, 1987]. It could be possible to create a powder blend that contains a heavy metal such as Pb for the purpose of increased collisional cooling and thermalisation, but this will be at the cost of an increased annihilation rate.

An increased thermalisation efficiency is however observed with variations of mesoporous SiO_2 assembled as thin films [Liszkay *et al.*, 2008b]. General explanations on the synthesis of such materials which undergo evaporation-induced self-assembly are given by [Brinker *et al.*, 1999; Grosso *et al.*, 2004]. SiO_2 is common but a variety of other materials can be used [Fischer *et al.*, 2005]. The use and study of mesoporous structures for Ps production has become increasingly important over the years. The fact the such materials facilitate the cooling and confinement of Ps has enabled measurements involving interactions between Ps atoms and the formation of the Ps_2 molecule [Cassidy and Mills, 2007c]. Figure 5.1 shows the possible fate of positrons implanted into mesoporous SiO_2, which are direct annihilation or Ps formation and annihilation in the *p*-Ps or *o*-Ps states, it is possible for the later to diffuse to the surface and be emitted into vacuum.

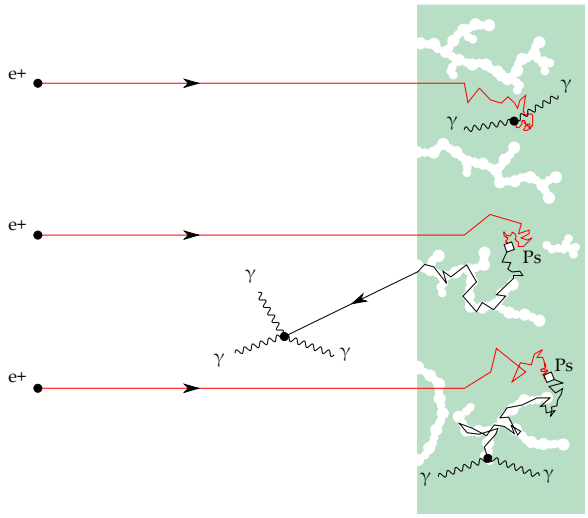

Figure 5.1: Possible outcomes following the implantation of positrons into mesoporous SiO_2 films. These include direct pick-off annihilation, Ps production, diffusion and escape into vacuum, or Ps production, diffusion and eventual decay inside a pore.

Mesoporous SiO_2 can be synthesised with various properties such as average pore size, overall porosity, and surface area. These materials provide a source of efficient, collisionally cooled Ps [Liszkay *et al.*, 2008a,b]. However, if the mean pore size is comparable to the Ps de-Broglie wavelength the Ps thermalisation is restricted. The Ps atoms become confined within the voids with an energy that depends on the size of the cavity. The Ps will therefore be emitted into vacuum with a non-thermal kinetic energy which is defined by quantum mechanical confinement [Cassidy *et al.*, 2010a]. Crivelli *et al.* [2010] measured Ps with 48 ± 5 meV energy emitted from a sample with a mean pore size of 4.1 nm, whereas a stronger confinement effect was observed within smaller pores (3.3 nm) as that emitted Ps with 73 ± 5 meV.

The SiO_2 samples used throughout this study were synthesised by Laszlo Liszkay at CEA Saclay France. The samples were made using the sol-gel method [Hench and West, 1990], with TEOS (tetraethyl orthosilicate) as a precursor to silicon dioxide. The triblock copolymer Pluronic® F-127 (poloxamer 407) was used as a template, following the method of Imperor-Clerc *et al.* [2000]. The porogen ratio was however twice as high (0.016 instead of 0.08 molar ratio). The F-127 and TEOS was mixed with ethanol, deionised water and HCl in a molar composition of $0.016{:}1{:}8{:}8{:}5 \times 10^{-5}$. The mixture was stirred at room temperature for 90 minutes, then deposited on a p-type Si single crystal wafer via 3000 rpm spin coating. The porogen was removed from by heating the samples to 723 K for 15 minutes in air. Porous voids are left behind as the porogen forms spherical micelles which undergo thermal decomposition. The SiO_2 walls are left behind formed from the TEOS precursor via hydrolysis. The pore surface exhibits silanol (Si-O-H) groups with a typical density of 4-5 OH/nm^2. Contamination from the decomposition products of the porogen can also be expected when annealing at temperatures below 773 K. These decomposition products are carbon based, and are mostly comprised of methoxyl Si-O-CH3 groups.

Doppler spectroscopy of Ps emitted into vacuum

To characterise the level of collisional cooling that Ps undergoes within a material, the kinetic energy can be measured via Doppler spectroscopy [Cassidy *et al.*, 2010a]. Residual light from the second harmonic (532 nm) of the Nd:YAG was used to photo-ionise Ps atoms in the n = 2 state, this scheme is shown in a simplified manner in figure 4.4 (a). The photo ionisation process decreases f_d as explained in chapter 3. This is because a positron that is liberated from a $2p$ positronium atom will be attracted back towards the target where it will likely annihilate.

Changes in the single shot lifetimes due to photo-ionisation were quantified by the parameter S_γ, equation 3.2. For this case the background is defined as f_d when the lasers are delayed with respect to the positron pulse by 1 μs, preventing the lasers from interacting with the Ps. Figure 5.2(a) shows S_γ plotted against the wavelength of the UV laser for varying positron energies. Here the UV excitation pulse is scanned over the 243 nm $1s$-$2p$ transition wavelength, whilst the ionisation pulse remains constant at 532 nm. The data are fitted with a Gaussian function, and the rms velocity is extracted via equation 4.1. This velocity was measured for positronium atoms emitted into vacuum following implantation into SiO_2 at various energies. Figure 5.2(b) shows that as the implantation energy is increased, the positronium velocity is reduced, indicating that Ps is being cooled through collisions during its diffusion towards the sample surface.

The highest positron impact energy (4.7 kV) gives a $v_{RMS\|} = 1.04 \pm 0.04$ x10^5 m/s, whilst the lowest positron impact energy (200 V) produces faster Ps, ($v_{RMS\|} = 2.7 \pm 0.2$ x10^5 m/s). Producing cold Ps is advantageous as it is difficult to spatially overlap a laser pulse with fast atoms without sacrificing the power density of the laser. A source of slow Ps would be advantageous towards experiments such as Stark deceleration of Rydberg Ps [Hogan *et al.*, 2012].

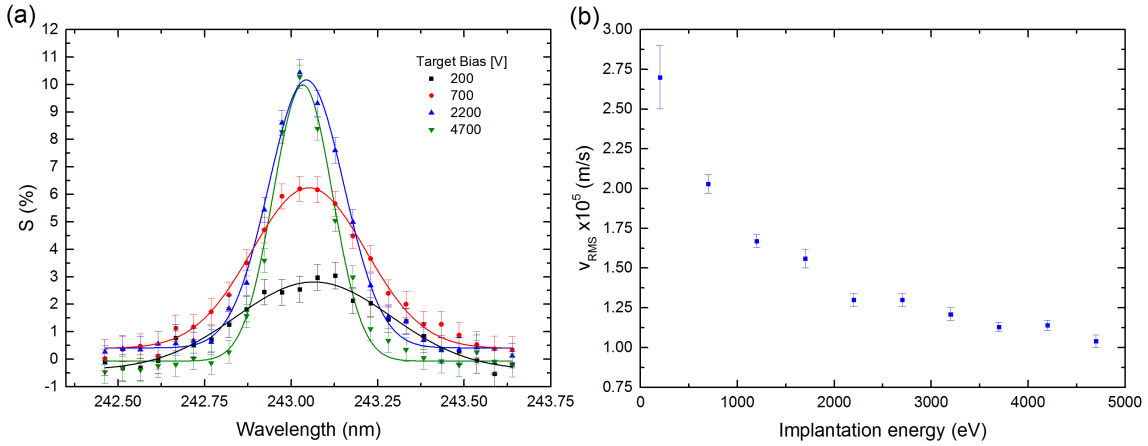

Figure 5.2: (a) Selected Doppler broadened line measurements of the $1s$-$2p$ transition in Ps, as measured by the photo-ionisation of the $n = 2$ state. The positron implantation energy is increased, leading to a narrowing of the line shape, due to an increase in Ps cooling within the bulk of the SiO_2 sample.(b) Ps cooling within the bulk is further evidenced by the reduction in the velocity component that is parallel to the direction of the lasers. [Deller *et al.*, 2015b]

Laser enhanced positronium time of flight

An extension to these techniques enabled us to measure the emission and flight times of Ps emitted from mesoporous SiO_2 samples. By sending the lasers through apertures and ensuring a good spatial overlap between the two beams (243 nm UV, and 532 nm visible) which ran parallel to the target mount, we were able to define the region in space where Ps atoms are excited and subsequently ionised. This Ps probing scheme followed the REMPI technique [Demtröder, 2003]. The target chamber was positioned as shown in figure 2.8 and the target mount is like that of figure 4.2 minus the grid electrode. Positrons were bunched directly out of the trap for this experiment. Here photoionised positrons are accelerated back to the target by the same electric field which defined the incident beam energy. The majority of these positrons ($\approx 70\%$) promptly annihilate creating an excess of γ-rays in the SSPALS spectra. The varying distance between the laser field and the target should not effect the timing of detected ionisation products (positrons) as even the slowest

of these particles will reach the target within 1 ns due to the large attractive -5 kV bias applied to the target.

Variations in the distance between the ionisation laser field and the face of the sample in addition to variations in the laser arrival time lead to a laser-enhanced positronium time-of-flight (LEPTOF) spectrum.

Figure 5.3 shows the excess annihilation signal caused by the laser in the form of bumps in the SSPALS spectra. The time that the bumps appear is changed with variations to the delay between the trap opening and the triggering of the laser. This value is then scaled relative to the mean arrival time of the positrons at the target.

The changes in the annihilation spectra are quantified in this case by the quantity W which is measure of the excess annihilation signal induced by the laser. W is given by,

$$W = \left[V(t)_{on} - V(t)_{off}\right] e^{t/142\,ns} \tag{5.2}$$

Where $V(t)$ is the mean signal during a 4 ns interval which is centred at the arrival time of the lasers. This quantity is measured when the UV wavelength is tuned on ($V(t)_{on}$) and off ($V(t)_{off}$) resonance with the $1s$-$2p$ transition (243.0 and 242.25 nm) for background subtraction. The exponential term considers the lifetime of o-Ps, which assumes a natural decay of 142 ns in vacuum.

The LEPTOF technique [Deller *et al.*, 2015b] allows one to determine the arrival time of a distribution of Ps atoms at a point in space defined by an ionising laser field. This time is relative to the mean implantation time of the positrons into the porous sample. This time is a convolution of the the time-width of the incident positron pulse, the Ps velocity distribution and the range of Ps emission times from the sample.

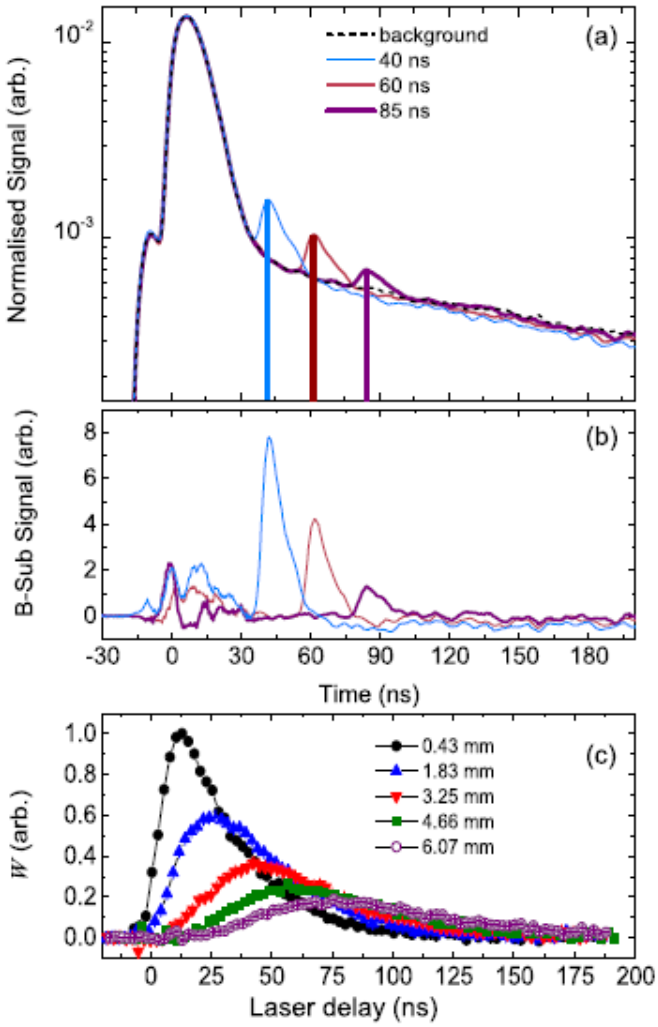

Figure 5.3: Above: Normalised SSPALS integrated between -3 ns to 350 ns showing the excess annihilations that are observed when the lasers meet the Ps atoms at different times. The traces represent an average of around 120 shots. The shaded regions represent the laser interaction window, which is 4 ns wide and centred about the laser arrival time. Middle: Background subtracted data from above. Below: *o*-Ps decay corrected ionisation signals as a function of laser delay time, plotted for varying distances between the target and the laser, this data is discussed in Deller *et al.* [2015b], figure from Cooper *et al.* [2015].

The data is therefore corrected to account for the slower atoms which transverse the laser field for longer and are therefore able to be photoionised over a broader timescale which leads to over counting to a degree inversely proportional to the speed of the atoms. To account for this, a correction function of t^{-1} was applied to the the data. The distributions were also truncated to a minimum time related to the maximum expected kinetic energy of 1.1 eV [Crivelli *et al.*, 2010], for each distance. In addition to this, the probability for interaction with the laser is also considered. This probability varies as a function of the speed of the atoms but is considered to be close to one for this combination of lasers for velocities less than around 300 km s^{-1}. The calculation is discussed in detail in [Deller *et al.*, 2015b] For the data shown here, the implantation bias was fixed at 5 kV which produced atoms with a mean rms velocity component through the path of the lasers of around 100 km/s. This velocity is increased at lower implantation energies as shown in the previous section.

The corrected data, which is shown in the bottom panel of figure 5.3 can be fit with an asymmetric double sigmoid function which is not based on a physical model, its selection is due to a good fit to the data. One can determine the mean flight time of the Ps atoms from the expectation value of the corrected fits. Extrapolation of the to the origin, or point of Ps emission gives the mean emission time of Ps atoms for the sample. For 5 keV positrons the implantation, diffusion and emission process is complete in around 10 ns.

Utilisation of the LEPTOF technique provides a measurement of the Ps arrival time at a point in space, the emission time from the sample, and the kinetic energy. However, the following experiments utilise the method of Doppler spectroscopy explained in the previous section.

Cavity induced shift of the 1*s*-2*p* line shape.

There is a great interest in the dynamics of Ps confined to small cavities as it resembles the appealing thought experiment proposed by Sommerfeld and Welker [1938], in which an atom is placed inside an impenetrable cavity. Ps is widely

used as a probe for studying nanoscale condensed matter structures as pick off annihilation processes reduce the Ps lifetime inside a cavity. The *o*-Ps positron can annihilate via a 2γ decay event with an electron of the cavity wall if a relative singlet state is realised [Brandt *et al.*, 1983]. This pickoff process depends on the local electron density in the bulk around the cavity and will thus have a strong dependence on the cavity size.

As well as sample probing and characterisation of porous materials, confined atoms may provide opportunities for recoil and Doppler free spectroscopy [Ido and Katori, 2003] as a result of their constrained motion. Ps confinement itself can be characterised via spectroscopy as shifts in atomic transition wavelengths arise following perturbations of the Ps internal wave function, with the centre of mass (cm) motion behaving classically [Cassidy *et al.*, 2011a]. There is also a contribution arising from the induced potential from the *o*-Ps positron and the wall electrons. The full perturbation is therefore a combined Ps centre of mass and relative coordinate wave function. The low mass of Ps in addition to the extra element in the perturbation leads to observed shifts that are much larger than those that would be observed for a heavier, normal matter atom in a similar cavity. A more complete, quantum mechanical treatment of these cavity induced effects on Ps is offered by Brown *et al.* [2017] where the effective collisional radius depends on the cm momentum.

Cassidy *et al.* [2011a] demonstrated both a large cavity induced shift and Dicke line narrowing effects [Dicke, 1953] in Ps confined within a mesoporous SiO_2 sample. The mean internal pore diameter of the material was ~ 5 nm [Crivelli *et al.*, 2010]. This was done via measurements of the Doppler broadened $1s$-$2p$ line shape both in vacuum and inside the sample. The inside measurement was conducted with the target rotated by 45^o relative to the incoming positron beam, which allowed the lasers to penetrate the sample. Here the resonant line was asymmetric and shifted relative to the unperturbed vacuum position. The line scan was repeated at a later laser arrival time revealing two distinct Ps populations. An asymmetric double peak was the result of the line scan taken inside the sample.

The measurements were decomposed into the sum of two Gaussians, both shifted from the unperturbed vacuum position.

This experiment was reproduced with a similar sample. The results, and the target geometry for the two measurements are shown in figure 5.4. In vacuum the measured $1p$-$2p$ line shape is centered at a mean wavelength of $\lambda_0 = 243.013 \pm 0.002$ nm.

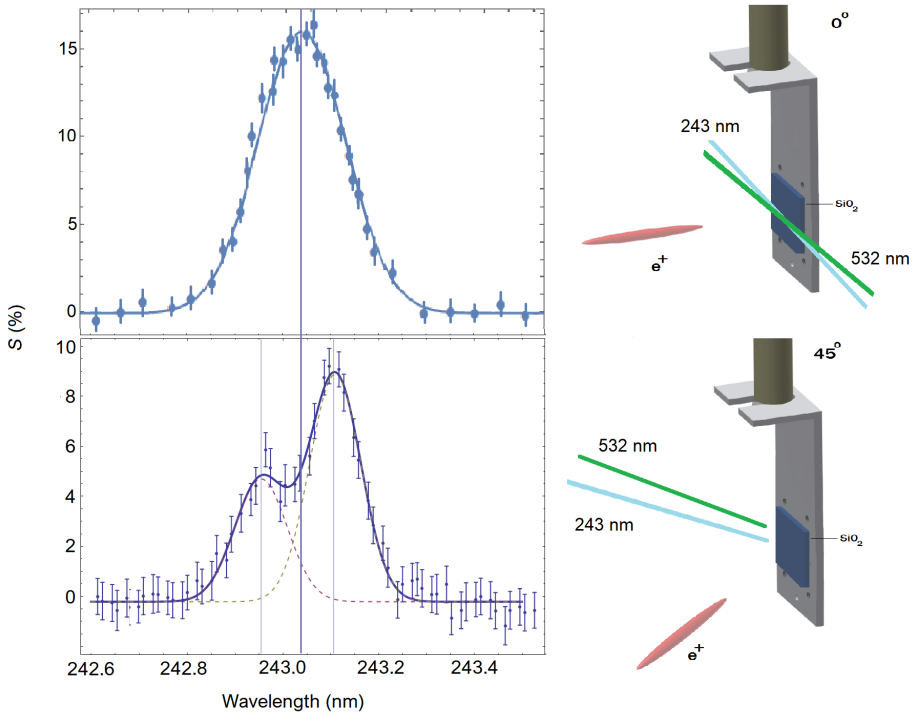

Figure 5.4: Above: Vacuum line scan showing the average unperturbed $1s$-$2p$ interval centered at $\lambda_0 = 243.013 \pm 0.002$ nm. Below: Cavity induced, and Doppler blue shifted peaks showing Ps excitation both inside and outside the sample. The average $1s$-$2p$ interval ΔE is larger than the unperturbed Ps. The sample geometry is shown on the right where the target was rotated relative to the positron beam axis.

When the laser is directed into the sample however, two shifted peaks are observed. The asymmetry of the two peaks confirm that the shorter wavelength component, centered at λ_{cavity}, is from Ps excited inside the sample. If the excitation was occurring in vacuum, an equal red and blue shift would be expected as the Ps travels towards and in the direction of the laser following its reflection from the substrate. The data was fitted with a double Gaussian, and was decomposed into two peaks which determined $\lambda_{cavity} = 242.954 \pm 0.005$ nm, giving $\Delta\ \lambda_{cavity} = 0.059 \pm 0.005$ nm. The average $1s$-$2p$ interval ΔE is thus 1.24 ± 0.07 meV larger than the unperturbed interval, which is in good agreement with the previous measurements of 1.26 ± 0.06 meV by Cassidy *et al.* [2011a]. This result verifies consistency of the mesoporous SiO_2 samples which originate from the same source.

Increasing the pore size

Larger pores will reduce the cooling limit imposed by the confinement energy but this is expected to be at the detriment to the Ps formation and cooling efficiency. This has been observed in macroporous silica films with pore sizes of 32-70 nm [Liszkay *et al.*, 2012]. Ps is formed in the bulk material of mesoporous thin films where typical lifetimes are sub-nanosecond [Gidley *et al.*, 1999]. For Ps to live long enough diffuse to the surface and be emitted into vacuum they must be formed very close to an internal void or pore. This is more likely for materials that posses smaller pores and are of higher porosity, as the thickness of the internal walls is lower on average.

Figure 5.5 shows this as an increase in the delayed fraction f_d, (see chapter 3) for both increasing porosity, and pore size. The decreasing bulk volume increases the probability of Ps formation in the vicinity of an open void. However, the mesoporous samples discussed in previous sections produce Ps with longer lifetimes, therefore higher f_d values which go up to 33 % when the samples are heated (see figure 6.10). The mesoporous samples have a mean pore size of 5 nm and a 60 % porosity, and this provides a higher probability for Ps to enter the interconnected pore network (see figure 5.1) where the Ps lifetime is extended.

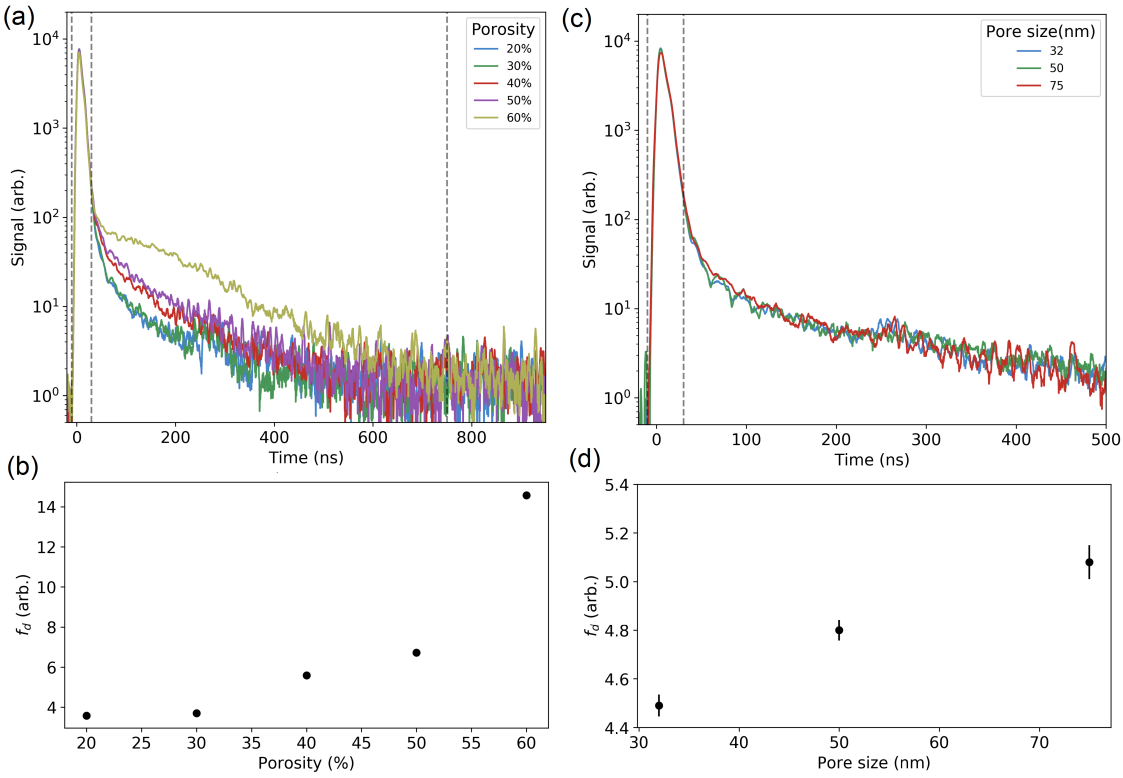

Figure 5.5: (a): Lifetime spectra of positrons implanted at 3 kV into various porosity samples with pores of a mean diameter = 32nm. (b): f_d with increasing porosity, the error bars are smaller than the points. (c) Lifetime spectra of 40% porosity samples with three pore sizes. (d) f_d with increasing pore size.

Long term confinement of Ps

For targets with large pores and low porosity we observe long term confinement of ground state Ps. This is due to Ps becoming confined within the voids that are isolated. Only the Ps atoms that are formed on the surface of these samples are able to interact with the lasers in vacuum. This is shown explicitly in figure 5.6 as there is a depletion of signal in the $1s$-$2p$ line scan as the target bias is increased. This is due to the surface formation fraction decreasing as the positrons are implanted deeper into the sample.

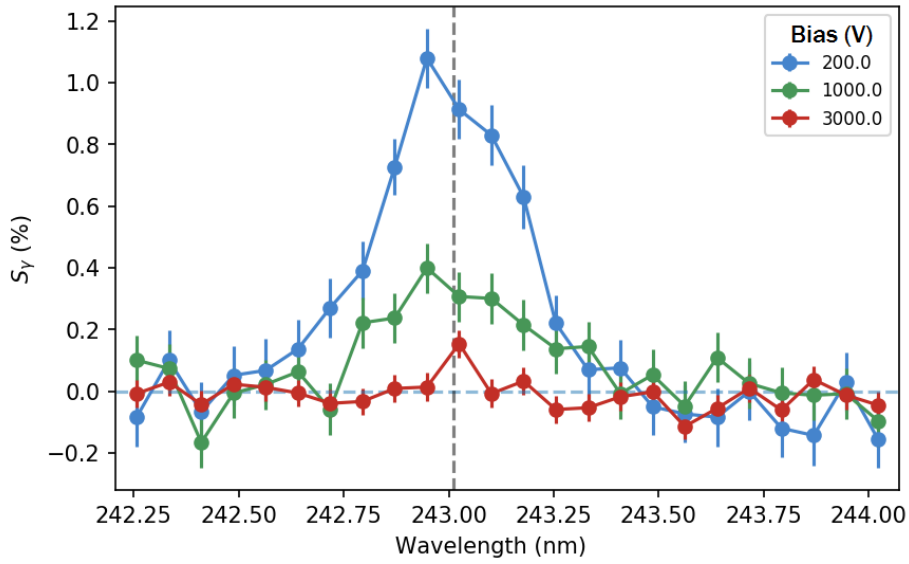

Figure 5.6: Depletion of the $1s$-$2p$-ionisation signal (S_γ) as the implantation energy is increased for a low porosity macroporous sample.

The excitation laser can be directed into the sample following the geometry show in figure 5.4. This allows interrogation of atoms that have been spatially confined. Pulses fixed at 243 nm irradiated the sample at a range of times after positron implantation.

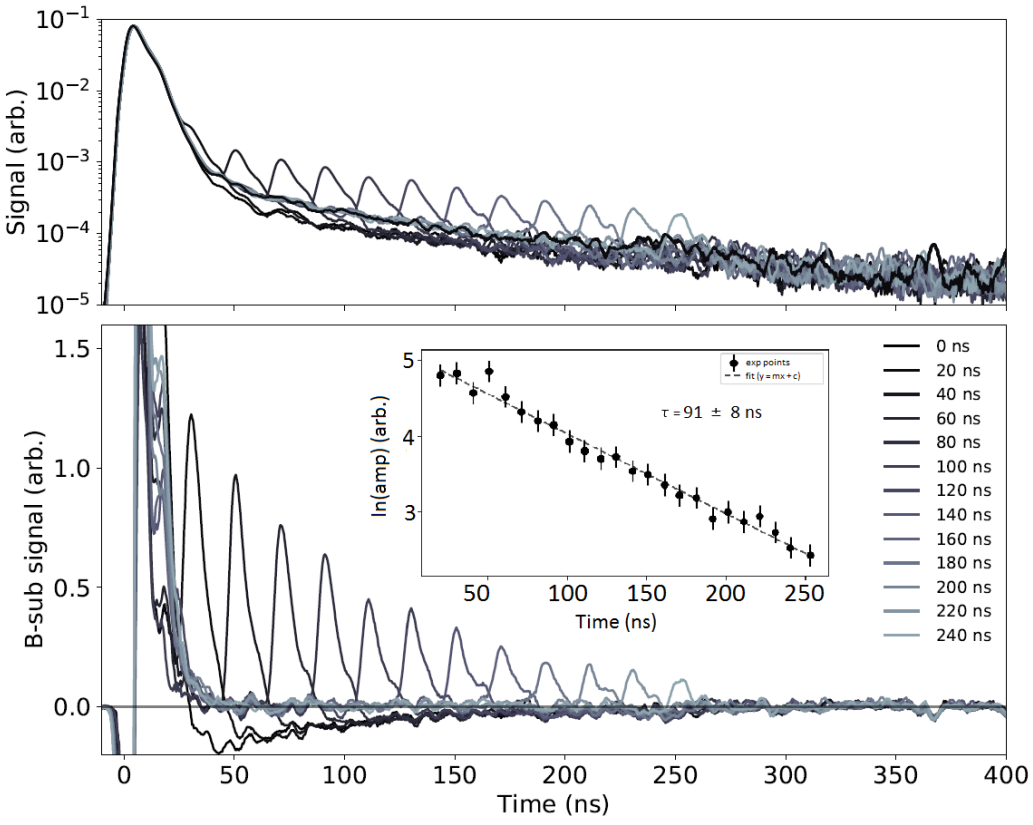

Figure 5.7: Above: Averaged SSPALS data with excess annihilation signals induced by the laser. Below: Background subtraction of the data in above. Inset: The linearised peak amplitudes plotted on the log scale to extract the confined Ps lifetime which is measured as 91 $\pm$ 8 ns.

Figure 5.7 shows excess annihilation signals as the laser arrival is delayed in steps of 10 ns relative to positron implantation. The mean amplitudes of the excess peaks in the background subtracted trace (lower figure) averaged over 300 shots were plotted on the $\log_e$ scale and fitted linearly and this is shown in the inserted figure. This was done to estimate the *o*-Ps lifetime within the sample. All of the points are shown in the insert whereas every other measurement is shown in the spectra and background subtracted spectra for clarity. The long term confinement of Ps is apparent due to excess annihilation signals at times which exceed the measured Ps emission time in SiO_2 ($\sim$ 10 ns) [Deller *et al.*, 2015b]. Ps is probed within the material at times which are long after positron implantation. Figure 5.7 was obtained using a sample with a mean pore diameter of 32 nm and a porosity of 40 %. The measured Ps lifetime within this sample is determined as 91 $\pm$ 8 ns.

The Tao-Eldrup model [Eldrup *et al.*, 1981; Tao, 1972] treats the cavity as an infinite potential well where the penetration of the *o*-Ps wave function into the wall boundaries give rise to the pick-off annihilation rate and hence lifetime within the cavity. However, this model is not reliable for void sizes above 1 nm which has led to recent modifications to the model by Wada and Hyodo [2013]. The models predict that the *o*-Ps lifetime within cavities larger than $\sim$ 30 nm should be close to, if not the same as the vacuum lifetime. It is therefore unexpected to measure a considerably shorter lifetime within a 32 nm cavity.

With the laser directed into the sample shortly after positron implantation, the 1*s*-2*p* transition wavelength was scanned to measure an excitation line shape of the confined atoms. The technique follows that which is explained in section 5.1.1 except a second laser for photoionisation of 2*p* states was not required with this sample. The optimum time of laser arrival was found via the largest excitation signal S_γ. This provided unexpected results which are shown in figure 5.8.

The 1*s*-2*p* transition line shape taken with the laser directed into the sample was expected to yield a Gaussian distribution centred about the mean excitation wavelength of 243 nm. A cavity induced shift resembling the data shown in figure 5.4 was not expected in large pores. Line narrowing effects [Dicke, 1953] may be

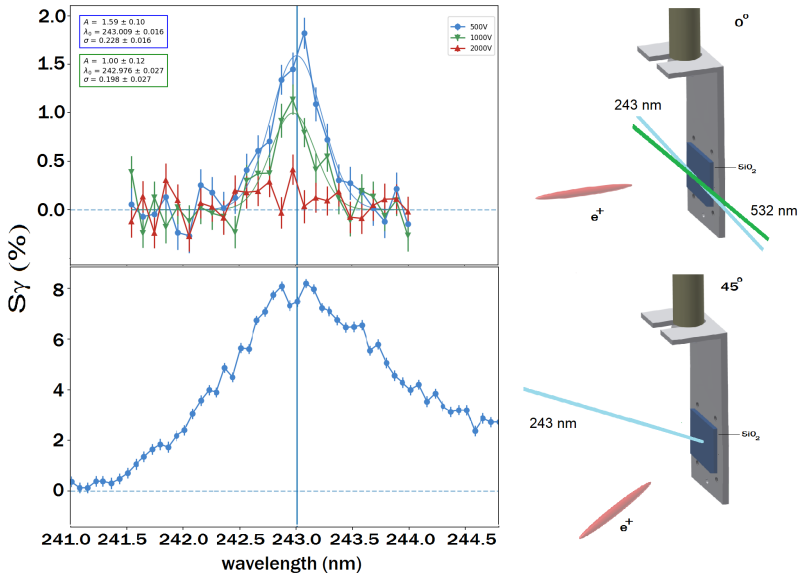

Figure 5.8: Above: Further examples of vacuum line scans of the $1s$-$2p$ transition is Ps formed and reflected from the surface of a macroporous silica sample. Below: $1s$-$2p$ line scan of Ps atoms confined within the sample.

resolved and it would perhaps be expected that the distribution of the Ps kinetic energies would be narrow in the case of uniform pores. However, a very broad range of wavelengths are able to excite Ps and the dependence on wavelength is unclear. This unusually broad and undefined line shape in addition to the lack of a photoionisation laser suggest that chemical quenching from an unknown origin may be taking place. The data suggest that $2p$ states may be having a stronger interaction due to the rapid annihilation of atoms addressed by the UV laser. Ground state atoms seem to survive in the environment for much longer as shown in figure 5.7. However, the shorter than expected lifetime of confined o-Ps may be explained by the sample properties.

The data shown in figure 5.7 represents the first Ps lifetime measurement using a laser as a time dependent probe of a Ps population. This technique has an advantage over positron annihilation lifetime spectroscopy (PALS) as sample specific processes can be identified such as the apparent chemical quenching observed here.

Transmission targets

Positronium converters that operate in reflection geometry have a disadvantage for experiments where the emitted Ps is to be transported away from the production region by external fields. The main challenge in using external fields is to avoid deflection of the incoming positron beam. This has been achieved with a reflection target using a pulsed electrostatic guide and this technique is explained further in chapter 4 section 4.2.1. However, several steps must be taken to achieve transportation which brings inevitable losses.

Transmission targets offer an alternative solution to this problem as the excitation and subsequent transport can be performed along, and in the direction of the positron beam axis. A production scheme where Ps is produced in transmission could enable experiments where Ps is imaged on axis, transported to a region of trapped antiprotons, or a scattering cell to name a few examples. However, collisional cooling within the bulk of the material as the Ps diffuses through it is essential for efficient laser excitation and subsequent Ps lifetime extension for such experiments. Previously, thin silver foils have been used to produce Ps in transmission [Poulsen *et al.*, 1991]. However, the foils must be heated for Ps production which presents practical challenges.

Measurements of Ps kinetic energy and formation efficiency were performed on thin mesostructured targets which operate in both a reflection and transmission geometry [Andersen *et al.*, 2015]. The materials were produced at the University of Aarhus, Denmark by the deposition of porous silica onto 20 nm thick amorphous carbon films via the technique of glancing angle deposition [Robbie *et al.*, 1995]. The structure of the material is rather different to the mesoporous materials described in the previous section. Here, the deposited film takes the form of a uniaxial anisotropic mesostructure with columns stranding orthogonal to the surface. The deposited material is around 1 μm thick. A scanning electron Micrograph (SEM) image obtained using a focused ion beam of Ga^+ for cutting a cross section slice is shown in figure 5.9.

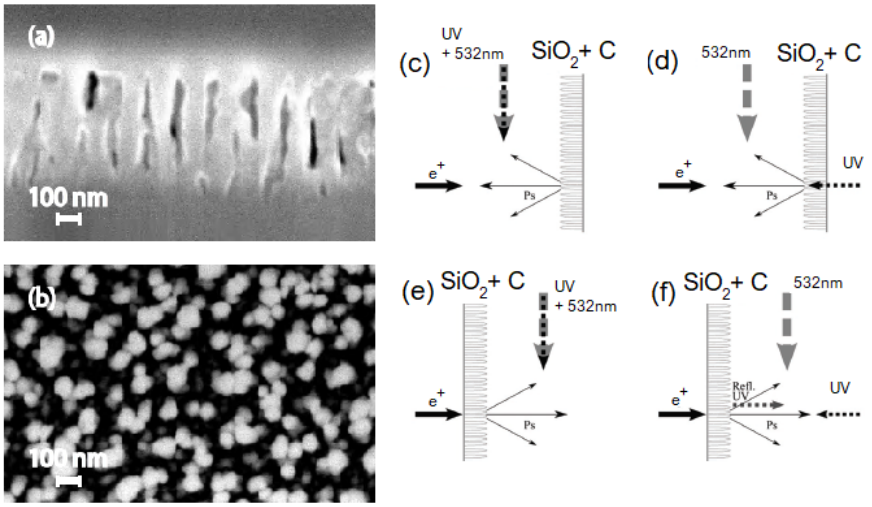

Figure 5.9: Meso-structured silica film imaged by SEM (a) in cross section and (b) from a top view. A carbon deposited layer can be seen in (a) and is used to protect the surface from the Ga^+ ion beam used to cut the cross section slice for transmission electron micrograph (TEM) imaging. TEM determines the film thickness as $\sim$ 800 nm. (c)-(f) The various orientations available with these targets which are explained in the text. Images were produced at the University of Aarhus, Denmark [Andersen *et al.*, 2015].

Figure 5.9 (c) and (d) show Ps formation in reflection geometry where both the transverse (c) and longitudinal (d) energy of the Ps can be measured by having the laser pass parallel, or penetrate through the thin carbon foil respectively. (d) and (f) show the same measurement technique for positrons that penetrate the foil and are excited following diffusion through the silica.

Ps formed within the bulk of the silica are able to diffuse through and undergo collisions with the walls of the columns. The column wall spacing is $\sim$ 100 nm which presents a larger, more open structure to the samples described in the previous section. It is therefore expected that a similar confinement limit on the cooling of Ps would not be imposed with these materials and it is the film thickness that sets the minimum achievable Ps energy. However, due to the column spacing being large, there is a limited number of collisions with the walls as Ps passes through the sample, resulting in fast Ps.

In reflection geometry, both the transverse and longitudinal kinetic energy were measured via Doppler spectroscopy of the $1s$-$2p$ line shape. Figure 5.10 shows results of the both the transverse and longitudinal measurements, where the excitation scheme followed the geometry of figure 5.9 (c) and (d) respectively. The data shows the kinetic energy of Ps. In the transverse measurement this is obtained from fitting $1s$-$2p$ line scans and extracting the RMS velocity (equation 4.1). The kinetic energy is then found via the classical expression $E_x = 1/2\ m_{ps}(v_{RMS})^2$, where x refers to the transverse direction. The longitudinal energy was estimated via the Doppler blue-shift, as the Ps traveled towards the laser.

In the reflection geometry, the targets show some Ps cooling as the implantation energy is increased. However, the highest implantation energy gives rise to emitted Ps with $\sim$ 200 meV of energy in both the transverse and longitudinal direction. The required implantation depth for Ps to loose all of its energy through collisions is longer than the sample thickness [Andersen *et al.*, 2015], this sets a minimum achievable energy that is higher than that of the mesoporous structures described in the previous section, where the lowest Ps kinetic energy achieved in this study was $\sim$ 60 meV, see section 5.1.1.

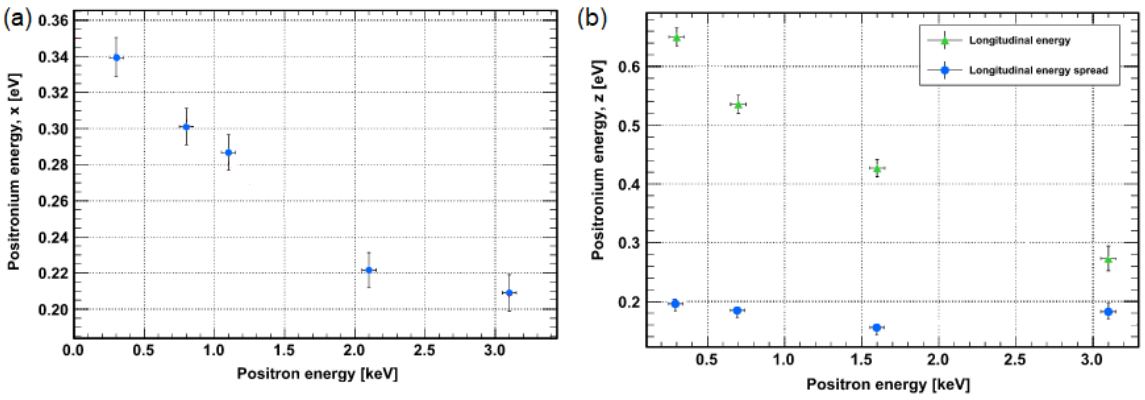

Figure 5.10: (a):The reflection-formed Ps transverse energy as extracted from the Doppler broadening widths, and plotted as a function of positron implantation energy. (b): The reflection-formed Ps longitudinal energy and energy width as extracted from the Doppler shifted resonances, and plotted as a function of positron implantation energy. [Andersen *et al.*, 2015].

In the transmission geometry (figure 5.9 (e) and (f)), positrons are implanted into the carbon foil where they either annihilate, form Ps in reflection, or fully penetrate through the foil where Ps formation and cooling within the silica is possible. At lower energies Ps formation on the surface of the foil is most likely and is was found that Ps exited on the opposite side at positron energies above 1 keV, which is shown in figure 5.11. f_d is maximised between 1.4 – 2 keV. The maximum formation fraction is obtained as the optimal trade off point between positrons making it through the carbon foil and positrons being implanted not too far into the silica columns.

In a similar fashion to the reflection geometry, the Ps kinetic energy was measured in transmission and the data is shown in figure 5.12. For the transverse measurement, the kinetic energy was extracted from a double peak resonance structure as a result of $\sim$ 90% of the UV light reflecting back from the target and initiating a second, red-shifted transition and is explained further in Andersen *et al.* [2015].

The data show some Ps cooling via collisions as Ps diffuses through the pillars. However, the Ps emitted from these samples is quite hot, $\sim$ 200 meV in both

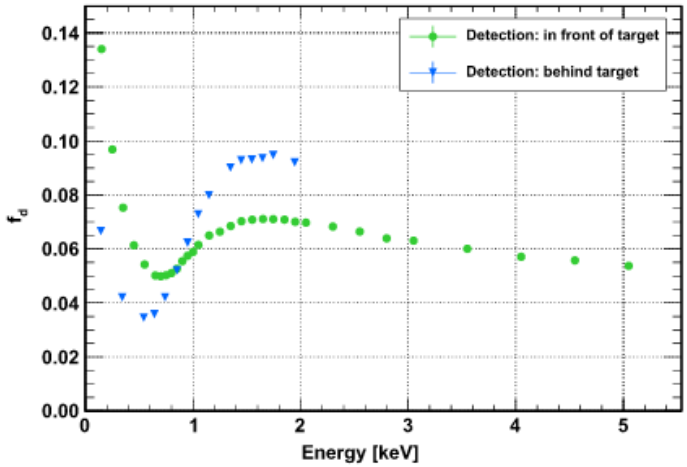

Figure 5.11: Ps formation efficiency in transmission geometry. The delayed fraction observed at low positron impact energy (0.8 keV) is attributed to Ps reflected from the carbon foil, whereas at higher energies the positrons can penetrate the carbon foil and form Ps in the meso-structured silica. Positioned in front of (behind) the target, the $PbWO_4$ and PMT more efficiently detect the annihilation of reflected (transmitted) Ps, as these are moving towards it. [Andersen *et al.*, 2015].

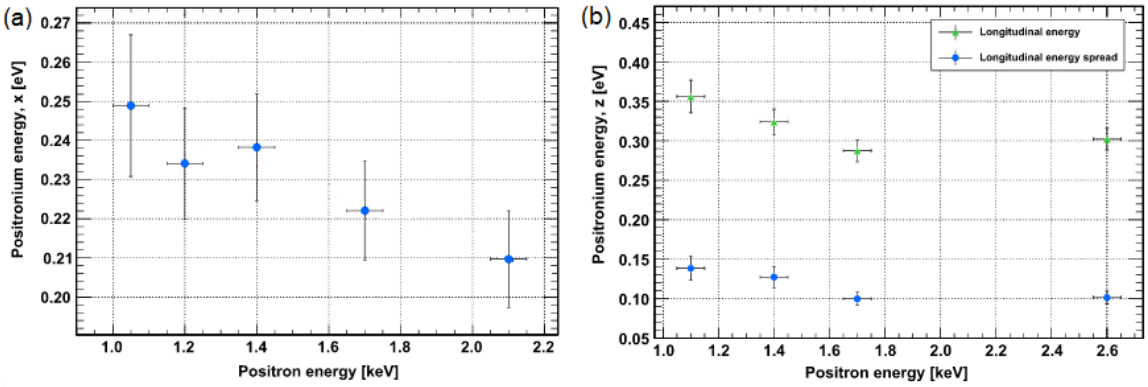

Figure 5.12: (a): The transmission-formed Ps transverse energy as extracted from the Doppler broadening widths, and plotted as a function of positron implantation energy. (b): The transmission-formed Ps longitudinal energy and energy width as extracted from Doppler shifted double peak resonance structures, and plotted as a function of positron implantation energy [Andersen *et al.*, 2015].

transmission and reflection geometries. The similarities between the minimum kinetic energies observed in both geometries support the idea that positrons are stopping deep into the silica structure near the foil, either through penetration through the foil in the transmission geometry, or through the deep implantation through the silica in the opposite direction. This enables the maximum diffusion length through the material providing the highest possible number of collisions. Improvements in this type of material for Ps cooling and emission could be realised with thinner foils as to decrease the required energy for penetration through to the transmission side. Also, narrower channels packed closer together would increase the overall Ps formation probability as Ps would be more likely to enter the open areas following formation in the bulk material. Narrower channels would also facilitate more collisional cooling which would be more forward directed upon emission into vacuum. This would be especially useful for an increased overlap with a laser and if the Ps is to be transported elsewhere following emission.

5.1.2 Magnesium oxide

Observations of Ps emitted from a layer of MgO were first made by Paulin and Ambrosino [1968]. Later Curry and Schawlow [1971] deposited MgO on the back side of a thin gold foil such that the Ps converter was operating in a transmission geometry. This followed the same geometry as the Au-MgO positron moderators introduced by Canter *et al.* [1974]. Deposition of MgO was achieved by burning a magnesium ribbon in air and collecting the oxide onto the foil directly. This produces an extremely porous layer of very fine MgO particles arranged as cubic crystals. Curry and Schawlow [1971] measured the kinetic energy of Ps emitted into vacuum from MgO via a coincidence counting scheme and the energy was determined as ~ 280 meV.

By burning a Mg ribbon in air and collecting the oxide onto an 10×10 mm copper sheet, a Ps converter target was made. The sample was held onto the mount in a reflection geometry and Ps formation was observed following positron bombardment of the MgO deposit. Increasing the target bias results in reductions in f_d

and this may be due to positrons penetrating deep into the MgO layer where they meet the Cu substrate and annihilate. An implantation curve is shown in figure 5.13.

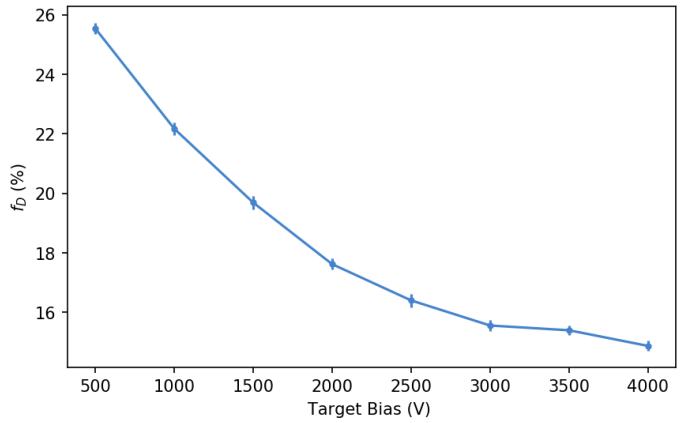

Figure 5.13: Implantation energy scan for MgO deposited on untreated Cu. The value of f_d decreases with energy. The apparent plateau may indicate that positrons are implanted deep enough to meet the Cu substrate where they are lost to annihilation.

However, deeper implantation within the range achievable (up to 5 keV) does not result in cooler Ps being emitted and this is shown via Doppler spectroscopy in figure 5.14. It is assumed that positrons require very deep implantation to lose energy through a reduced number of inelastic collisions much like that of other oxide grains [Mills *et al.*, 1989; Nagashima *et al.*, 1995; Tianbao *et al.*, 1987].

One would assume that the average void diameter in an MgO deposit is therefore quite large. Rao and Sunandana [2008] observed the formation of 15 - 60 nm MgO clusters via the technique of X-ray diffraction in a sample prepared with combustion. However, there are many types of MgO deposition techniques with varying results. A wide range of void sizes is expected for an MgO deposit which has not been annealed into a regular crystalline structure.

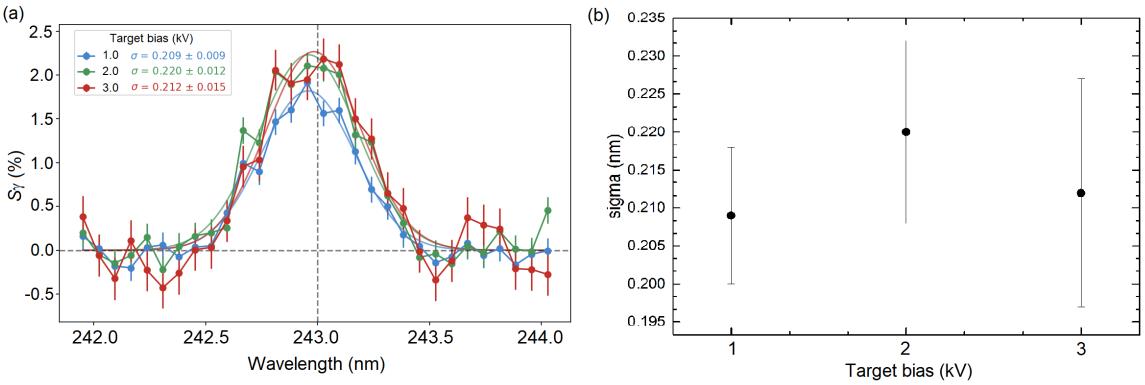

Figure 5.14: (a): 1*s*-2*p* line scans of Ps emitted from MgO at different implantation energies. The fitted widths are also shown. (b): No statistically significant change in the measured width indicating a lack of collisional cooling within the sample.

The data in figure 5.14 shows that no significant Ps cooling is taking place in this material over an increased diffusion length which suggests that the mean void size is large and Ps does not have a significant number of collisions within the material.

To ensure Ps is formed in the deeper layers of the sample, maximising the amount of possible collisions, a transmission target was made. This was achieved with an MgO deposition onto a thin SiN film which was 50 nm thick. An Mg ribbon was burnt in air and the oxide was collected onto the film in the same way as the target with the Cu substrate. However, with this sample positrons can be made to impinge on the SiN side such that Ps is formed at a location with a maximised MgO volume to diffuse through before entering vacuum. This sample is geometrically similar to the samples described in the previous section (see figure 5.9).

With the lasers passing perpendicular to the face of the MgO side of the sample, positrons were implanted into the SiN film at varying energies. The UV laser was tuned to excite the 1*s*-2*p* transition at 243 nm, and the IR laser was tuned to 730 nm in order to ionise atoms that had excited the MgO and been excited to the 2*p* state. The background measurement for determination of S_γ values was made with the laser arrival set to be 1 μs before the positron arrival.

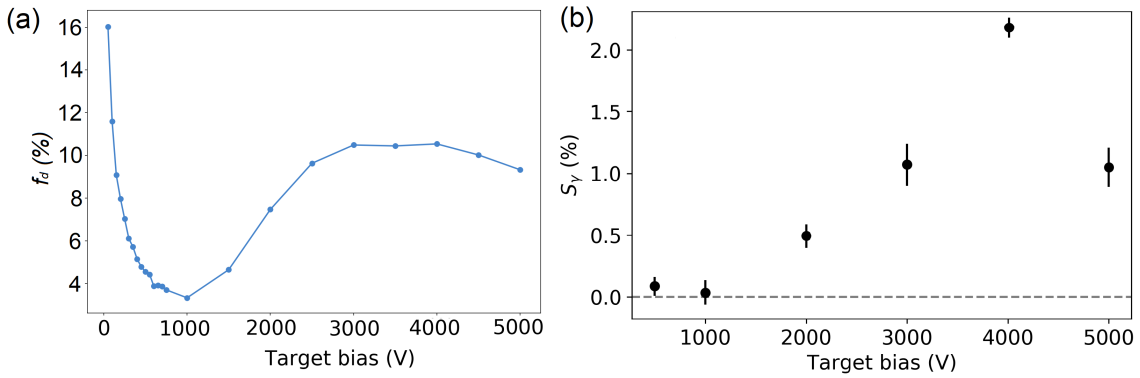

Figure 5.15: (a): Implantation energy scan for SiN-MgO target. Some Ps is reflected at low energies, and full penetration of the SiN film is achieved at energies above $\sim$ 1 kV. (b): The laser interaction signal S_γ measured following ejection of Ps atoms on the MgO side of the sample.

The data in 5.15(a) follows a similar form to that shown in figure 5.11 and shows that Ps can be made and reflected from the SiN surface at low energies. It appears that virtually no Ps (an $f_d \sim 4\%$ is typical of background levels) is made when positrons stop within the SiN layer and f_d is only recovered when positrons are transmitted through the thin film where Ps can be formed in the deeper layers of the MgO deposit.

The $1s$-$2p$ line shape was then measured in the transmission geometry. There was no change to the line shapes with varying bias above the level which permitted transmission (see figure 5.15) much in the same was as the reflection data shown in figure 5.14. Representative line shapes for both the reflection and transmission geometries are shown in figure 5.16. We therefore conclude that Ps does not undergo any significant collisional cooling following its diffusion through MgO. This is likely due to a large open volume.

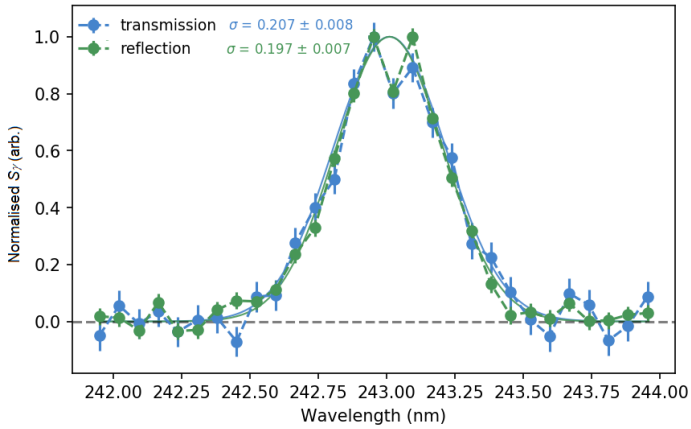

Figure 5.16: 1*s*-2*p* line scans for Ps formed in MgO in both a reflection and transmission geometry. The kinetic energy in both cases is ≈ 350 meV.

5.2 Single crystal semiconductors

Unlike the materials previously described, it is not possible for Ps to form within the bulk of metals or semiconductors. This is due to high electron densities which cause Ps to be unbound due to screening effects [Callaway, 1959]. Ps can only be formed on the surface. The positron can either pick up an electron following its reflection from the sample, which can result in a broad range of Ps kinetic energies, or form when a positron resides in a shallow surface potential well which is induced by its own image charge. Ps is then formed if an e^+ and e^- are emitted into vacuum together via a spontaneous, thermally activated process. The rate of this type of Ps emission is governed by the material specific activation energy, the surface sticking coefficient, and the temperature of the sample [Chu *et al.*, 1981]. The efficiency of this emission process therefore improves when the sample is heated above room temperature [Mills and Pfeiffer, 1979].

Semiconductors can also exhibit the production of Ps via an excitonlike surface state [Cassidy *et al.*, 2011b,d]. The surface states are similar to the surface exciton observed by Weinelt *et al.* [2004]. To produce Ps, an electron binds to a hole in

the surface band forming a surface exciton denoted as X, which can be activated thermally. If positrons are present, the electrons can instead form Positronium, in a state denoted PsX [Cassidy *et al.*, 2011c]. The Ps formation efficiency via this process therefore depends on the sample temperature. Alternatively, the electron X states can be populated optically. PsX can therefore be produced in a non thermal process referred to as photoemission [Cassidy *et al.*, 2011c]. This opens the possibilities for efficient Ps production at low temperatures, a prerequisite for many advanced experiments.

We have observed both the spontaneous thermal activation of PsX, and a PsX emission enhanced by the presence of photons on P-type, Ga doped Ge(100) single crystals. The manufacturer stated resistivity of the samples was 0.019 - 0.024 Ω. cm. n-type, Sb doped samples with higher resistivities of 0.01 - 0.1 Ω. cm were also used briefly and it was found that the p-type single crystals were more efficient in Ps production via photoemission, a result consistent with previous studies on Si [Cassidy *et al.*, 2011d].

5.2.1 Sample preparation

10 mm^2 single crystal Ge samples were used in this study. Ge sample preparation requires an acid (HCl, 32%) for etching. The Ge sample preparation methodology was based upon the procedure outlined by Cassidy *et al.* [2011b] and is as follows:

Dust is removed from the Ge single crystals with directed N_2 gas. The sample was then immersed in distilled water for around one minute in order to dissolve the native oxide layer. The sample was immediately transferred into 32 % HCl acid for 3.5 minutes for etching. Evidence of the removal of the oxide layer was found in a test sample which became hydrophobic following this procedure. The samples were then dried with N_2 gas and attached to the cold-head mount shown in figure 5.17. The samples were placed in vacuum within twenty minutes following removal from the acid.

The etching process is expected to terminate Ge dangling bonds with Cl. These bonds are detrimental to Ps production [Cassidy *et al.*, 2011d]. The cold-head used here had a high temperature (1000 K) interface which facilitated the removal of Cl via thermal desorption.

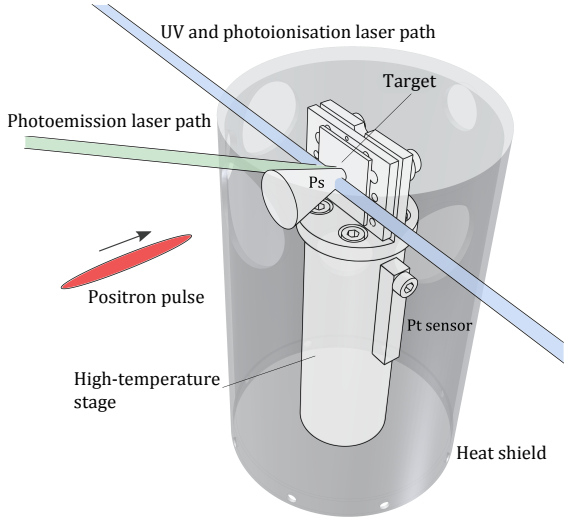

Figure 5.17: Schematic layout of the high-temperature cold head interface and positron beam and laser pathways. Holes are drilled in the heat shield to allow laser access from two directions. The heat shield is grounded via the chamber, and the target mount is biased to control the incident positron beam energy [Cooper *et al.*, 2016].

Electrical isolation from, but thermal contact with the target mount and the variable-temperature interface was achieved using sapphire discs. This enabled the positron impact energy with the target to be controlled via the sample bias. For the high temperature interface the real range of sample temperatures was ~ 20-750 K. All quoted temperatures and those shown within the figures are as measured using a Pt sensor attached to the high-temperature stage beneath the target mount (see figure 5.17). K-type thermocouples were also used to measure the temperature with the sample at ground potential. Early heating tests showed a discrepancy between the thermocouple readings and those of the thermocouples. A maximum temperature of 780 K was recorded at the target when the Pt sensor

read 850 K. This indicated a thermal gradient between the two positions. All temperature sensors agreed to within 5 K within the range of 27-700 K. All quoted temperatures above this range therefore have a considerable uncertainty attached to them. The minimum temperature attainable for this cold-head was $\sim$ 15 K. However, this was raised to around $\sim$ 20 K by the laser access holes in the heat shield, which is also the lower limit of the Pt sensor range.

Following insertion into vacuum the treated semiconductor target was moved into the path of the pulsed positron beam and the resulting delayed fraction f_d was recorded. Initially the formation efficiency is low and this is due to the presence of Cl terminated dangling bonds. These are removed thermally as evidenced by an increase in f_d and is shown in figure 5.18. The temperature was recorded using a digital temperature controller connected to the k-type thermocouples and platinum censor. Data was transferred via Ethernet cable to a server dedicated to the recording of environmental variables and was matched to the f_d data with time stamps made at the start of each 30s acquisition. The figure shows that an increase in f_d is observed as the temperature is raised above $\sim$ 700 K. Heating further resulted in a higher Ps yield until a plateau was reached at 850 K. The temperature reading in this high range is unreliable and the actual maximum temperature was closer to $\sim$ 750 K. A higher Ps yield remains as the sample returns back to room temperature showing that the increase is a result of thermal desorption of Cl. Thermal emission of PsX is relatively efficient at room temperature following sample etching and thermal treatment as $f_d \approx 0.27$.

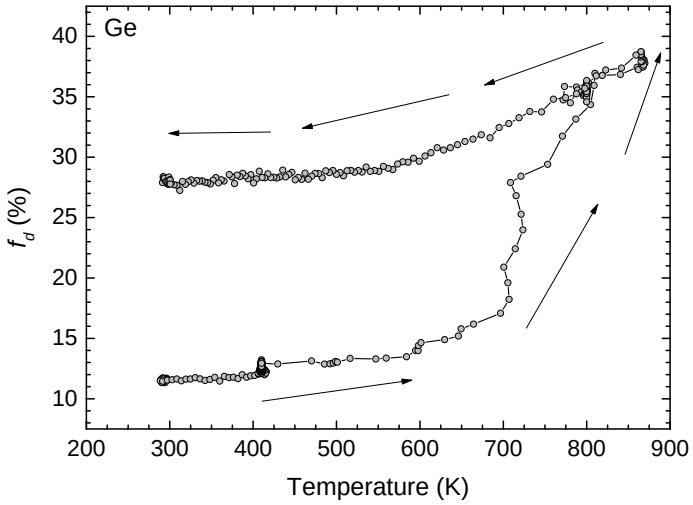

Figure 5.18: Thermal desorption of Cl and the resulting increase in f_d, measured from p-type single crystal Ge. The measured temperatures above 700 K are inaccurate, as explained in the text. Each point represents the average f_d value over a 30 second period [Cooper *et al.*, 2016].

5.2.2 Laser enhanced positronium production on semiconductors

PsX emission can be greatly enhanced when the surface electron states are populated optically via a process referred to as photoemission of PsX. The photoemission process was observed with 532 nm (visible, green) laser pulses (see chapter 4) directed into samples that had been prepared and heated as outlined in the previous section. The laser power was limited to avoid destruction of the samples. The maximum fluence used for these tests was 50 mJ cm^{-2}. The significant increase in the PsX formation efficiency with photoemision is shown in figure 5.19. The PsX formation enhancement is most effective when the laser arrives at around the same time as the positron pulse. The effect is still significant when the laser arrives up to $\sim$ 5 ns before the positrons indicating the lifetime of the surface states that participate in PsX formation. Previously with Si targets, the surface states appeared to have longer lifetimes than those seen here with Ge. The electron surface states

persisted for many tens of nanoseconds with p-Si(100) [Cassidy *et al.*, 2011c].

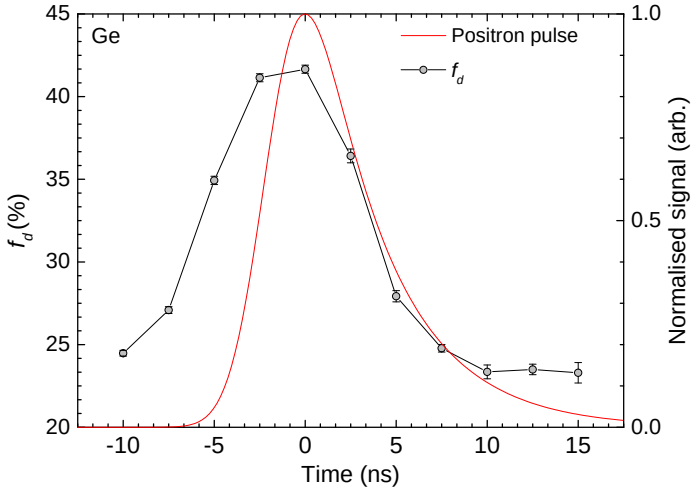

Figure 5.19: Time dependence of PsX photoemission from a p-type Ge(100) crystal. The laser fluence was ~ 50 mJ/cm^2. The solid (red) line is the positron annihilation signal measured with a fast γ-ray detector. This signal is the convolved signals of the prompt annihilation radiation and the ~ 4 ns (FWHM) detector response [Cooper *et al.*, 2016].

PsX formation via photoemission from single crystal Ge(100) semiconductors offers a copious amount of Ps atoms. However, as shown in the next chapter, the kinetic energy of the Ps emitted is relatively high (~ 170 meV), which can present some issues for further experimentation.

Chapter 6

Formation of positronium at cryogenic temperatures

There are some situations in which it may be necessary to produce an efficient source of Ps in cryogenic environments. For example, an experiment in which the effects of black-body radiation are to be minimised. Other examples include Ps mediated antihydrogen production at low temperatures or the utilisation of mesoporous structures that have been modified to produce cold Ps atoms [Liszkay *et al.*, 2012]. For antihydrogen production, it is envisaged that the charge exchange interaction (see section 4.2.2), would be conducted within the cold bore of a superconducting magnet [Doser and the Aegis collaboration, 2010]. For gravitational free-fall measurements and precision spectroscopy, long lived Rydberg states are required which are susceptible to transitions towards the short-lived ground state following interactions with black-body photons. These transitions can occur at room temperature for $n > 20$ [Gallagher, 1994].

If the Ps is to be optically excited, then laser irradiation of Ps convertor materials at cryogenic temperatures may be unavoidable. In this case a robust material that is immune to problems arising from laser irradiation would be required. As explained in chapter 5 mesoporous SiO_2 and single crystal semiconductors can produce Ps via non thermal processes and can therefore be expected to function at any

temperature. How these materials function when cooled to cryogenic temperatures and when irradiated with laser light is explored in this chapter. This work has been published by Cooper *et al.* [2016].

Porous structured materials (chapter 5) which produce Ps at low temperatures could be useful in the first observations of a Ps Bose-Einstein condensate (BEC) [Liang and Dermer, 1988; Platzman and Mills, 1994]. The realisation of Ps BEC could then lead to many other observations such stimulated annihilation, and eventually a γ-ray laser [Avetissian *et al.*, 2014; Bertolotti and Sibilia, 1979; Mills, 2014; Ramaty and Jones, F.C. and McKinley, J.M.; Wang *et al.*, 2014]. The critical temperature of a BEC transition is given by

$$T_c \approx 3.3125 \frac{\hbar^2 n^{2/3}}{m k_b} \tag{6.1}$$

where n is the Boson density. T_c is inversely proportional to the mass per Boson. As Ps is of a very low mass, its effect on the critical temperature of a BEC transition is quite small. In order to make a Ps BEC, a dense congregation of spin-polarised Ps atoms must be cooled to below the BEC transition temperature for that given density [Cassidy *et al.*, 2010b]. The highest density of Ps observed previously is of the order 10^{16} Ps cm^{-3} [Cassidy *et al.*, 2012a]. With an increase in this density by two orders of magnitude, the BEC transition temperature would be at the easily attainable temperature of ~ 15 K. The BEC transition temperature could be raised further if Ps cooling rates are able to be increased within engineered structures that facilitate a combination of both collisional, and laser cooling where a collection of Ps atoms settle within a central void [He *et al.*, 2012; Morandi *et al.*, 2014]. A combination of both collisional and laser cooling techniques may be required to reach the lowest temperature allowed by the cavity [Mills, 2010]. For example, if Ps could be laser cooled to the recoil limit (≈ 1 K, which is higher than the ≈ 1 mK Doppler limit due to the low mass of Ps) then a BEC transition would occur at a density closer to what has already been observed.

It is therefore important to develop an understanding of what happens to Ps converter materials over a range of temperatures and when irradiated with lasers.

6.1 Cooling samples to cryogenic temperatures

Positronium converter materials were mounted on closed-cycle helium refrigerators which operate according to the Gifford-McMahon principle [McMahon and Gifford, 1960]. Two were used over the course of this study. One of them had a 1000 K high-temperature interface, as shown in figure 5.17.

The second cold head was similar except it did not have a high temperature interface and there are some minor differences in the heat shield geometry. The principle of cryogenic pumping is that gasses such as water vapour, oils and others are frozen onto a cold body which in turn reduces the pressure in the open area of the vacuum chamber. Gas molecules are held onto the cold surface via Van der Waals forces.

As Ps thermalisation within a porous structure relies on many hundreds of thousand collisions with the internal walls [Ford *et al.*, 1976; Gidley *et al.*, 1999], the lifetime of Ps within these structures is heavily dependent of the surface conditions of the samples. This is even more critical for materials where the Ps formation is exclusively on the sample surface. Cooling positronium converters makes them susceptible to the absorption of background gasses.

Using the beam line arrangement showed in figure 2.8, a cold head with a range 12 - 300 K was installed in the target chamber and the delayed fraction (f_d) was recorded as a mesoporous SiO_2 sample was cooled. The region in which the target resided had poor vacuum isolation from the buffer gas trap. The pressure here, as measured by an ion gauge near the cold head was $\sim 2 \times 10^{-6}$ mbar during normal trap operation. Under these conditions, the amount of Ps detected was inhibited rapidly after cooling to low temperatures and is shown in figure 6.1. The trap was run at 1 Hz and each data point represents the average of 20 shots. The temperature curve represents an interpolation between readings taken at 3 second

intervals following the same method described in section 5.2.2. All data is mapped together offline using the time stamp associated with the initial data points.

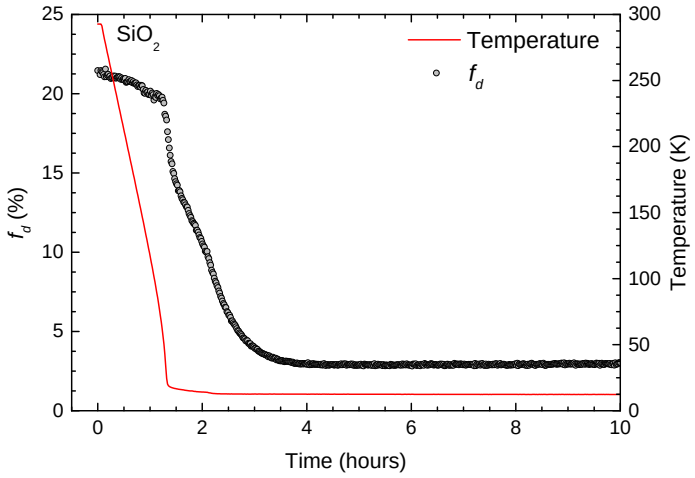

Figure 6.1: Delayed fraction (f_d) from cooled mesoporous SiO_2 measured near the trap (2×10^{-6} mBar). The delayed fraction error bars ($\pm$ 0.1 %) are not shown. A rapid reduction in Ps formation is observed as the target absorbs background gasses. [Cooper *et al.*, 2016]

The reduction in f_d is attributed to a high freezing rate of N_2 and CF_4 gas from the positron trap which renders the sample useless within a matter of hours. In some cases absorbed materials can in fact increase the cooling rate [He *et al.*, 2007], but more often it leads to a reduction in the amount of Ps emitted into vacuum [Mariazzi *et al.*, 2008; Moia *et al.*, 2012] due to the reduced lifetime within the material and chemical quenching. The available free volume in the sample is reduced affecting Ps lifetimes and the emission efficiency. As the pore volume is reduced, the rate of Ps-wall interactions increases. It is assumed that the amount of Ps produced is not affected as this happens within the bulk of the sample. It is therefore important to note that when speaking of the Ps formation efficiency, one is referring to the amount of Ps that has a lifetime that is long enough for either the diffusion and ejection into vacuum or the interaction with laser radiation, or in some cases both. Short lived Ps, either *p*-Ps or *o*-Ps with a reduced lifetime due to increased collisions or other quenching processes are not counted within the f_d

values if they annihilate within the early time window (see chapter 3).

6.1.1 Reduced pressure target chamber

To improve the vacuum conditions and reduce the rate of gas absorption in cold samples the beam-line shown in figure 2.8 was extended to accommodate differential pumping. Figure 6.2 shows the 2.5 m extension and the average pressure in three regions during normal trap operation. The buncher described in chapter 2 is also shown. The large eight port chamber has a cryogenic pump underneath, and the sample cold-head was installed from above, the base pressure in this region approaches the lower limit of the ion gauge which is attached to one of the eight ports. The mean recorded pressure is is $\sim 3 \times 10^{-9}$ mbar. The additional ports allow an easy laser access at 45^o, but due to the increased size of the chamber, the acceptance of the γ-ray detectors was reduced which affects the signal to noise ratio.

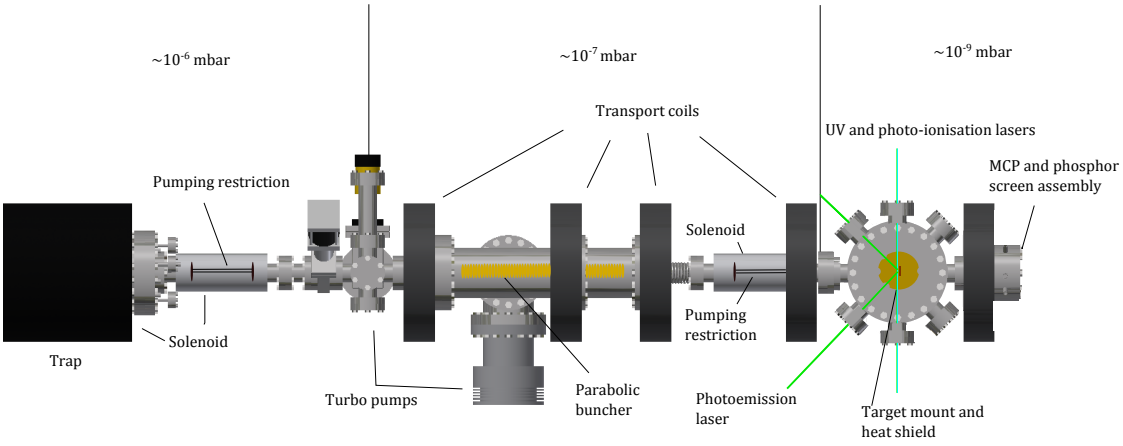

Figure 6.2: Extended beamline following the trap. Tube inserts similar to those described in chapter 2 are used with two turbo molecular pumps to achieve differential pumping and a reduced background pressure in the target region. The UV laser was directed both parallel and into the target depending on whether vacuum or confined Ps was being probed respectively.

Since the underlying production mechanism that occurs in mesoporous Ps converters is non thermal, they can be expected to work with similar efficiency at any temperature provided that the sample is not contaminated by background gas.

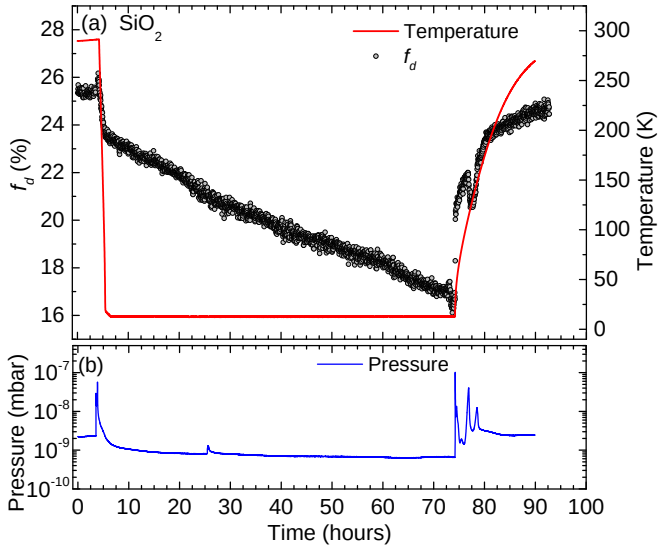

Figure 6.3: (a) Delayed fraction (f_d) from cooled SiO_2 measured in the low-pressure (10^{-9} mBar) chamber. (b) Pressure in the target chamber associated with the cooling and heating cycle of (a). [Cooper *et al.*, 2016]

In the new location f_d does decrease with time, but at a much reduced rate. The system was left monitoring f_d for just over three days and it dropped by almost 10% per day after an initial drop of ∼15 %. This reduction in f_d is also attributed to the adsorption of residual gas in the system, mostly N_2, CF_4 and, some H_2O. Whilst the gas is having a detrimental effect to the target, a sufficient source of usable Ps remains for several days which is enough time to perform many experiments. The room temperature f_d can also be recovered without venting to atmospheric pressure as the gasses can be desorbed thermally. The recovery and subsequent structure observed in the warm up curve is attributed to the desorption of gases at different temperatures, as evidenced by the fluctuations in the chamber pressure.

A short investigation into whether the 523 nm laser could remove absorbed matter via an ablation process was undertaken and some evidence for this was

found. However, to see a significant cleaning effect via heat transfer and desorption induced by the laser, the 532 nm fluence had to exceed 50 mJ cm^{-1}. Visible burn patterns on the samples were previously observed at fluences slightly above this. It was therefore postulated that the sample morphology would be irreversibly altered with this process and that regular resistive heating was a much less damaging option.

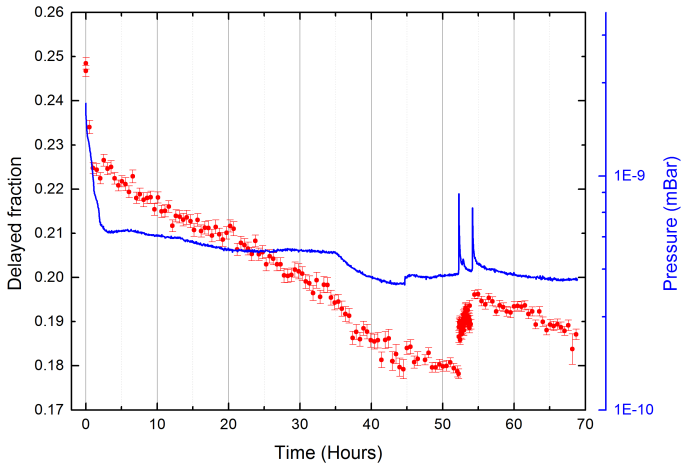

Figure 6.4: Irradiation of a cold, contaminated sample with 532 nm pulses of fluence = 50 mJ cm^{-1}. An ablation based cleaning is observed as evidenced by the increase in f_d and the spikes in pressure characteristic of desorbed material.

Figure 6.4 shows the cleaning effect via irradiation of the target with 532 nm pulses and the resulting increase in f_d and pressure at the time of laser arrival.

It was confirmed that gas adsorption was the primary mechanism for the reduction in f_d as the target was cooled down and left cold for a long time with the gas flow to the trap cut off. Regardless of how long the sample is cold for, the target starts at the same f_d when the trap is finally turned on suggesting that the sample does not undergo significant thermal contraction.

Positron beam impact has itself shown a detrimental effect to Ps converter materials at low temperatures previously [Cassidy and Mills, 2007d; Dauwe *et al.*, 1996; Djourelov *et al.*, 2005; Saito *et al.*, 1995]. This was not observed with mesoporous SiO_2 as the rate of f_d decline did not seem to depend on the rate of positron bom-

bardment. Figure 6.5 shows both of these tests which confirm that the reduction in f_d is mostly, if not entirely due to gas adsorption.

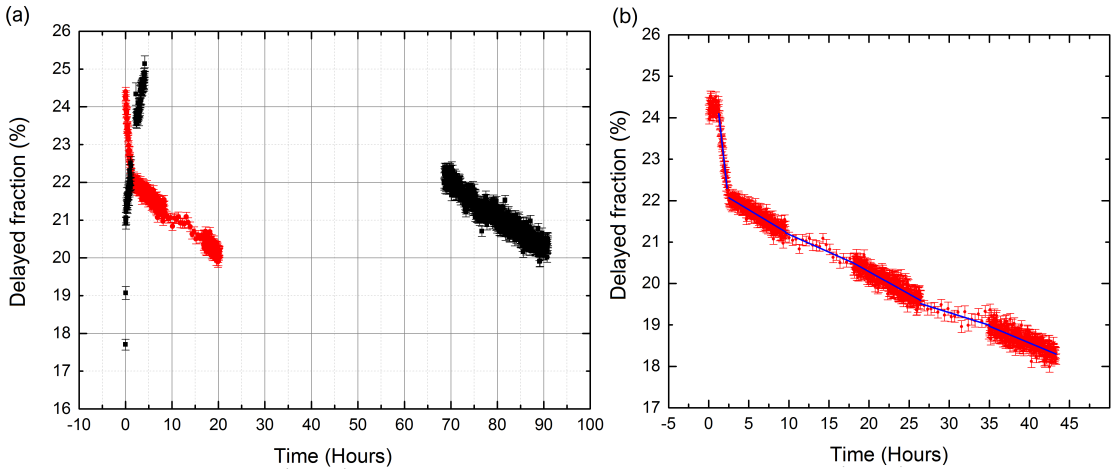

Figure 6.5: (a) Delayed fraction (f_d) from cooled SiO_2 measured as the sample is cooled(red circles), and after a delayed opening of the trap (black squares). The early black points show a thermal resetting of the sample before trap gas removal and cooling. (b) Variation of positron beam frequency as f_d is monitored for a cold sample. The gradient of the fitted lines does not change in a statistically significant way indicating that positron bombardment is not detrimental to the sample at low temperature.

Further confirmation of the non thermal nature of Ps production and emission by these samples was also observed via Doppler spectroscopy. In previous measurements of Ps emitted from SiO_2 it has been observed that the Ps kinetic energy does not depend strongly on the temperature of the sample in the range 50 - 300 K [Crivelli *et al.*, 2010].

Figure 6.6 shows that we have also observed no change in the Ps kinetic energy between 300 and 12 K via measurements of the Doppler broadened $1s$-$2p$ lineshape.

Gaussian fitting of the Doppler broadened lines yield σ of 0.070 $\pm$ 0.001 nm and 0.069 $\pm$ 0.002 nm for sample temperatures of 300 and 12 K. This corresponds to Ps kinetic energies of around 40 meV along the direction of the laser path, which

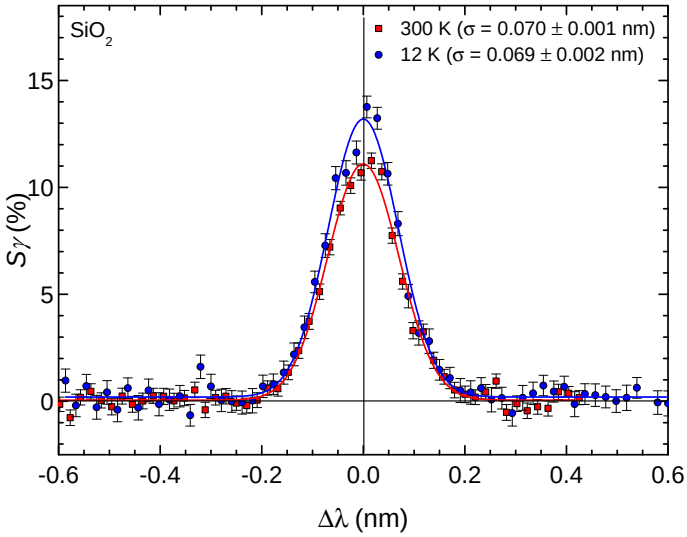

Figure 6.6: Doppler broadened $1s$-$2p$ line-shape measurements at 300 and 12 K. The central wavelength ($\Delta\lambda = 0$) is 243.01 nm. The data are fitted to Gaussian functions as described in chapter 4. The values of the Gaussian width (σ) are shown in the legend. [Cooper *et al.*, 2016]

is parallel to the SiO_2 sample surface.

6.1.2 Laser induced paramagnetic centres

It would seem unlikely that the cavity induced shift of the $1p$-$2p$ transition in Ps would be affected by temperature as the Ps kinetic energy is not. However, thermal contraction effects may be observed. A very different situation arose when the excitation and ionisation lasers were directed into the target following the geometry outlined in figure 6.2. A repeat of the cavity experiments outlined in chapter 5 was repeated at 12 K with a mesoporous sample. Observations of a cavity induced shift was unobtainable due to the effect of the laser on the sample. Within a very short space of time following irradiation of the target, the value of f_d had reduced significantly.

During collisions with the walls of the porous network the annihilation rate is approximately the spin averaged decay rate weighted by the 3:1 triplet-singlet ratio

[Gidley *et al.*, 1999] ($\sim 2\ \mathrm{ns}^{-1}$). The quantum mechanical version of this model states that the spin-averaged decay rate is applied only to the portion of the wave function that is deemed to interact with the wall which is determined empirically. The contribution to the decay rate from Ps-wall interactions can be small in any case, so that the total decay rate may be comparable to the vacuum rate if the pores are large enough. However, the Ps decay rate will be increased dramatically if there are sites within the insulator with unpaired spins [Deutsch, 1951; Ferrell, 1958]. These sites are known as paramagnetic centres and they can take many forms and can be difficult to define and identify without employing advanced techniques such as electron paramagnetic resonance (EPR). A combination of Ps lifetime and EPR measurements is desirable and this has been done in previous experiments involving bulk oxide grains [Saito and Hyodo, 1999]. However, these techniques have not been used together with thin films and could lead to insights into laser induced surface reactions and identification of the exact types of paramagnetic centres produced in these materials. With this knowledge it may be possible to engineer new Ps converters that are less susceptible to laser induced issues at low temperatures.

The presence of an unpaired spin allows *o*-Ps to undergo a spin exchange quenching process, namely the conversion to the short lived *p*-Ps state. Just like the gas adsorption problems described in the last section, it is thought that the laser does not effect the amount of Ps produced, it merely effects the mean lifetime of Ps whilst inside the porous network.

Some types of paramagnetic centres have been defined in various materials and their effects on Ps have been studied [Dauwe and Mbungu-Tsumbu, 1992; Lazzarini and Lazzarini, 2001; Saito *et al.*, 1995; Saito and Hyodo, 1999; Zhang *et al.*, 2010]. In general the majority of paramagnetic centres are unstable at room temperature. They may be formed, but thermal fluctuations at room temperature or above cause the rapid recombination of unpaired spins which suppresses spin exchange quenching. At low temperatures it is the recombination which is suppressed leading to long term stability of the paramagnetic centres and enhanced Ps quenching.

Saito *et al.* [1995] and Saito and Hyodo [1999] showed that paramagnetic centres produced at low temperatures by a UV lamp had a detrimental affect on the lifetime of Ps atoms produced in silica aerogel and fine oxide grains. The UV laser was responsible for the production of paramagnetic centres in our case following irradiation of mesoporous SiO_2 with laser light.

Positron irradiation is itself able to generate paramagnetic centers in some materials [Cassidy and Mills, 2007d; Dauwe *et al.*, 1996; Djourelov *et al.*, 2005; Saito *et al.*, 1995], but this was not observed here with mesoporous SiO_2 as shown in 6.5 (b). Figure 6.7 shows that irradiation with UV photons at low temperature is far more efficient in paramagnetic centre production as evidenced by the reduction in f_d. The apparent lack of this type of radiation induced damage may be due to a slight variation in the sample morphology and considerably less positrons to that used by Cassidy and Mills [2007d].

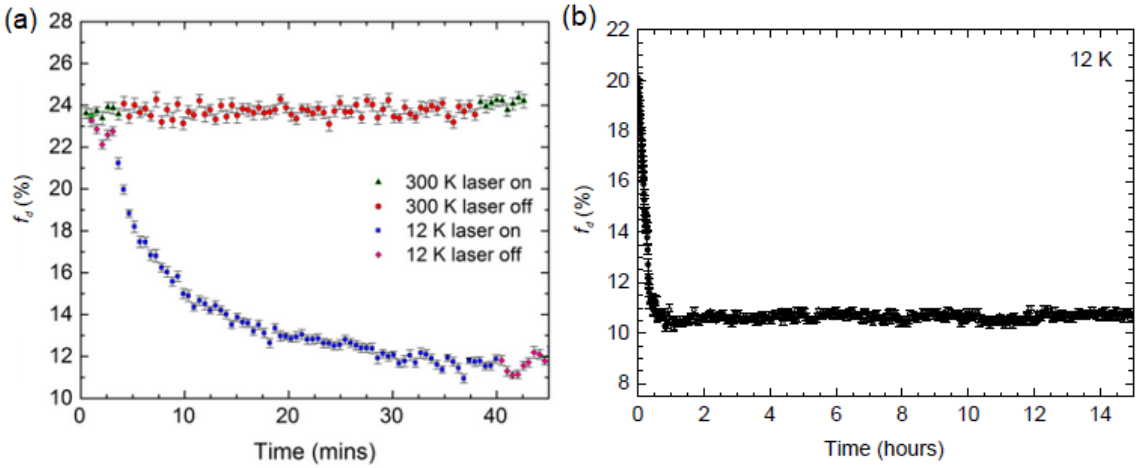

Figure 6.7: (a):Ps formation at 300 and 12 K with and without UV laser irradiation.(b): Long term stability of laser induced paramagnetic centres at 12 K. [Cooper *et al.*, 2016].

Figure 6.7 (a) shows a significant reduction in f_d during the irradiation of an SiO_2 sample cooled to 12 K with 10 Hz UV laser pulses. At 300 K there is no observable effect from the laser which is why the cavity induced shift of the $1s$-$2p$ line-shape is observable at this temperature.

Long term stability of these *o*-Ps quenching paramagnetic centres was observed as no recovery of f_d was found post irradiation at 12 K. We conclude that the laser induced paramagnetic centers observed here have extremely long recombination times as there was virtually no recovery of f_d when the sample was left at 12 K overnight. Figure 6.7(b) shows the rapid decline of f_d during the first $\sim$ 30 mins (laser on), followed by a low and stable f_d value for the hours that followed.

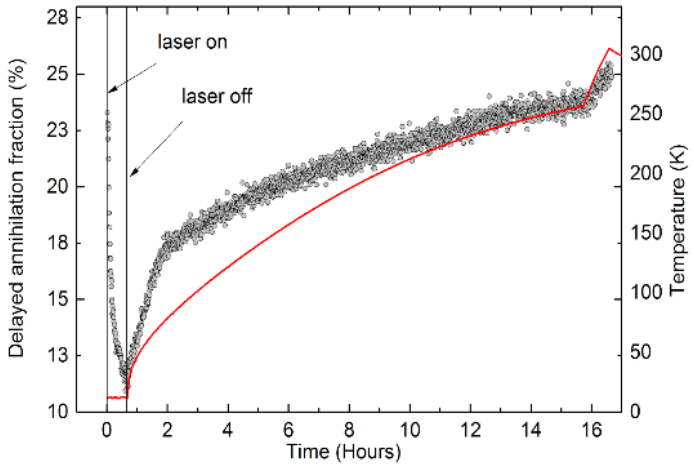

Figure 6.8: f_d as a function of temperature for an SiO_2 sample irradiated with UV light pulses at 10 Hz. The period of active laser irradiation is indicated by the vertical bars [Cooper *et al.*, 2016].

It was not until the temperature was raised that an increase in f_d could be observed. f_d could be completely recovered to its pre-cooling and pre-laser value by warming the sample back to room temperature which is consistent with thermally induced recombination of unpaired spins. Figure 6.8 shows the temperature dependent recovery of f_d. There appears to be a change in gradient of the recovery curve at around 75 K which could indicate that two distinct groups of paramagnetic centre are present.

If a single type of paramagnetic center which has a well-defined activation energy were present then we might expect to see threshold like behaviour in the recovery, i.e. a mass recombination of unpaired spins leading to a rapid recovery of f_d. However, the data suggests that it is more likely that there are many different

local environments, or types of paramagnetic center present, perhaps all falling into one of two subgroups and that the activation energies for thermal recombination are spread out across a broad range.

In the experiments of Saito and Hyodo [1999], radiation induced effects on Ps lifetimes were not observed in silica powder or silica aerogel that had been heat treated to 1073 K. This was attributed to the formation of -OCH_2 radicals, which were identified via electron spin resonance measurements and perhaps a similar heating process could also eliminate the production of paramagnetic centres in the mesoporous SiO_2 samples used here.

Warming these samples to temperatures in excess of 600 K would likely risk the sample integrity and our high temperature interface does not cover the same range of temperatures used by Saito and Hyodo [1999]. It was therefore not possible to check if warming the the targets to similar temperatures would reduce or prevent the radiation-induced effects. However, some heating was done and an increase in f_d was observed in samples heated up to 600 K. Figure 6.9 shows the improvement remaining as the sample returned back to room temperature much like that observed in Ge(100) single crystals (see chapter 5 figure 5.18). The desorbed material in this case being mostly H_2O from sample exposure to air during preparation and background gasses within the vacuum system.

Similar benefits were observed with SiO_2 samples heated to $\sim 400^oC$ in a tube furnace just prior to insertion into the vacuum chamber. However, this method leaves the sample susceptible to the re absorption of H_2O and other gasses. These risks are removed when heating in situ. The heated sample returns to room temperature with only a slight reduction in f_d from the maximum (600 K) value. This rules out an effect due to thermal desorption of Ps from surface states, which have been observed previously in both quartz targets [Sferlazzo *et al.*, 1987] and in silica films [Cassidy and Mills, 2008].

When the heated sample was cooled to 27 K and irradiated again, a reduction in f_d was reproduced, as shown in figure 6.10(a). However, f_d did not saturate at the same level as the first irradiation, which was done prior to heating, but this is

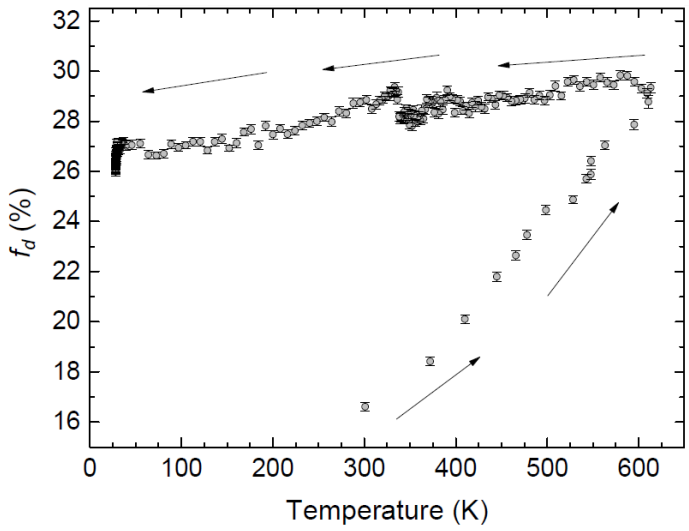

Figure 6.9: (a) Delayed fraction (f_d) (filled circles) measured as a function of temperature for an SiO_2 sample as it is heated. Each point represents the average f_d value over a 30 second period.

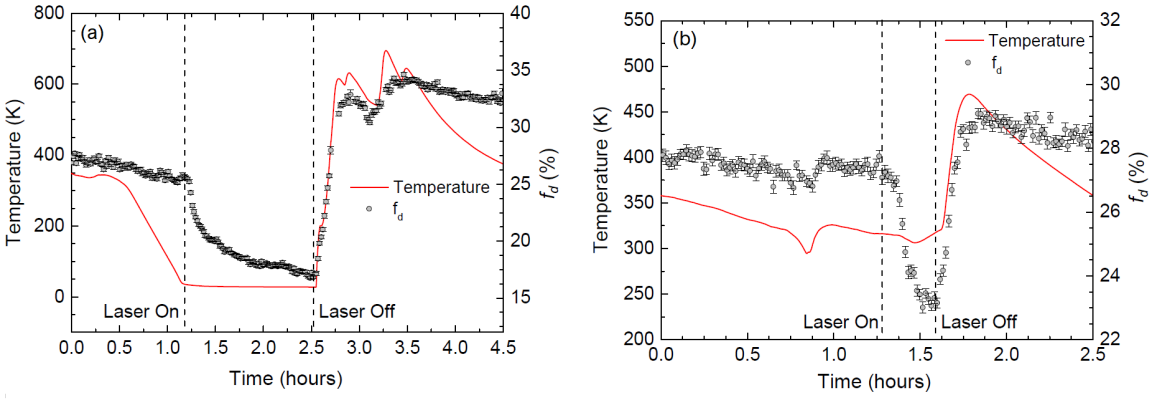

Figure 6.10: (a) Effect of cooling and laser irradiation on the delayed fraction, and (b) laser irradiation at room temperature following heating to $\sim$ 600 K. The sample temperature is indicated by the solid (red) lines.

expected to decline with time. Any benefits obtained from heating do not appear to persist in cryogenic environments, but they can be recovered if the sample is again warmed up to $\sim$ 600 K, as shown in figure 6.10(a) and (b).

Interestingly after a heating and cooling cycle, the SiO_2 sample was susceptible to a laser-induced reduction in the Ps yield at room temperature as shown in figure 6.10 (b) which strongly suggests that the laser produces paramagnetic centers that have a stability dependent on the sample temperature. Irradiation following this cycle did not reduce f_d to the minimum value observed following the irradiations before heating was done, but did reduce it towards the preheated value. This suggests that some of the improvement in f_d may have been due to desorption of material, or possibly that the stable paramagnetic centers are more difficult to populate without a heating cycle. If paramagnetic centres were present at room temperature prior to heating and their population was saturated then one would not expect any additional effect from the laser. This was observed in figure 6.7. However, these centres can be repopulated with the laser at room temperature if they have been thermally recombined prior to irradiation.

Improvements in the Ps yield due to heating is likely a combination of both the desorption of material and the thermal recombination of paramagnetic centres that are stable at room temperature, this is evidenced by the data in figures 6.9 and 6.10.

Depth profiling of irradiated samples

Measurements of f_d as a function of implantation at different sample temperatures are shown in figure 6.11. Without prior laser irradiation (figure 6.11(a)) it is expected that a decrease in f_d should be observed at higher implantation energies as the Ps must diffuse further through the sample which will reduce the Ps lifetime. However, with these samples we expect only a negligible decline for implantation energies of 3 keV, in accord with previous measurements [Crivelli *et al.*, 2010]. There is in fact a small increase in f_d as the implantation energy is raised and it is assumed that the detection efficiency of γ-rays for the detectors described in

chapter 3 is higher for slower atoms as fast Ps is able to move away from the detectors [Andersen *et al.*, 2015]. An alternative, explanation for the reduced f_d at lower beam energies could be due to the production of some paramagnetic centres induced by low energy positrons. If such paramagnetic centres were being produced the lifetime of these sites would be very short as no lasting reductions are observed following low energy positron bombardment of these samples.

The mean implantation depth is indicated on the top axis and was estimated using a Makhov type profile [Mills and Wilson, 1982],

$$z = \frac{A}{\rho} E^{\nu} \tag{6.2}$$

where E is in keV, $\nu \approx 1.7$, A 2.81 μg cm^{-2} [Algers *et al.*, 2003], and $\rho = 1.35$ g cm^{-3} is the mean density of the sample which is scaled to the sample porosity.

The target bias was varied at each of the stated temperatures in ascending order as to minimise gas adsorption effects which were expected to be minimal during the course of these measurements as one full sequence of voltages took 25 minutes to complete (see figure 6.3). Following completion of the scan at the lowest temperature, the target was irradiated as described in the previous section. This was done until the reduction in f_d reached saturation. The bias scans were repeated as the temperature was raised (6.11(b)). These measurements indicate the location of the laser induced paramagnetic centers as Ps formation occurs at a depth determined by the incident positron beam energy and implantation profile [Algers *et al.*, 2003; Mills and Wilson, 1982; Schultz and Lynn, 1988].

Below 250 K there is an energy-dependent reduction in f_d, in agreement with the model of temperature stabilised paramagnetic centers. Ps atoms diffuse further though the distribution of potential quenching sites which increases the probability of spin exchange quenching. At temperatures above 250 K no such energy dependent reductions are observed as the majority of the unpaired spins have recombined. The curves start to resemble those of 6.11(a) where there was no prior laser irradiation. At temperatures above 250 K it is assumed that the laser would

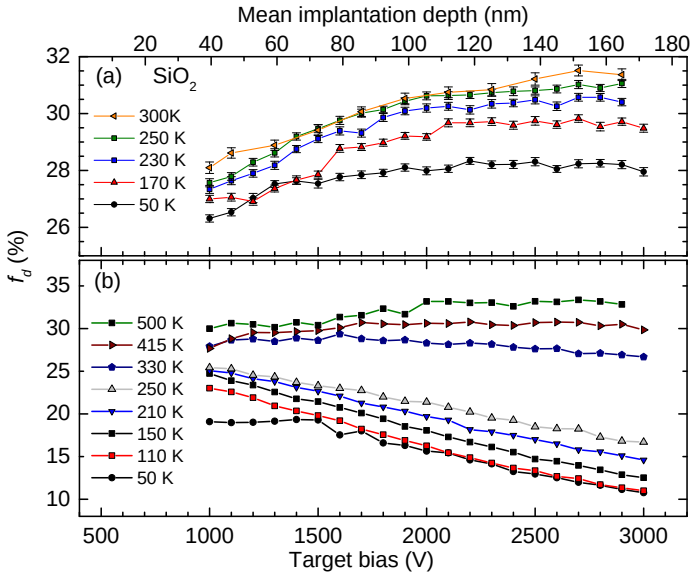

Figure 6.11: f_d versus target bias at various temperatures for a SiO_2 sample without (a) and with (b) prior UV laser irradiation. The top axis indicates the mean implantation depth of the positrons. The irradiation and heating sequence is explained in the text. Error bars are not shown in (b) but are a similar size to those in (a) [Cooper *et al.*, 2016].

not be effective in producing stable paramagnetic centers as it would seem that those produced with this form of radiation are unstable at this temperature and above. At lower temperatures, f_d is reduced by around 50 % at higher implantation energies. This suggests that either the paramagnetic centers that affect Ps atoms are created predominantly in the deeper layers of the target, or that they are primarily formed on the internal surfaces of the pores. Lifetime measurements performed on irradiated silica powders [Saito and Hyodo, 1999] suggest that the latter is correct.

The porous films are deposited on a Si substrate. Most of the incident laser irradiation is reflected by this substrate [Cassidy *et al.*, 2011a]. A measurement of the sample reflectivity was performed to verify consistency of this property of the samples used here and $> 85\%$ of the UV energy was reflected. It is therefore assumed that laser induced paramagnetic centres are distributed throughout the sample with uniformity. Those created in the bulk material are unlikely to effect the Ps as it is formed within the spur electrons [Mogensen, 1974]. The idea that Ps interacts with the paramagnetic centres that reside on the pore surfaces is reinforced by previous measurements where Ps was unable to escape the sample as a surface capping layer was used [Cassidy *et al.*, 2007]. The observed energy dependent reduction in f_d for low temperature ($T < 250$ K) irradiated samples is therefore consistent with the model of an increased diffusion length through potential quenching sites. However, explanation of the apparent linearity of this dependence with the positron implantation energy may not be so straightforward as it may be related to the way in which confined Ps atoms move between pores [Cassidy and Mills, 2011]. This observed linearity is broadly consistent with previous data where the emission times also appear to be linearly dependent on the beam energy [Deller *et al.*, 2015b]. The losses in f_d associated with Ps quenching via spin exchange with paramagentic centres can at least be partially recovered by implantation at lower energies. However, this will produce hotter Ps as shown in chapter 5.

6.1.3 Photoemission at cryogenic temperatures

The experiments outlined in previous chapters were repeated in a cryogenic environment using the Ge(100) single crystals. Preparation of Ge(100) single crystals is outlined in chapter 5. These tests were performed exclusively in the lower pressure chamber (6.2). As suggested earlier in this chapter, Ps converters that rely on a surface based mechanism for Ps production are far more susceptible to gas absorption effects at low temperatures. For Ge(100) single crystals the value of f_d plummets rapidly when exposed to background gas, much like the porous SiO_2 samples did in the higher pressure region (see figure 6.1). However, if a photoemission laser is present the absorbed material is removed from the sample much more effectively than seen in figure 6.4, and the photoemission process can be observed with high efficiency.

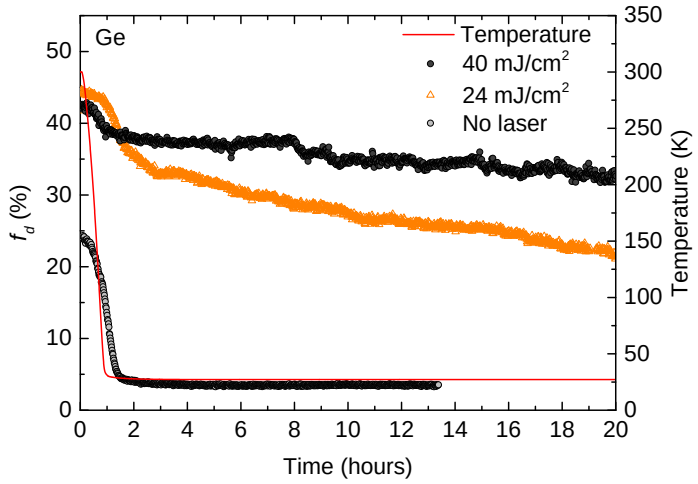

Figure 6.12: Delayed fraction (f_d) measured from a p-Ge(100) single crystal as the sample is cooled with and without 532 nm laser-induced photoemission. The laser fluence is indicated in the legend. [Cooper *et al.*, 2016]

Figure 6.12 shows the effects of f_d for a Ge(100) sample cooled to 27 K with and without the photoemission laser present. Without the laser, gas adsorption effects saturate very quickly rendering the sample unusable within two hours of turning the cold head on. Figure 6.13 shows this in terms of the SSPALS lifetime spectrum

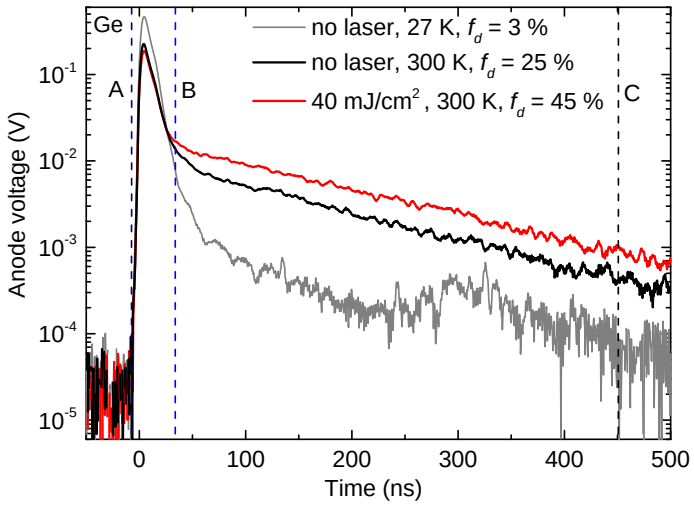

Figure 6.13: Single-shot lifetime spectra measured with a Ge target, with and without a 532 nm photoemission laser, at 300 K and 27 K. The dashed vertical lines represent the time windows *A*, *B* and *C*. Each spectrum is the average of 100 individual shots [Cooper *et al.*, 2016].

The f_d value is at background levels a matter of minutes after the target has reached its base temperature. This highlights the increased susceptibility for gas adsorption problems in semiconductors compared to the mesoporous targets which produce Ps for many days in these conditions (see figure 6.3). However, if a photoemission laser is present, the PsX yield (see chapter section 5.2), and therefore f_d is increased. The efficiency and stability of PsX photoemission is increased with higher laser fluences as shown in the figure. PsX can therefore be produced via photoemission in cryogenic environments for at least a duration shown in the figure. However, it is unclear if these samples would also require a thermal reset after some time like that of the mesoporous films, or if an equilibrium f_d is reached for a given fluence. The higher fluence test (40 mJ/cm^{-2}) show longer periods of stability suggesting that this fluence may be near the threshold value for indefinite stability. There were no visible signs of any laser induced damage to the samples following long periods of irradiation.

The cleaning effect is explored further in figure 6.14. Here the sample was

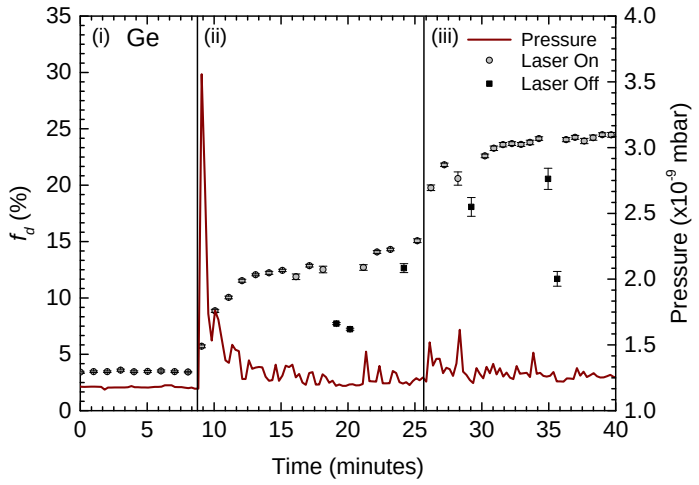

Figure 6.14: Laser irradiation of a cold and contaminated Ge sample (the sample was kept at 27 K for $\sim$ 12 hours) and its effect on (f_d). Different laser fluences were tested, as indicated by the numbered regions ((i) = laser off, (ii) = 10 mJ/cm^2, (iii) = 24 mJ/cm^2). The square points were recorded with the photoemission laser temporarily blocked [Cooper *et al.*, 2016].

left at 27 K for 12 hours which ensured complete saturation of the Ps inhibiting effects related to gas adsorption. At the start of this test essentially no emitted Ps is observed as typical background levels are $f_d \sim$ 3-4 %. When the photoemission laser is introduced f_d is recovered from $\sim$ 4 to 25%, showing that the laser is desorbing accumulated gas layers from the Ge surface. This is supported by the spike in the chamber pressure associated with the laser light. The largest spike appearing at around 9 minutes corresponding to much of the absorbed material leaving the sample. Two laser fluences were used in this test and to measure what these were, the laser had to be diverted into an energy meter. This temporary blocking of the laser resulted in the re adsorption of background gasses resulting in a decline in f_d. The points where the laser was not present or temporarily blocked in this way are indicated by solid black squares. Data obtained when the laser is present is represented by filled circles. Measuring the laser fluence only takes a couple of minutes at most. The gas adsorption effects are therefore significant on the time scale of tens of seconds. Returning the laser restores the losses.

Kinetic energy of PsX produced via photoemission

To assess whether or not thermal effects are present in the PsX emission process, Doppler spectroscopy was performed at room and cryogenic temperatures, much in the same way as explained in chapter 5. It was not expected that PsX would be emitted from the surface of Ge(100) single crystals with a reduced kinetic energy at lower temperatures as both Si and Ge did not exhibit this property in previous measurements [Cassidy *et al.*, 2011d]. In fact, this work led to the observation of the opposite and showed a slight reduction in the PsX kinetic energy at very high temperatures which was attributed to shifts of the surface energy levels.

Figure 6.15 shows data verifying that the energy of PsX emitted via photoemission from cryogenic targets does not depend strongly on the target temperature. This was achieved by measuring the Doppler-broadened $1s$-$2p$ transition line shapes. A second YAG laser was employed to photoionise PsX parallel with the target face after it has been generated via photoemission with a pulse incident at 45^o. No temperature dependent difference in the Ps energy was observed. The figure shows kinetic energies of around 170 meV in the direction of the laser, for temperatures ranging from 27-400 K.

PsX emitted from single crystal semiconductors has a broad range of energies, as evidenced by the large Doppler broadening of the $1s$-$2p$ line shapes [Cassidy *et al.*, 2011d; Cooper *et al.*, 2016]. However, the PsX kinetic energy is determined by the surface electron and positron energy levels, so the mechanism behind the broadening is not well understood. It is possible that the crystal surface could be irregular such that the electron and positron surface-state energies vary from site to site. This could contribute to variations in the emission energies. There may also be a wide range of available surface states with different energies, which would also lead to observations of a broad distribution of PsX energies. Other contributions could be from thermally or optically excited surface electrons forming Ps atoms before thermalising. This may be unlikely however given the relevant electronic relaxation rates are in general very rapid [Ichibayashi and Tanimura, 2009; Sjodin *et al.*, 1998]. Thermally generated surface interactions (e.g., phonon scattering)

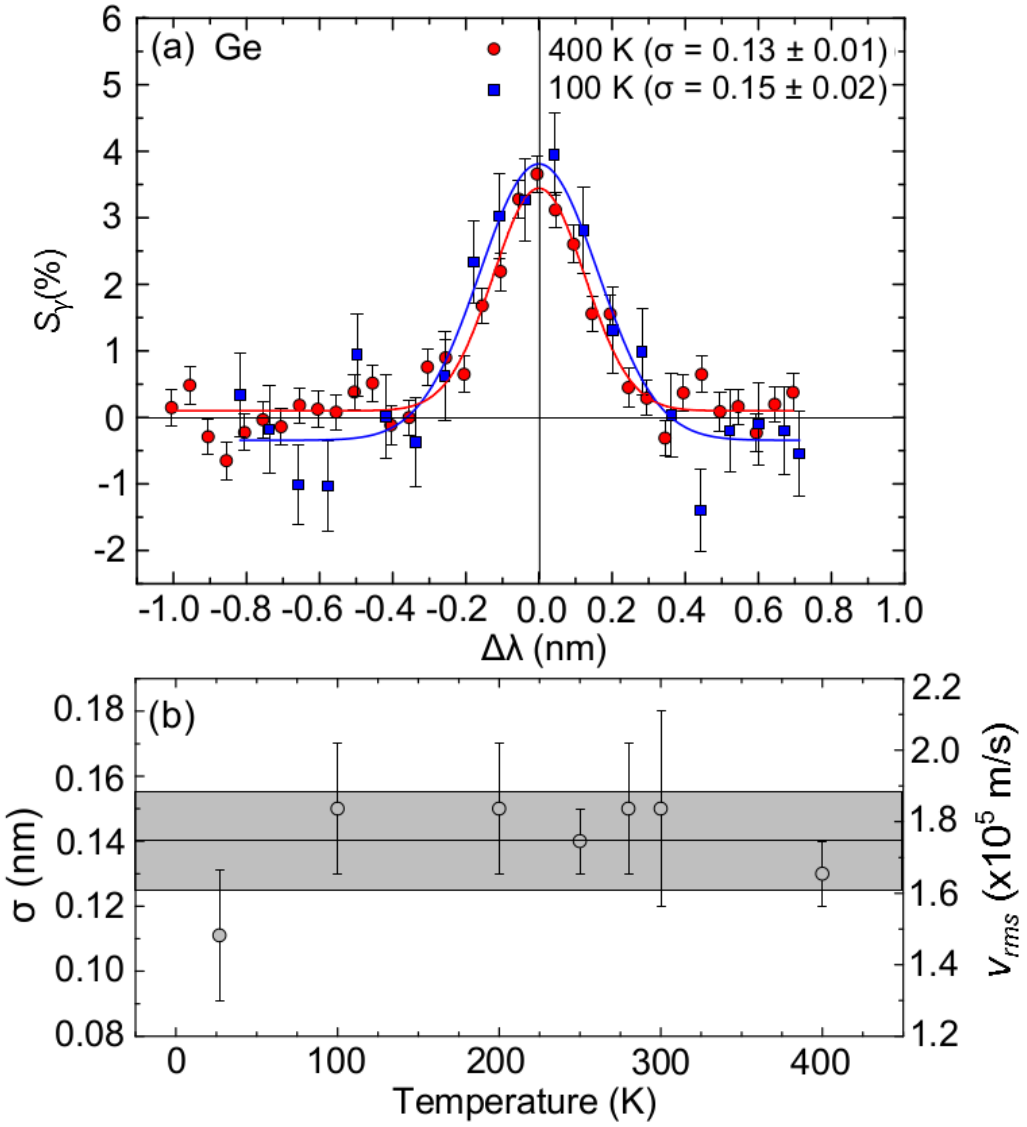

Figure 6.15: Doppler spectroscopy of Ps emitted from single crystal Ge(100). (a) Doppler broadened line-shapes measured at 400 K and 100 K. (b) Values of σ obtained from linewidth measurements conducted at different sample temperatures. The gray band indicates the mean value of $\sigma \pm 1$ standard deviation (0.140 ± 0.015 nm), and the corresponding RMS velocities. The positron beam energy was 0.65 keV for the data shown in (a) and 0.5 keV for the data in (b) [Cooper *et al.*, 2016].

could also play a part in the broadening but as figure 6.15 shows, thermally generated interactions cannot be playing a significant role as the broadening persists in cryogenic environments. Whilst these crystals are taken close to the annealing temperature during the Cl desorption routine, it may be beneficial to implement more stringent surface preparation protocols such as ion sputtering and high temperature annealing. Auger spectroscopy of these samples did show that the desorption of Cl had been successful, but it was not clear if the crystal displayed long range ordering.

It would seem that the PsX formation process via photoemission discussed here for Ge(100) may be observed in any other indirect band-gap semiconductor with dangling-bond states. Perhaps an alternative material exists that has intrinsic energy levels lower than those of Ge or Si, it may provide an efficient source of cold Ps atoms that can be used in cryogenic environments. As explained in chapter 4, overlapping a laser with Doppler broadened transitions in Ps is currently the limiting factor in the efficiency of such excitation schemes. It would therefore be extremely beneficial to find a source of cold Ps atoms for any experiments involving Ps laser excitation. It is possible to increase the laser bandwidth as discussed in chapter 4 but improving the spectral overlap of an excitation laser with a given Ps transition by reducing Doppler broadening is preferable because considerably less power is required, and more accurate state selection becomes possible [Wall *et al.*, 2015]. In addition, broadening due to shorter transit-times and 2nd order Doppler shifts are reduced if colder atoms are used.

The field of Ps physics can progress rapidly once a source of efficiently produced, low-energy Ps atom is realised. Cold Ps atoms would have many uses such as Ps Stark deceleration [Cassidy and Hogan, 2014], Ps mediated antihydrogen formation [Humberston *et al.*, 1987; Kadyrov *et al.*, 2015], Ps-atom scattering measurements [Brawley *et al.*, 2015], precision $1^3S_1 \rightarrow 2^3S_1$ optical spectroscopy [Fee *et al.*, 1993], and microwave spectroscopy of the Ps fine structure [Hagena *et al.*, 1993; Hatamian *et al.*, 1987; Mills *et al.*, 1975]. The work in this chapter has highlighted two materials that produce Ps reliably in cryogenic environments. In both cases, gas

adsorption effects can be extremely inhibiting, but these effects can be managed. In the case of mesoporous SiO_2 these effects can be mitigated with good initial vacuum conditions and regular thermal desorption of frozen gasses. Ps that is emitted from these samples can be cooled via collisions but the level of thermalisation is set by quantum confinement, not the sample temperature. These materials are highly susceptible to laser induced paramagnetic centres at low temperatures so direct contact with the laser should be avoided. In contrast, PsX emission from Ge(100) single crystals *requires* the presence of a laser for sample cleaning and population of electronic surface states which enhances the Ps yield. However, the PsX kinetic energy is much higher than desired. It is therefore concluded that the modification of existing converter materials produce cold Ps reliably at cryogenic temperatures is a promising approach to achieving these goals. Such a material will be robust enough to not be affected by laser irradiation at cryogenic temperatures. Also, it would either facilitate collisional cooling or a low energy PsX emission process with a narrow spread. Similarly, such a material may also find applications in the production of cold confined Ps, leading to studies of Ps-wall interactions [Cassidy *et al.*, 2011a], Ps laser cooling [Liang and Dermer, 1988] and the eventual formation of a Ps BEC [Platzman and Mills, 1994].

Chapter 7

Review and conclusions

The early chapters provide a detailed overview of the the experimental apparatus and its operation. Through the mastery of this system I have gained many skills such as the preparation of ultra-high-vacuum, radiation detection, and instrument control and automation. I am extremely fortunate to have been a part of this project from the beginning.

Chapter 4 described the laser system and some of the techniques and applications of Ps laser spectroscopy. These include the Doppler broadened $1s$-$2p$ transition as a tool for the determination of the Ps kinetic energy. The LEPTOF technique was also described, along with the two-step excitation scheme to Rydberg-Stark states, and the electrostatic guiding of low field seeking k-states. These techniques pave the way for the realisation of schemes in which atom optics techniques are employed to manipulate Ps atoms for advanced experiments such as a gravity measurement [Cassidy and Hogan, 2014; Mills and Leventhal, 2002].

Chapter 5 presents a survey on the Ps formation and cooling properties of a few materials. The mesoporous SiO_2 films [Fischer *et al.*, 2005; Gidley *et al.*, 1999; Liszkay *et al.*, 2008b] are extremely good materials for efficient Ps production. These materials have a high enough porosity ($\sim$ 50%) to exhibit interconnected voids which enable a route for Ps to exit the sample for experimentation in vacuum. The high porosity also increases the positron to long lived Ps (o-Ps) conversion

efficiency as Ps is more likely to diffuse into an open area following its formation in the bulk. The most efficient of these materials have mean pore diameters that are small enough ($\sim$ 5nm) such that Ps undergoes many collisions on its way to the surface where it can be emitted at reduced kinetic energies [Cassidy *et al.*, 2010a]. The kinetic energy of Ps emitted from these structures are close to, and above thermal energies which is due to the limit imposed by the confinement energy. The search for a material which produces Ps at thermal energies at high efficiency is currently underway. This could be realised using long nano-channels [Mariazzi *et al.*, 2010a,b] or one of the many materials within the class of metal-organic-frameworks [Crivelli *et al.*, 2014]. Increasing the density of Ps formed in solid insulators may lead to a Ps Bose-Einstein condensate being produced within an engineered porous structure, which could be used to stimulate annihilation radiation [Mills *et al.*, 2004; Platzman and Mills, 1994]. One can envision a porous network, or series of long nanochannels which lead to a large central void for the purpose of Ps thermalisation through wall collisions and subsequent confinement of a dense collection of Ps atoms. A Ps BEC would provide a source of coherent Ps suitable for matter-wave interferometry [Cronin *et al.*, 2009] and high resolution spectroscopy. Ps formation and long term confinement in macroporous voids was also demonstrated. By using a pulsed laser as a method of interrogation we find that the Ps lifetime is shorter than expected for the size of the cavity and this is perhaps due to chemical quenching. This raises the point that the standard practices employed by Ps porosimetry and modeling are unable to detect such processes. This work gives the first example of delayed laser excitation of Ps in a fixed location which opens up the possibilities of producing cold confined Ps, leading to studies of Ps-wall interactions [Cassidy *et al.*, 2011a], Ps laser cooling [Liang and Dermer, 1988] and perhaps the formation of a Ps BEC [Platzman and Mills, 1994].

Chapter 6 has demonstrated measurements of Ps formation from mesoporous SiO_2 films and Ge(100) single crystals at temperatures ranging from 12-700 K. The data show that Ps atoms can be created in cryogenic environments using both materials. The efficiency of production at cryogenic temperatures is comparable

to that observed at room temperature, but can be compromised by residual gas contamination. For SiO_2 films in a low pressure vacuum environment (10^{-9} mbar) the Ps formation decays on a time scale of a few days. The room temperature efficiency can be restored by heating the sample. However, these samples will decay rapidly if they are directly exposed to UV laser light via the creation of paramagnetic centers that become stable at cryogenic temperatures [Cassidy *et al.*, 2007; Saito and Hyodo, 1999]. Warming cold irradiated SiO_2 films to room temperature completely restores the Ps formation efficiency as the paramagentic centres are thermally destabilised. The effects of UV light on cold SiO_2 have implications for attempts to perform laser cooling on Ps confined in cryogenic cavities. On the contrary, PsX emission from Ge crystals is enhanced by laser irradiation, which has been previously observed in Si [Cassidy *et al.*, 2011c]. The photoemission process operates at low temperatures but low temperature Ge is highly susceptible to residual gas adsorption, and Ps emission is compromised much faster than is the case for porous SiO_2 samples. However, laser light that gives rise to photoemission will also desorb gas from a Ge surface, making it possible to produce Ps indefinitely in a cryogenic environment using laser irradiated Ge. Further studies of Ps formation from various semiconductors at low temperatures is desired as the kinetic energy of the emitted Ps may be characteristic of the material, and a low energy Ps emitter that functions in a cryogenic environment may yet to be found.

Bibliography

Al-Ramadhan, A.H. and Gidley, D.W. (1994). New precision measurement of the decay rate of singlet positronium. *Phys. Rev. Lett.*, 72:1632–1635. doi:10.1103/PhysRevLett.72.1632

Alekseev, A.I. (1958). *Soviet Phys. JETP.*, 7:826

Algers, J., Sperr, P., Egger, W., Kögel, G. and Maurer, F.H.J. (2003). Median implantation depth and implantation profile of 3-18 keV positrons in amorphous polymers. *Phys. Rev. B*, 67:125404. doi:10.1103/PhysRevB.67.125404

Alonso, A.M., Cooper, B.S., Deller, A., Hogan, S.D. and Cassidy, D.B. (2015). Controlling positronium annihilation with electric fields. *Phys. Rev. Lett.*, 115:183401. doi:10.1103/PhysRevLett.115.183401

Alonso, A.M., Cooper, B.S., Deller, A. and Cassidy, D.B. (2016). Single-shot positron annihilation lifetime spectroscopy with lyso scintillators. *Nuclear Instruments and Methods in Physics Research Section A: Accelerators, Spectrometers, Detectors and Associated Equipment*, 828(Supplement C):163 – 169. ISSN 0168-9002. doi:https://doi.org/10.1016/j.nima.2016.05.049

Alonso, A.M., Cooper, B.S., Deller, A., Gurung, L., Hogan, S.D. and Cassidy, D.B. (2017). Velocity selection of Rydberg positronium using a curved electrostatic guide. *Phys. Rev. A*, 95:053409. doi:10.1103/PhysRevA.95.053409

Andersen, S.L., Cassidy, D.B., Chevallier, J., Cooper, B.S., Deller, A., Wall, T.E. and Uggerhoj, U.I. (2015). Positronium emission and cooling in reflection and transmission from thin meso-structured silica films. *Journal of Physics B: Atomic, Molecular and Optical Physics*, 48(20):204003

Anderson, C.D. (1933). The positive electron. *Phys. Rev.*, 43:491–494. doi:10.1103/PhysRev.43.491

Andresen, G.B., Ashkezari, M.D., Baquero-Ruiz, M., Bertsche, W., Bowe, P.D., Butler, E., Cesar, C.L., Chapman, S., Charlton, M., Deller, A., Eriksson, S., Fajans, J., Friesen, T., Fujiwara, M.C., Gill, D.R., Gutierrez, A., Hangst, J.S., Hardy, W.N., Hayden, M.E., Humphries, A.J., Hydomako, R., Jenkins, M.J., Jonsell, S., Jørgensen, L.V., Kurchaninov, L., Madsen, N., Menary, S., Nolan, P., Olchanski, K., Olin, A., Povilus, A., Pusa, P., Robicheaux, F., Sarid, E., Seif el Nasr, S., Silveira, D.M., So, C., Storey, J.W., Thompson, R.I., van der Werf, D.P., Wurtele, J.S. and Yamazaki, Y. (2010). Trapped antihydrogen. *Nature*, 468(7324):673–676. doi:10.1038/nature09610

Antognini, A., Nez, F., Schuhmann, K., Amaro, F.D., Biraben, F., Cardoso, J.M.R., Covita, D.S., Dax, A., Dhawan, S., Diepold, M., Fernandes, L.M.P., Giesen, A., Gouvea, A.L., Graf, T., Hänsch, T.W., Indelicato, P., Julien, L., Kao, C.Y., Knowles, P., Kottmann, F., Le Bigot, E.O., Liu, Y.W., Lopes, J.A.M., Ludhova, L., Monteiro, C.M.B., Mulhauser, F., Nebel, T., Rabinowitz, P., dos Santos, J.M.F., Schaller, L.A., Schwob, C., Taqqu, D., Veloso, J.F.C.A., Vogelsang, J. and Pohl, R. (2013). Proton structure from the measurement of 2s-2p transition frequencies of muonic hydrogen. *Science*, 339(6118):417–420. ISSN 0036-8075. doi:10.1126/science.1230016

Avetissian, H.K., Avetissian, A.K. and Mkrtchian, G.F. (2014). Self-amplified gamma-ray laser on positronium atoms from a Bose-Einstein condensate. *Phys. Rev. Lett.*, 113:023904. doi:10.1103/PhysRevLett.113.023904

Berko, S., and Pendleton, H.N. (1980). Positronium. *Annual Review of Nuclear and Particle Science*, 30(1):543–581. doi:10.1146/annurev.ns.30.120180.002551

Bertolotti, M. and Sibilia, C. (1979). Coherent γ-emission by stimulated annihilation of electron-positron pairs. *Appl. Phys*, 19(1):127–130. ISSN 0340-3793. doi:10.1007/BF00900548

Blackett, P.M.S. and Occhialini, G.P.S. (1933). Some photographs of the tracks of penetrating radiation. *Proceedings of the Royal Society of London A: Mathematical, Physical and Engineering Sciences*, 139(839):699–726. ISSN 0950-1207. doi:10.1098/rspa.1933.0048

Brandt, W. and Paulin, R. (1968). Positronium diffusion in solids. *Phys. Rev. Lett.*, 21:193–195. doi:10.1103/PhysRevLett.21.193

Brandt, W., Dupasquier, A. and italiana di fisica, S. (1983). *Positron solid-state physics: Varenna on Lake Como, Villa Monastero, 14-24 July 1981*. Number v. 1981 in Enrico Fermi International School of Physics Series. North-Holland

Brawley, S.J., Fayer, S.E., Shipman, M. and Laricchia, G. (2015). Positronium production and scattering below its breakup threshold. *Phys. Rev. Lett.*, 115:223201. doi:10.1103/PhysRevLett.115.223201

Brinker, C.J., Lu, Y., Sellinger, A. and Fan, H. (1999). Evaporation-induced self-assembly: Nanostructures made easy. *Advanced Materials*, 11(7):579–585. ISSN 1521-4095. doi:10.1002/(SICI)1521-4095(199905)11:7<579::AID-ADMA579>3.0.CO;2-R

Brown, R., Prigent, Q., Swann, A.R. and Gribakin, G.F. (2017). Effective radius of ground- and excited-state positronium in collisions with hard walls. *Phys. Rev. A*, 95:032705. doi:10.1103/PhysRevA.95.032705

Callaway, J. (1959). Formation of positronium in an electron gas. *Phys. Rev.*, 116:1140–1140. doi:10.1103/PhysRev.116.1140

Canter, K.F., Mills, A.P. and Berko, S. (1974). Efficient positronium formation by slow positrons incident on solid targets. *Phys. Rev. Lett.*, 33:7–10. doi:10.1103/PhysRevLett.33.7

Cassidy, D. and Mills, A.P. (2007a). A fast detector for single-shot positron annihilation lifetime spectroscopy. *Nuclear Instruments and Methods in Physics Research Section A: Accelerators, Spectrometers, Detectors and Associated Equipment*, 580(3):1338 – 1343. ISSN 0168-9002. doi:http://dx.doi.org/10.1016/j.nima.2007.06.078

Cassidy, D.B., Deng, S.H.M., Greaves, R.G. and Mills, A.P. (2006a). Accumulator for the production of intense positron pulses. *Review of Scientific Instruments*, 77(7):073106. doi:http://dx.doi.org/10.1063/1.2221509

Cassidy, D.B., Deng, S.H.M., Tanaka, H.K.M. and Mills, A.P. (2006b). Single shot positron annihilation lifetime spectroscopy. *Applied Physics Letters*, 88(19):194105. doi:http://dx.doi.org/10.1063/1.2203336

Cassidy, D.B. and Mills, A.P. (2007b). Physics with dense positronium. *physica status solidi (c)*, 4(10):3419–3428. ISSN 1610-1642. doi:10.1002/pssc.200675760

Cassidy, D.B., Yokoyama, K.T., Deng, S.H.M., Griscom, D.L., Miyadera, H., Tom, H.W.K., Varma, C.M. and Mills, A.P. (2007). Positronium as a probe of transient paramagnetic centers in a-SiO_2. *Phys. Rev. B*, 75:085415. doi:10.1103/PhysRevB.75.085415

Cassidy, D.B. and Mills, A.P. (2007c). The production of molecular positronium. *Nature*, 449(7159):195–197

Cassidy, D.B. and Mills, A.P. (2007d). Radiation damage in a-SiO_2 exposed to intense positron pulses. *Nuclear Instruments and Methods in Physics Research Section B: Beam Interactions with Materials and Atoms*, 262(1):59 – 64

Cassidy, D.B. and Mills, A.P. (2008). Interactions between positronium atoms in porous silica. *Phys. Rev. Lett.*, 100:013401. doi:10.1103/PhysRevLett.100.013401

Cassidy, D.B., Crivelli, P., Hisakado, T.H., Liszkay, L., Meligne, V.E., Perez, P., Tom, H.W.K. and Mills, A.P. (2010a). Positronium cooling in porous silica measured via Doppler spectroscopy. *Phys. Rev. A*, 81:012715. doi:10.1103/PhysRevA.81.012715

Cassidy, D.B., Meligne, V.E. and Mills, A.P. (2010b). Production of a fully spin-polarized ensemble of positronium atoms. *Phys. Rev. Lett.*, 104:173401. doi:10.1103/PhysRevLett.104.173401

Cassidy, D.B., Bromley, M.W.J., Cota, L.C., Hisakado, T.H., Tom, H.W.K. and Mills, A.P. (2011a). Cavity induced shift and narrowing of the positronium Lyman- α transition. *Phys. Rev. Lett.*, 106:023401. doi:10.1103/PhysRevLett.106.023401

Cassidy, D.B. and Mills, A.P. (2011). Enhanced Ps-Ps interactions due to quantum confinement. *Phys. Rev. Lett.*, 107:213401. doi:10.1103/PhysRevLett.107.213401

Cassidy, D.B., Hisakado, T.H., Tom, H.W.K. and Mills, A.P. (2011b). New mechanism for positronium formation on a silicon surface. *Phys. Rev. Lett.*, 106:133401. doi:10.1103/PhysRevLett.106.133401

Cassidy, D.B., Hisakado, T.H., Tom, H.W.K. and Mills, A.P. (2011c). Photoemission of positronium from Si. *Phys. Rev. Lett.*, 107:033401. doi:10.1103/PhysRevLett.107.033401

Cassidy, D.B., Hisakado, T., Tom, H. and Mills, A.P. (2011d). Positronium formation via excitonlike states on Si and Ge surfaces. *Phys. Rev. B*, 84:195312. doi:10.1103/PhysRevB.84.195312

Cassidy, D.B., Hisakado, T.H., Tom, H.W.K. and Mills, A.P. (2012a). Optical spectroscopy of molecular positronium. *Phys. Rev. Lett.*, 108:133402. doi:10.1103/PhysRevLett.108.133402

Cassidy, D.B., Hisakado, T.H., Tom, H.W.K. and Mills, A.P. (2012b). Positronium hyperfine interval measured via saturated absorption spectroscopy. *Phys. Rev. Lett.*, 109:073401. doi:10.1103/PhysRevLett.109.073401

Cassidy, D.B. and Hogan, S.D. (2014). Atom control and gravity measurements using Rydberg positronium. *International Journal of Modern Physics: Conference Series*, 30:1460259. doi:10.1142/S2010194514602592

Charlton, M. (1990). Antihydrogen production in collisions of antiprotons with excited states of positronium. *Physics Letters A*, 143(3):143 – 146. ISSN 0375-9601. doi:https://doi.org/10.1016/0375-9601(90)90665-B

Chu, S., Mills, A.P. and Murray, C.A. (1981). Thermodynamics of positronium thermal desorption from surfaces. *Phys. Rev. B*, 23:2060–2064. doi:10.1103/PhysRevB.23.2060

Chu, S., Mills, A.P. and Hall, J.L. (1984). Measurement of the positronium 1^3s_1-2^3s_1 interval by doppler-free two-photon spectroscopy. *Phys. Rev. Lett.*, 52:1689–1692. doi:10.1103/PhysRevLett.52.1689

Clarke, J., van der Werf, D.P., Griffiths, B., Beddows, D.C.S., Charlton, M., Telle, H.H. and Watkeys, P.R. (2006). Design and operation of a two-stage positron accumulator. *Review of Scientific Instruments*, 77(6):063302. doi:http://dx.doi.org/10.1063/1.2206561

Cooke, D.W., McClellan, K.J., Bennett, B.L., Roper, J.M., Whittaker, M.T., Muenchausen, R.E. and Sze, R.C. (2000). Crystal growth and optical characterization of cerium-doped lu1.8y0.2sio5. *Journal of Applied Physics*, 88(12):7360–7362. doi:10.1063/1.1328775

Cooper, B.S., Alonso, A.M., Deller, A., Wall, T.E. and Cassidy, D.B. (2015). A trap-based pulsed positron beam optimised for positronium laser spectroscopy. *Rev. Sci. Instrum*, 86(10):103101. doi:http://dx.doi.org/10.1063/1.4931690

Cooper, B.S., Alonso, A.M., Deller, A., Liszkay, L. and Cassidy, D.B. (2016). Positronium production in cryogenic environments. *Phys. Rev. B*, 93:125305. doi:10.1103/PhysRevB.93.125305

Cotterill, R.M.J., Petersen, K., Trumpy, G. and Traff, J. (1972). Positron lifetimes and trapping probabilities observed separately for vacancies and dislocations in aluminium. *Journal of Physics F: Metal Physics*, 2(3):459

Cowan, T., Beck, B., Hartley, J., Howell, R., Rohatgi, R., Fajans, J. and Gopalan, R. (1993). Development of a pure cryogenic positron plasma using a linac positron source. *Hyperfine Interactions*, 76(1):135–142. ISSN 0304-3843. doi:10.1007/BF02316712

Crivelli, P., Gendotti, U., Rubbia, A., Liszkay, L., Perez, P. and Corbel, C. (2010). Measurement of the orthopositronium confinement energy in mesoporous thin films. *Phys. Rev. A*, 81:052703. doi:10.1103/PhysRevA.81.052703

Crivelli, P., Cooke, D., Barbiellini, B., Brown, B.L., Feldblyum, J.I., Guo, P., Gidley, D.W., Gerchow, L. and Matzger, A.J. (2014). Positronium emission spectra from self-assembled metal-organic frameworks. *Phys. Rev. B*, 89:241103. doi:10.1103/PhysRevB.89.241103

Cronin, A.D., Schmiedmayer, J. and Pritchard, D.E. (2009). Optics and interferometry with atoms and molecules. *Rev. Mod. Phys.*, 81:1051–1129. doi:10.1103/RevModPhys.81.1051

Curry, S. and Schawlow, A. (1971). Measurements of the kinetic energy of free positronium formed in mgo. *Physics Letters A*, 37(1):5 – 6. ISSN 0375-9601. doi:https://doi.org/10.1016/0375-9601(71)90304-5

Curry, S.M. (1973). Combined zeeman and motional stark effects in the first excited state of positronium. *Phys. Rev. A*, 7:447–450. doi:10.1103/PhysRevA.7.447

D. Kleppner, M.G.L. and Zimmerman, M.L. (1983). *Rydberg States of Atoms and Molecules*. Cambridge University Press

Damburg, R.J. and Kolosov, V.V. (1979). A hydrogen atom in a uniform electric field. iii. *Journal of Physics B: Atomic and Molecular Physics*, 12(16):2637

Danielson, J.R. and Surko, C.M. (2005). Torque-balanced high-density steady states of single-component plasmas. *Phys. Rev. Lett.*, 94:035001. doi:10.1103/PhysRevLett.94.035001

Danielson, J.R., , D.H.E., Greaves, R.G. and Surko, C.M. (2015). Plasma and trap-based techniques for science with positrons. *Rev. Mod. Phys.*, 87:247–306. doi:10.1103/RevModPhys.87.247

Darewych, J.W. (1987). Formation of antihydrogen in excited states in antiproton-positronium collisions. *Journal of Physics B: Atomic and Molecular Physics*, 20(21):5917

Dauwe, C. and Mbungu-Tsumbu (1992). Orthopositronium study of positron-irradiation-induced surface defects in alumina powder. *Phys. Rev. B*, 45:9–19. doi:10.1103/PhysRevB.45.9

Dauwe, C., Van Waeyenberge, B., Segers, D., Van Hoecke, T. and Kuriplach, J. (1996). Some aspects of the interactions of orthopositronium with perfect and defect surfaces of insulating materials. *Journal of Radioanalytical and Nuclear Chemistry*, 210(2):293–308. ISSN 0236-5731. doi:10.1007/BF02056374

Deller, A., Mortensen, T., Isaac, C.A., van der Werf, D.P. and Charlton, M. (2014). Radially selective inward transport of positrons in a penning–malmberg trap. *New Journal of Physics*, 16(7):073028

Deller, A., Edwards, D., Mortensen, T., Isaac, C.A., van der Werf, D.P., Telle, H.H. and Charlton, M. (2015a). Exciting positronium with a solid-state UV laser: the Doppler-broadened Lyman-α transition. *J. Phys. B*, 48(17):175001

Deller, A., Cooper, B.S., Wall, T.E. and Cassidy, D.B. (2015b). Positronium emission from mesoporous silica studied by laser-enhanced time-of-flight spectroscopy. *New J. Phys*, 17(4):043059

Deller, A., Alonso, A.M., Cooper, B.S., Hogan, S.D. and Cassidy, D.B. (2016a). Electrostatically guided Rydberg positronium. *Phys. Rev. Lett.*, 117:073202. doi:10.1103/PhysRevLett.117.073202

Deller, A., Alonso, A.M., Cooper, B.S., Hogan, S.D. and Cassidy, D.B. (2016b). Measurement of Rydberg positronium fluorescence lifetimes. *Phys. Rev. A*, 93:062513. doi:10.1103/PhysRevA.93.062513

Demtröder, W. (2003). *Laser Spectroscopy*. Springer, New York, third edition. ISBN 3-540-65225-6

Deutch, B.I., Jacobsen, F.M., Andersen, L.H., Hvelplund, P., Knudsen, H., Holzscheiter, M.H., Charlton, M. and Laricchia, G. (1988). Antihydrogen production by positronium-antiproton collisions in an ion trap. *Physica Scripta*, 1988(T22):248

Deutch, B.I., Charlton, M., Holzscheiter, M.H., Hvelplund, P., Jørgensen, L.V., Knudsen, H., Laricchia, G., Merrison, J.P. and Poulsen, M.R. (1993). Antihydrogen synthesis by the reaction of antiprotons with excited state positronium atoms. *Hyperfine Interactions*, 76(1):151–161. ISSN 1572-9540. doi:10.1007/BF02316714

Deutsch, M. (1951). Evidence for the formation of positronium in gases. *Phys. Rev.*, 82:455–456. doi:10.1103/PhysRev.82.455

Deutsch, M. and Brown, S. (1952). Zeeman effect and hyperfine splitting of positronium. *Phys. Rev*, 84:1047–1048

Dicke, R.H. (1953). The effect of collisions upon the Doppler width of spectral lines. *Phys. Rev.*, 89:472–473. doi:10.1103/PhysRev.89.472

Dirac, P.A.M. (1928a). The quantum theory of the electron. *Proceedings of the Royal Society of London A: Mathematical, Physical and Engineering Sciences*, 117(778):610–624. ISSN 0950-1207. doi:10.1098/rspa.1928.0023

Dirac, P.A.M. (1928b). The quantum theory of the electron. Part II. *Proceedings of the Royal Society London A*, 118:351–361. doi:10.1098/rspa.1928.0056

Dirac, P.A.M. (1930). A theory of electrons and protons. *Proceedings of the Royal Society London A*, 126(801):360–365. doi:10.1098/rspa.1930.0013

Dirac, P.A.M. (1931). Quantised singularities in the electromagnetic field. *Proceedings of the Royal Society London A*, 133(821):60–72. doi:10.1098/rspa.1931.0130

Djourelov, N., Suzuki, T., Shantarovich, V. and Kondo, K. (2005). Positronium formation in sol-gel-prepared silica-based glasses: temperature and positron-irradiation effect. *Radiation Physics and Chemistry*, 72(6):723 – 729. ISSN 0969-806X. doi:http://dx.doi.org/10.1016/j.radphyschem.2004.04.030

Doser, M. and the Aegis collaboration (2010). Aegis: An experiment to measure the gravitational interaction between matter and antimatter. *Journal of Physics: Conference Series*, 199(1):012009

Einstein, A. (1905). Ist die trägheit eines körpers von seinem energieinhalt abhängig? *Annalen der Physik*, 323(13):639–641. ISSN 1521-3889. doi:10.1002/andp.19053231314

Einstein, A. (1907). Über die vom relativitätsprinzip geforderte trägheit der energie. *Annalen der Physik*, 328(7):371–384. ISSN 1521-3889. doi:10.1002/andp.19073280713

Eldrup, M., Lightbody, D. and Sherwood, J. (1981). The temperature dependence of positron lifetimes in solid pivalic acid. *Chemical Physics*, 63(1):51 – 58. ISSN 0301-0104. doi:https://doi.org/10.1016/0301-0104(81)80307-2

Ermolaev, A., Bransden, B. and Mandal, C. (1987). Theoretical cross sections for formation of antihydrogen in p+ps collisions in the antiproton energy range 2–100 kev lab. *Physics Letters A*, 125(1):44 – 46. ISSN 0375-9601. doi:https://doi.org/10.1016/0375-9601(87)90516-0

Fee, M.S., Mills, A.P., Chu, S., Shaw, E.D., Danzmann, K., Chichester, R.J. and Zuckerman, D.M. (1993). Measurement of the positronium 1^3S_1-2^3S_1 interval by continuous-wave two-photon excitation. *Phys. Rev. Lett.*, 70:1397–1400. doi:10.1103/PhysRevLett.70.1397

Ferrell, R.A. (1951). The positronium fine structure. *Phys. Rev.*, 84:858–859. doi:10.1103/PhysRev.84.858

Ferrell, R.A. (1958). Ortho-parapositronium quenching by paramagnetic molecules and ions. *Phys. Rev.*, 110:1355–1357. doi:10.1103/PhysRev.110.1355

Feynman, R.P. (1949a). Space-time approach to quantum electrodynamics. *Phys. Rev.*, 76:769–789. doi:10.1103/PhysRev.76.769

Feynman, R.P. (1949b). The theory of positrons. *Phys. Rev.*, 76:749–759. doi:10.1103/PhysRev.76.749

Fischer, B.M., Mortensen, J. and Højgaard, L. (2001). Positron emission tomography in the diagnosis and staging of lung cancer: a systematic, quantitative review. *The Lancet Oncology*, 2(11):659 – 666. ISSN 1470-2045. doi:https://doi.org/10.1016/S1470-2045(01)00555-1

Fischer, C.G., Weber, M.H., Wang, C.L., McNeil, S.P. and Lynn, K.G. (2005). Positronium in low temperature mesoporous films. *Phys. Rev. B*, 71:180102. doi:10.1103/PhysRevB.71.180102

Ford, G.W., Sander, L.M. and Witten, T.A. (1976). Lifetime effects of positronium in powders. *Phys. Rev. Lett.*, 36:1269–1272. doi:10.1103/PhysRevLett.36.1269

Gabrielse, G., Bowden, N.S., Oxley, P., Speck, A., Storry, C.H., Tan, J.N., Wessels, M., Grzonka, D., Oelert, W., Schepers, G., Sefzick, T., Walz, J., Pittner, H., Hänsch, T.W. and Hessels, E.A. (2002). Background-free observation of cold antihydrogen with field-ionization analysis of its states. *Phys. Rev. Lett.*, 89:213401. doi:10.1103/PhysRevLett.89.213401

Gallagher, T.F. (1994). *Rydberg Atoms*. Cambridge University Press

Gidley, D.W., Frieze, W.E., Dull, T.L., Yee, A.F., Ryan, E.T. and Ho, H.M. (1999). Positronium annihilation in mesoporous thin films. *Phys. Rev. B*, 60:R5157–R5160. doi:10.1103/PhysRevB.60.R5157

Gidley, D.W., Peng, H.G. and Vallery, R.S. (2006). Positron annihilation as a method to characterize porous materials. *Annu. Rev. Mater. Res.*, 36:49–79. doi:10.1146/annurev.matsci.36.111904.135144

Greaves, R.G. and Surko, C.M. (2000). Inward transport and compression of a positron plasma by a rotating electric field. *Phys. Rev. Lett.*, 85:1883–1886. doi:10.1103/PhysRevLett.85.1883

Greaves, R.G. and Moxom, J. (2003). Design and performance of a trap based positron beam source. *AIP Conference Proceedings*, 692(1):140–148. doi:http://dx.doi.org/10.1063/1.1635169

Greaves, R.G. and Moxom, J.M. (2008). Compression of trapped positrons in a single particle regime by a rotating electric field. *Physics of Plasmas (1994-present)*, 15(7):072304. doi:http://dx.doi.org/10.1063/1.2956335

Grosso, D., Cagnol, F., Soler-Illia, G.J.d.A.A., Crepaldi, E.L., Amenitsch, H., Brunet-Bruneau, A., Bourgeois, A. and Sanchez, C. (2004). Fundamentals of mesostructuring through evaporation-induced self-assembly. *Advanced Functional Materials*, 14(4):309–322. ISSN 1616-3028. doi:10.1002/adfm.200305036

Hagena, D., Ley, R., Weil, D., Werth, G., Arnold, W. and Schneider, H. (1993). Precise measurement of $n = 2$ positronium fine-structure intervals. *Phys. Rev. Lett.*, 71:2887–2890. doi:10.1103/PhysRevLett.71.2887

Hatamian, S., Conti, R.S. and Rich, A. (1987). Measurements of the 2^3S_1-2^3P_j ($j = 0, 1, 2$) fine-structure splittings in positronium. *Phys. Rev. Lett.*, 58:1833–1836. doi:10.1103/PhysRevLett.58.1833

He, C., Ohdaira, T., Oshima, N., Muramatsu, M., Kinomura, A., Suzuki, R., Oka, T. and Kobayashi, Y. (2007). Evidence for pore surface dependent positronium thermalization in mesoporous silica/hybrid silica films. *Phys. Rev. B*, 75:195404. doi:10.1103/PhysRevB.75.195404

He, C., Wang, S., Kobayashi, Y., Ohdaira, T. and Suzuki, R. (2012). Role of pore morphology in positronium diffusion in mesoporous silica thin films and in positronium emission from the surfaces. *Phys. Rev. B*, 86:075415. doi:10.1103/PhysRevB.86.075415

Hench, L.L. and West, J.K. (1990). The sol-gel process. *Chemical Reviews*, 90(1):33–72. doi:10.1021/cr00099a003

Hessels, E.A., Homan, D.M. and Cavagnero, M.J. (1998). Two-stage Rydberg charge exchange: An efficient method for production of antihydrogen. *Phys. Rev. A*, 57:1668–1671. doi:10.1103/PhysRevA.57.1668

Hogan, S.D., Allmendinger, P., Saßmannshausen, H., Schmutz, H. and Merkt, F. (2012). Surface-electrode Rydberg-Stark decelerator. *Phys. Rev. Lett.*, 108:063008. doi:10.1103/PhysRevLett.108.063008

Hogan, S.D. (2013). Calculated photoexcitation spectra of positronium Rydberg states. *Phys. Rev. A*, 87:063423. doi:10.1103/PhysRevA.87.063423

Hotop, H. and Niehaus, A. (1968). Reactions of excited atoms and molecules with atoms and molecules. *Zeitschrift für Physik*, 215(4):395–407. ISSN 0044-3328. doi:10.1007/BF01380020

Howell, R., Fluss, M., Rosenberg, I. and Meyer, P. (1985). Low-energy, high-intensity positron beam experiments with a linac. *Nuclear Instruments and Methods in Physics Research Section B: Beam Interactions with Materials and Atoms*, 10(Part 1):373 – 377. ISSN 0168-583X. doi:https://doi.org/10.1016/0168-583X(85)90272-1

Huang, X.P., Anderegg, F., Hollmann, E.M., Driscoll, C.F. and O'Neil, T.M. (1997). Steady-state confinement of non-neutral plasmas by rotating electric fields. *Phys. Rev. Lett.*, 78:875–878. doi:10.1103/PhysRevLett.78.875

Humberston, J.W., Charlton, M., Jacobson, F.M. and Deutch, B.I. (1987). On antihydrogen formation in collisions of antiprotons with positronium. *J. Phys. B*, 20(1):L25

Ichibayashi, T. and Tanimura, K. (2009). Ultrafast carrier relaxation in Si studied by time-resolved two-photon photoemission spectroscopy: Intravalley scattering and energy relaxation of hot electrons. *Phys. Rev. Lett.*, 102:087403. doi:10.1103/PhysRevLett.102.087403

Ido, T. and Katori, H. (2003). Recoil-free spectroscopy of neutral sr atoms in the lamb-dicke regime. *Phys. Rev. Lett.*, 91:053001. doi:10.1103/PhysRevLett.91.053001

Imperor-Clerc, M., Davidson, P. and Davidson, A. (2000). Existence of a microporous corona around the mesopores of silica-based SBA-15 materials templated by triblock copolymers. *Journal of the American Chemical Society*, 122(48):11925–11933. doi:10.1021/ja002245h

Jentschura, U.D. (2013). Gravitationally coupled dirac equation for antimatter. *Phys. Rev. A*, 87:032101. doi:10.1103/PhysRevA.87.032101

Jones, A.C.L., Hisakado, T.H., Goldman, H.J., Tom, H.W.K., Mills, A.P. and Cassidy, D.B. (2014). Doppler-corrected Balmer spectroscopy of Rydberg positronium. *Phys. Rev. A*, 90:012503. doi:10.1103/PhysRevA.90.012503

Jones, A.C.L., Goldman, H.J., Zhai, Q., Feng, P., Tom, H.W.K. and Mills, A.P. (2015). Monoenergetic positronium emission from metal-organic framework crystals. *Phys. Rev. Lett.*, 114:153201. doi:10.1103/PhysRevLett.114.153201

Kadyrov, A.S., Rawlins, C.M., Stelbovics, A.T., Bray, I. and Charlton, M. (2015). Antihydrogen formation via antiproton scattering with excited positronium. *Phys. Rev. Lett.*, 114:183201. doi:10.1103/PhysRevLett.114.183201

Karshenboim, S.G. (2004). Precision study of positronium: Testing bound state qed theory. *International Journal of Modern Physics A*, 19(23):3879–3896. doi:10.1142/S0217751X04020142

Kasevich, M. and Chu, S. (1992). Measurement of the gravitational acceleration of an atom with a light-pulse atom interferometer. *Applied Physics B*, 54(5):321–332. ISSN 1432-0649. doi:10.1007/BF00325375

Krasnický, D., Caravita, R., Canali, C. and Testera, G. (2016). Cross section for Rydberg antihydrogen production via charge exchange between Rydberg positroniums and antiprotons in a magnetic field. *Phys. Rev. A*, 94:022714. doi:10.1103/PhysRevA.94.022714

Lazzarini, A.F. and Lazzarini, E. (2001). Metal electron delocalization in 3d complexes estimated by positronium spin-exchange reactions. *Coordination Chemistry Reviews*, 213(1):159 – 180. ISSN 0010-8545

Ley, R. (2002). Atomic physics of positronium with intense slow positron beams. *Applied Surface Science*, 194(1–4):301 – 306. 9th International Workshop on Slow Positron Beam Techniques for Solids and Surfaces

Liang, E.P. and Dermer, C.D. (1988). Laser cooling of positronium. *Optics Communications*, 65(6):419 – 424. ISSN 0030-4018. doi:http://dx.doi.org/10.1016/0030-4018(88)90116-2

Liouville, J. (1838). *Journal. de Math*, 3

Liszkay, L., Barthe, M.F., Corbel, C., Crivelli, P., Desgardin, P., Etienne, M., Ohdaira, T., Perez, P., Suzuki, R., Valtchev, V. and Walcarius, A. (2008a). Orthopositronium annihilation and emission in mesostructured thin silica and silicalite-1 films. *Appl. Surf. Sci.*, 255(1):187–190. ISSN 0169-4332. doi:10.1016/j.apsusc.2008.05.210

Liszkay, L., Corbel, C., Perez, P., Desgardin, P., Barthe, M.F., Ohdaira, T., Suzuki, R., Crivelli, P., Gendotti, U., Rubbia, A., Etienne, M. and Walcarius, A. (2008b). Positronium reemission yield from mesostructured silica films. *Appl. Phys. Lett.*, 92(6):063114. doi:10.1063/1.2844888

Liszkay, L., Guillemot, F., Corbel, C., Boilot, J.P., Gacoin, T., Barthel, E., Pérez, P., Barthe, M.F., Desgardin, P., Crivelli, P., Gendotti, U. and Rubbia, A. (2012). Positron annihilation in latex-templated macroporous silica films: pore size and ortho-positronium escape. *New. J. Phys*, 14(6):065009

Madsen, N., Robicheaux, F. and Jonsell, S. (2014). Antihydrogen trapping assisted by sympathetically cooled positrons. *New Journal of Physics*, 16(6):063046

Malmberg, J.H. and deGrassie, J.S. (1975). Properties of nonneutral plasma. *Phys. Rev. Lett.*, 35:577–580. doi:10.1103/PhysRevLett.35.577

Malmberg, J.H. and Driscoll, C.F. (1980). Long-time containment of a pure electron plasma. *Phys. Rev. Lett.*, 44:654–657. doi:10.1103/PhysRevLett.44.654

Mariazzi, S., Toniutti, L., Patel, N. and Brusa, R. (2008). Formation and escaping of positronium in porous SiO_2 films at low temperature. *Appl. Surf. Sci.*, 255(1):191 – 193. ISSN 0169-4332. doi:http://dx.doi.org/10.1016/j.apsusc.2008.05.207. Proceedings of the Eleventh International Workshop on Slow Positron Beam Techniques for Solids and Surfaces

Mariazzi, S., Bettotti, P., Larcheri, S., Toniutti, L. and Brusa, R.S. (2010a). High positronium yield and emission into the vacuum from oxidized tunable nanochannels in silicon. *Phys. Rev. B*, 81:235418. doi:10.1103/PhysRevB.81.235418

Mariazzi, S., Bettotti, P. and Brusa, R.S. (2010b). Positronium cooling and emission in vacuum from nanochannels at cryogenic temperature. *Phys. Rev. Lett.*, 104:243401. doi:10.1103/PhysRevLett.104.243401

Marler, J.P. and Surko, C.M. (2005a). Positron-impact ionization, positronium formation, and electronic excitation cross sections for diatomic molecules. *Phys. Rev. A*, 72:062713. doi:10.1103/PhysRevA.72.062713

Marler, J.P. and Surko, C.M. (2005b). Positron-impact ionization, positronium formation, and electronic excitation cross sections for diatomic molecules. *Phys. Rev. A*, 72:062713. doi:10.1103/PhysRevA.72.062713

McMahon, H.O. and Gifford, W.E. (1960). *A New Low-Temperature Gas Expansion Cycle*, pp. 354–367. Springer US, Boston, MA. ISBN 978-1-4757-0537-9. doi:10.1007/978-1-4757-0537-9_43

Merhra, J. and Rechenberg, H. (2000). *The Historical Development of Quantum Theory, Volume 6: The Completion of Quantum Mechanics*. Springer. ISBN 978-0-387-95175-1

Merrison, J.P., Bluhme, H., Chevallier, J., Deutch, B.I., Hvelplund, P., Jørgensen, L.V., Knudsen, H., Poulsen, M.R. and Charlton, M. (1997). Hydrogen formation by proton impact on positronium. *Phys. Rev. Lett.*, 78:2728–2731. doi:10.1103/PhysRevLett.78.2728

Michishio, K., Tachibana, T., Terabe, H., Igarashi, A., Wada, K., Kuga, T., Yagishita, A., Hyodo, T. and Nagashima, Y. (2011). Photodetachment of positronium negative ions. *Phys. Rev. Lett.*, 106:153401. doi:10.1103/PhysRevLett.106.153401

Mills, A.P., Berko, S. and Canter, K.F. (1975). Fine-structure measurement in the first excited state of positronium. *Phys. Rev. Lett.*, 34:1541–1544. doi:10.1103/PhysRevLett.34.1541

Mills, A.P. (1978). Positronium formation at surfaces. *Phys. Rev. Lett*, 41(26):1828–1831

Mills, A.P. and Pfeiffer, L. (1979). Desorption of surface positrons: A source of free positronium at thermal velocities. *Phys. Rev. Lett.*, 43:1961–1964. doi:10.1103/PhysRevLett.43.1961

Mills, A.P. (1979). Thermal activation measurement of positron binding energies at surfaces. *Solid State Communications*, 31(9):623 – 626. ISSN 0038-1098. doi:http://dx.doi.org/10.1016/0038-1098(79)90310-7

Mills, A.P. (1980). Time bunching of slow positrons for annihilation lifetime and pulsed laser photon absorption experiments. *Appl. Phys.*, 22(3):273–276. ISSN 0340-3793. doi:10.1007/BF00899876

Mills, A.P. and Wilson, R.J. (1982). Transmission of 1 - 6 keV positrons through thin metal films. *Phys. Rev. A*, 26:490–500. doi:10.1103/PhysRevA.26.490

Mills, A.P. and Gullikson, E.M. (1986). Solid neon moderator for producing slow positrons. *Applied Physics Letters*, 49(1121)

Mills, A.P. (1989). Positron moderation and remoderation techniques for producing cold positron and positronium sources. *Hyperfine Interactions*, 44(1-4):105–123. ISSN 0304-3843. doi:10.1007/BF02398662

Mills, A.P., Shaw, E.D., Chichester, R.J. and Zuckerman, D.M. (1989). Production of slow positron bunches using a microtron accelerator. *Rev. Sci. Instrum*, 60(5):825–830. doi:http://dx.doi.org/10.1063/1.1141030

Mills, A.P., Shaw, E.D., Leventhal, M., Chichester, R.J. and Zuckerman, D.M. (1991). Thermal desorption of cold positronium from oxygen-treated Al(111) surfaces. *Phys. Rev. B*, 44:5791–5799. doi:10.1103/PhysRevB.44.5791

Mills, A.P. and Leventhal, M. (2002). Can we measure the gravitational free fall of cold Rydberg state positronium? *Nuclear Instruments and Methods in Physics Research B*, 192

Mills, A.P., Cassidy, D.B. and Greaves, R.G. (2004). Prospects for making a bose-einstein-condensed positronium annihilation gamma ray laser. *Materials Science Forum*, 445-446:424–429

Mills, A.P. (2010). Physics with many positrons. In A.D. R. S. Brusa and A.P. Mills, editors, *Course CLXXIV "Physics with Many Positrons"*, pp. 77– 187. Proceedings of the International School of Physics 'Enrico Fermi', IOS Press, Amserdam

Mills, A.P. (2014). Possibilities with pulsed polarized high density slow positrons. *J. Phys: Conference Series*, 505(1):012039

Mogensen, O.E. (1974). Spur reaction model of positronium formation. *The Journal of Chemical Physics*, 60(3):998–1004. doi:http://dx.doi.org/10.1063/1.1681180

Moia, F., Ferragut, R., Dupasquier, A., Giammarchi, M. and Ding, G. (2012). Thermal production of positronium in porous alumina. *The European Physical Journal D*, 66(5):124. ISSN 1434-6060

Morandi, O., Hervieux, P.A. and Manfredi, G. (2014). Bose-Einstein condensation of positronium in silica pores. *Phys. Rev. A*, 89:033609. doi:10.1103/PhysRevA.89.033609

Nagashima, Y., Kakimoto, M., Hyodo, T., Fujiwara, K., Ichimura, A., Chang, T., Deng, J., Akahane, T., Chiba, T., Suzuki, K., McKee, B.T.A. and Stewart, A.T. (1995). Thermalization of free positronium atoms by collisions with silica-powder grains, aerogel grains, and gas molecules. *Phys. Rev. A*, 52:258–265. doi:10.1103/PhysRevA.52.258

Nagashima, Y., Morinaka, Y., Kurihara, T., Nagai, Y., Hyodo, T., Shidara, T. and Nakahara, K. (1998). Origins of positronium emitted from SiO_2. *Phys. Rev. B*, 58:12676–12679. doi:10.1103/PhysRevB.58.12676

Nagashima, Y. (2014). Experiments on positronium negative ions. *Physics Reports*, 545(3):95 – 123. ISSN 0370-1573. doi:http://dx.doi.org/10.1016/j.physrep.2014.07.004. Experiments on positronium negative ions

Natisin, M.R., Danielson, J.R. and Surko, C.M. (2014). Positron cooling by vibrational and rotational excitation of molecular gases. *Journal of Physics B: Atomic, Molecular and Optical Physics*, 47(22):225209

Oppenheimer, J.R. (1930). On the theory of electrons and protons. *Phys. Rev.*, 35:562–563. doi:10.1103/PhysRev.35.562

Ore, A. and Powell, J.L. (1949). Three-photon annihilation of an electron-positron pair. *Phys. Rev.*, 75:1696–1699. doi:10.1103/PhysRev.75.1696

Paulin, R. and Ambrosino, G. (1968). Annihilation libre de l'ortho-positonium forme dans certaines poudres de grande surface specifique. *J. Phys. France*, 29(4):263–270. doi:10.1051/jphys:01968002904026300

Platzman, P.M. and Mills, A.P. (1994). Possibilities for Bose condensation of positronium. *Phys. Rev. B*, 49:454–458. doi:10.1103/PhysRevB.49.454

Poulsen, M.R., Charlton, M., Chevallier, J., Deutch, B.I., Jorgensen, L.V. and Laricchia, G. (1991). Thermal activation of positronium from thin ag(100) films in backscattering and transmission geometries. *Journal of Physics: Condensed Matter*, 3(17):2849

R. Khatri, M., Charlton, M., Sferiazzo, P., Lynn, K.G., Mills, A.P. and Roellig, L.O. (1990). Improvement of rare-gas solid moderators by using conical geometry. *Applied Physics Letters*, 57(2374)

Ramaty, R. and Jones, F.C. and McKinley, J.M., Journal = apj, Y...M..m.P...V... (????). On the theory of gamma-ray amplification through stimulated annihilation radiation

Rao, K. and Sunandana, C. (2008). Structure and microstructure of combustion synthesized mgo nanoparticles and nanocrystalline mgo thin films synthesized by solution growth route. 43:146–154

Rich, A. (1981). Recent experimental advances in positronium research. *Rev. Mod. Phys.*, 53(1):127. doi:10.1103/RevModPhys.53.127

Robbie, K., Friedrich, L.J., Dew, S.K., Smy, T. and Brett, M.J. (1995). Fabrication of thin films with highly porous microstructures. *Journal of Vacuum Science & Technology A: Vacuum, Surfaces, and Films*, 13(3):1032–1035. doi:10.1116/1.579579

Saito, H., Nagashima, Y., Hyodo, T. and Chang, T. (1995). Detection of paramagnetic centers on amorphous-SiO_2 grain surfaces using positronium. *Phys. Rev. B*, 52:R689–R692. doi:10.1103/PhysRevB.52.R689

Saito, H. and Hyodo, T. (1999). Quenching of positronium by surface paramagnetic centers in ultraviolet- and positron-irradiated fine oxide grains. *Phys. Rev. B*, 60:11070–11077. doi:10.1103/PhysRevB.60.11070

Salpeter, E.E. and Bethe, H.A. (1951). A relativistic equation for bound-state problems. *Phys. Rev.*, 84:1232–1242. doi:10.1103/PhysRev.84.1232

Schultz, P.J. and Lynn, K.G. (1988). Interaction of positron beams with surfaces, thin films, and interfaces. *Rev. Mod. Phys.*, 60:701–779. doi:10.1103/RevModPhys.60.701

Sferlazzo, P., Berko, S. and Canter, K.F. (1987). Time-of-flight spectroscopy of positronium emission from quartz and magnesium oxide. *Phys. Rev. B*, 35:5315–5318. doi:10.1103/PhysRevB.35.5315

Sferlazzo, P., Berko, S., Lynn, K.G., Mills, A.P., Roellig, L.O., Viescas, A.J. and West, R.N. (1988). Evidence for phonon-assisted positronium emission from graphite. *Phys. Rev. Lett.*, 60:538–541. doi:10.1103/PhysRevLett.60.538

Sjodin, T., Petek, H. and Dai, H. (1998). Ultrafast carrier dynamics in silicon: A two-color transient reflection grating study on a (111) surface. *Phys. Rev. Lett.*, 81:5664–5667. doi:10.1103/PhysRevLett.81.5664

Sommerfeld, A. and Welker, H. (1938). Künstliche grenzbedingungen beim keplerproblem. *Annalen der Physik*, 424(1-2):56–65. ISSN 1521-3889. doi:10.1002/andp.19384240109

Storry, C.H., Speck, A., Sage, D.L., Guise, N., Gabrielse, G., Grzonka, D., Oelert, W., Schepers, G., Sefzick, T., Pittner, H., Herrmann, M., Walz, J., Hänsch, T.W., Comeau, D. and Hessels, E.A. (2004). First laser-controlled antihydrogen production. *Phys. Rev. Lett.*, 93:263401. doi:10.1103/PhysRevLett.93.263401

Sullivan, J.P., Roberts, J., Weed, R.W., Went, M.R., Newman, D.S. and Buckman, S.J. (2010). A trap-based positron beamline for the study of materials. *Measurement Science and Technology*, 21(8):085702

Surko, C. (2010). Accumulation, storage and manipulation of large numbers of positrons in traps i. the basics. In A.D. R. S. Brusa and A.P. Mills, editors, *Course CLXXIV "Physics with Many Positrons"*, pp. 511– 543. Proceedings of the International School of Physics 'Enrico Fermi', IOS Press, Amserdam

Surko, C.M., Leventhal, M. and Passner, A. (1989). Positron plasma in the laboratory. *Phys. Rev. Lett.*, 62:901–904. doi:10.1103/PhysRevLett.62.901

Tao, S. (1974). Positronium in molecular substances. *Applied physics*, 3(1):1–7. ISSN 0340-3793. doi:10.1007/BF00892327

Tao, S.J. (1972). Positronium annihilation in molecular substances. *The Journal of Chemical Physics*, 56(11):5499–5510. doi:10.1063/1.1677067

Tianbao, C., Min, X. and Xiangtao, Z. (1987). Effect of the energy loss process on the annihilation of orthopositronium in silica aerogel. *Phys. Lett. A*, 126(3):189 – 194. ISSN 0375-9601. doi:http://dx.doi.org/10.1016/0375-9601(87)90458-0

Tomonaga, S.I. and Oppenheimer, J.R. (1948). On infinite field reactions in quantum field theory. *Phys. Rev.*, 74:224–225. doi:10.1103/PhysRev.74.224

Vallery, R.S., Zitzewitz, P.W. and Gidley, D.W. (2003). Resolution of the orthopositronium-lifetime puzzle. *Phys. Rev. Lett.*, 90:203402. doi:10.1103/PhysRevLett.90.203402

Vliegen, E., Limacher, P.A. and Merkt, F. (2006). Measurement of the three-dimensional velocity distribution of Stark-decelerated Rydberg atoms. *The European Physical Journal D - Atomic, Molecular, Optical and Plasma Physics*, 40(1):73–80. ISSN 1434-6079. doi:10.1140/epjd/e2006-00095-1

Vliegen, E. and Merkt, F. (2006). Normal-incidence electrostatic Rydberg atom mirror. *Phys. Rev. Lett.*, 97:033002. doi:10.1103/PhysRevLett.97.033002

Wada, K. and Hyodo, T. (2013). A simple shape-free model for pore-size estimation with positron annihilation lifetime spectroscopy. *Journal of Physics: Conference Series*, 443(1):012003

Wall, T.E., Alonso, A.M., Cooper, B.S., Deller, A., Hogan, S.D. and Cassidy, D.B. (2015). Selective production of Rydberg-Stark states of positronium. *Phys. Rev. Lett.*, 114(173001)

Wang, Y., Anderson, B.M. and Clark, C.W. (2014). Spinor Bose-Einstein condensates of positronium. *Phys. Rev. A*, 89:043624. doi:10.1103/PhysRevA.89.043624

Ward, S.J., Humberston, J.W. and McDowell, M.R.C. (1987). Elastic scattering of electrons (or positrons) from positronium and the photodetachment of the positronium negative ion. *Journal of Physics B: Atomic and Molecular Physics*, 20(1):127

Weinelt, M., Kutschera, M., Fauster, T. and Rohlfing, M. (2004). Dynamics of exciton formation at the Si(100) c(4 $\times$ 2) surface. *Phys. Rev. Lett.*, 92:126801. doi:10.1103/PhysRevLett.92.126801

Wieman, C.E., Pritchard, D.E. and Wineland, D.J. (1999). Atom cooling, trapping, and quantum manipulation. *Rev. Mod. Phys.*, 71:S253–S262. doi:10.1103/RevModPhys.71.S253

Willitsch, S., Bell, M.T., Gingell, A.D., Procter, S.R. and Softley, T.P. (2008). Cold reactive collisions between laser-cooled ions and velocity-selected neutral molecules. *Phys. Rev. Lett.*, 100:043203. doi:10.1103/PhysRevLett.100.043203

Wiza, J.L. (1979). Microchannel plate detectors. *Nuclear Instruments and Methods*, 162(1–3):587 – 601. ISSN 0029-554X. doi:10.1016/0029-554X(79)90734-1

Wolfenstein, L. and Ravenhall, D.G. (1952). Some consequences of invariance under charge conjugation. *Phys. Rev.*, 88:279–282. doi:10.1103/PhysRev.88.279

Yang, C.N. (1950). Selection rules for the dematerialization of a particle into two photons. *Phys. Rev.*, 77:242–245. doi:10.1103/PhysRev.77.242

Zhang, H.J., Chen, Z.Q., Wang, S.J., Kawasuso, A. and Morishita, N. (2010). Spin conversion of positronium in NiO/Al_2O_3 catalysts observed by coincidence Doppler broadening technique. *Phys. Rev. B*, 82:035439. doi:10.1103/PhysRevB.82.035439

Ziock, K.P., Howell, R.H., Magnotta, F., Failor, R.A. and Jones, K.M. (1990a). First observation of resonant excitation of high-n states in positronium. *Phys. Rev. Lett.*, 64:2366–2369. doi:10.1103/PhysRevLett.64.2366

Ziock, K.P., Dermer, C.D., Howell, R.H., Magnotta, F. and Jones, K.M. (1990b). Optical saturation of the 1^3S-2^3P transition in positronium. *J. Phys. B*, 23(2):329. doi:10.1088/0953-4075/23/2/015